مجلة الخوارزمي الهندسية

تعليمات النشر

تصدر مجلة الخوارزمي الهندسية أربعة اعداد سنويا وتعنى بنشر البحوث العلمية الاصيلة والمراجعات العلمية والمقالات المختصرة غير المنشورة سابقاً في مجال اختصاصات هندسة الطب الحياتي وهندسة المعلومات وهندسة الميكاترونيكس وهندسة عمليات التصنيع والهندسة الكيميائية الاحيائية والتخصصات الهندسية الاخرى .

- تقدم البحوث بـثلاث نسـخ مرفقـة بالمخططــات والرسـوم والصـور الاصلية.
- تقدم البحوث بلغة انكليزيـة سـليمة ومطبوعة على ورق A4 بعمـودين مع ترقيم الصفحات وحسب الفورمات المقدمة.
- تتضمن صفحة الغلاف عنوان البحث، اسم المؤلــف (او المـؤلفين) واسـم المؤسسة (المؤسسات) التي ينتمـون اليها وعنوانهـا البريـدي ويؤشـر المؤلف الذي توجه اليه المراسـلات. بعد ذلك عنـوان البحـث واسمـاء المؤلفين باللغة العربية.
- تتضمن الصـفحة التاليـة: عنـوان البحث، خلاصة من ٨٠-٢٠٠ كلمة ثم خلاصة باللغة العربية مـن ٥٠-١٥٠ كلمة.
- تثبت الجداول والرسـوم والصـور خارج المتن على ان يؤشر موقعهـا التقديري ضمن المتن.

- يستخدم نظام الوحدات العـالمي SI units
- توضع المصادر في نهايـة البحـث وبترتيب حسب ورودها في البحث.
- يرفق القرص المرن ٣٫٥ " او قرص مدمج الذي يحوي مسـودة النهائيـة المقبولة للنشر اضافة الى المخططات والرسوم ضمن نظام windows.
- تمتلك هيئة التحرير الحريـة الكاملـة لاجــراء التعــديلات فـي اللغـة والاسلوب.
- تقدم البحوث مع رسالة الـى رئـيس هيئة تحرير المجلة تتضـمن طلـب النشر مع تعهد بـأن البحث المقدم لـم يسبق نشره في اية جهة اخرى.
- ترسل البحوث وكافـة المراسـلات الخاصة بالمجلة الى :
  رئيس هيئة تحرير مجلة الخوارزمي الهندسية
  ص.ب: ٤٧٠٠٨ جادرية - بغداد- العراق
  البريد الالكتروني:
  journal@kecbu.uobaghdad.edu.iq

مجلة الخوارزمي الهندسية

مجلة علمية هندسية محكمة تصدرعن كلية هندسة الخوارزمي

AL-KHWARIZMI ENGINEERING JOURNAL

AIMS AND SCOPE

Al-Khwarizmi Engineering Journal is issued four times a year by AL-Khwarizmi college of Engineering – University of Baghdad. It is concerned with the publication of the original manuscripts: research papers, scientific notes and articles in related engineering fields of specialization such as: Bio-Medical, Information, Mechatronics, Manufacturing Operations and Bio-Chemical Engineering.

INSTRUCTIONS FOR AUTHORS

- Three copies of the original manuscript should be submitted together with the original diagrams, photographs and tables.
- The manuscript should be written in formal English and typed on A4 paper type and formatted in tow Columns.
- The cover page should include: Research title, authors names, name of organization, mail address, and an indication to whom correspondence should be addressed. It should also include authors name in Arabic language.
- The second page should include: the research title and an abstract within 80-200 words written in English language. An Arabic abstract should also be included within 50-150 words.
- Tables, figures, graphs and photographs should be included outside the main body of the manuscript and referred to else where.
- The use of System International (SI) units as primary units of measure is mandatory.
- Reference should be placed at the end of the manuscript.
- A floppy or compact disk (CD) containing the electronic copy of the submitted work should be attached to the final submitted manuscript.
- The magazine has the right to impose changes in terms of grammar and style if necessary.
- The manuscript is presented accompanied by a cover letter to the president of the editorial board. The letter should include a confirmation that the material is not readily available else where; i.e., it has not been published previously.
- Address all correspondence and inquiries to the following

AL-KHWARIZMI ENGINEERING JOURNAL

AL-KHWARIZMI ENGINEERING JOURNAL

A Referred Scientific
Journal Issued by Al-Khwarizmi College of Engineering
University of Baghdad.

An Experimental Study on the Effect of Shape and Location of Vortex Generators Ahead of a Heat Exchanger

Wisam Abed Kattea

Department of Machines and Equipment Engineering /University of Technology
Email: wisam_bd@yahoo.com

Abstract

An experimental study is carried out on the effect of vortex generators (Circular and square) on the flow and heat transfer at variable locations at (X = 0.5, 1.5, 2.5 cm) ahead of a heat exchanger with Reynolds number ranging from $62000 < Re < 125000$ and heat flux from $3000 \leq q \leq 8000 \ W/m^2$.

In the experimental investigation, an apparatus is set up to measure the velocity and temperatures around the heat exchanger.

The results show that there is an effect for using vortex generators on heat transfer. Also, heat transfer depends on the shape and location. The circular is found to be the best shape for enhancing heat transfer at location [X_m=0.5 cm] distance before heat exchanger is the best location for enhancing heat transfer. The square is the best shape for enhancing heat transfer at location [X_m=2.5 cm] distance before heat exchanger is the best location for enhancing heat transfer.

The results of flow over heat exchanger with vortex generators are compared with the flow over heat exchanger without vortex generators. Heat transfer around heat exchanger is enhanced (56%, 50%, 36%) at location (X=0.5, 1.5, 2.5cm) respectively by using circular vortex generators without turbulator and heat transfer around heat exchanger is enhanced (39%, 42%, 51%) at location (X=0.5, 1.5, 2.5cm) respectively by using square shape vortex generators without turbulator.

Keywords: Vortex generator: VGs, NUX: Local nusselt number heat exchanger, vortex flow, heat transfer.

1. Introduction

Convectional types of heat exchanger are externally plain tube in cross flow. They are widely used in chemical, petrochemical, automotive industry, cooling towers, heated pipes refrigerators of power plants as well as in applications for heating, refrigeration and air conditioning. In finned tube heat exchanger liquid or steam flows through the tube and gas through fin ducts, [1], [2]. Heat transfer is closely related to fluid dynamics. That is why heat transfer is considered simultaneously with fluid dynamics [3].

Heat transfer and fluid dynamic around curvilinear body as cylinder is complex process and need a big efforts to find out temperatures, pressure and velocity distribution. Therefore one

must know what happens when the fluid flows over bluff bodies as sphere, wire and tube.

The ability to manipulate a flow field to improve efficiency or performance is of immense technological importance. Flow control is one of the leading areas of research of many scientists and engineers in fluid mechanics. The potential benefits of flow control include performance and maneuverability, affordability, increased range and payload, and environmental compliance. The intent of flow control may be to delay/advance transition, to suppress / enhance turbulence, or to prevent/promote separation. The resulting benefits include drag reduction, lift enhancement, mixing augmentation, heat transfer enhancement, and flow–induced noise suppression. The objectives of

flow control may be interrelated, leading to potential conflicts as the achievement of one particular goal may adversely affect another goal. For example, consider an aircraft wing for which the performance is measured by the improvement in lift-to-drag ratio. Promoting transition will lead to a turbulent boundary layer that is more resistant to separation and increased lift can be obtained at higher angle of incidence. The viscous or skin – friction drag for a laminar boundary layer can be an order of magnitude smaller than that for a turbulent boundary layer. However, a laminar boundary layer is more prone to separation resulting in a loss in lift and an increase in form drag.

The performance of liquid-to-air and two-phase-to-air heat exchangers is important in many applications, including thermal management and processing systems found in the air conditioning, automotive, refrigeration, chemical, and petroleum industries. Improving the performance of these heat exchangers can lead to a smaller surface-area requirement, reduced material cost, and a lower heat exchanger mass. Furthermore, improving heat exchanger performance can have a significant impact on the environment through improvements in energy efficiency. The total thermal resistance in these heat exchangers can be considered as the sum of three contributions: the liquid or two-phase convective resistance, the wall conductive resistance, and the air-side convective resistance. The air-side convective resistance is typically the dominant resistance to heat transfer,[4], and efforts to improve these heat exchangers should focus on the air - side heat-transfer behavior. The type of turbulator using heat exchanger is shown in Figure (1). [5]
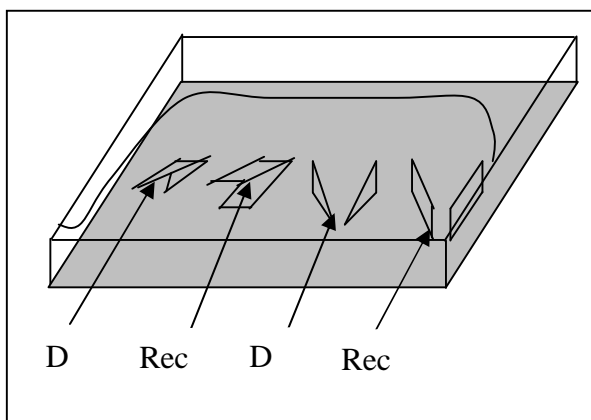

Fig. 1.Type of Vortex Generator.

1.1. Vortex Generation

At the front of region of tube there is high heat transfer due to small boundary layer (B.L) thickness but there is a small heat transfer at the rear region especially at separation point. This region is therefore prime focus area for transport enhancement, [4]. The strategy proposed here involves placing the vortex generators (V.Gs) in front of or behind the tube to prevent growth of boundary layer (B.L) and to transfer the separation point to the rear region of tube in order to reject the minimum heat transfer region to the rear. The (V.Gs) are small plates placed in the stream flow of mixed flow, disturbing flow and controlling the growth of boundary layer, [6], has any shape; the common shapes of (V.Gs) (winglets) are circular and square. The (V.Gs) winglets affect both tube and fin, all previous studies were studied the effect of wing and winglet on heat transfer from the fin by generating a vortex due to pressure difference between front surface and back surface, this vortex will mix the hot fluid near the surfaces with cold main flow, this process enhances heat transition from the surfaces, [7]. The effect of winglet on tube guides the flow at high momentum in to low heat transfer region, [6].The size, shape and angle of attack of winglet determine the specific characteristics of the vortices generated in the flow, [8].

1. 2. Application of VGs

The advantages of these vortex generators or tabulators (turbulence promoters) are to:

1. Improve heat exchange in compact heat exchangers and electronic equipment packages or microelectronic devices in industrial application ,[9] like the wide use of plate-fin and fin-tube heat exchangers, for example, in dry cooling towers, in chemical industry and in automotive applications ,[10].
2. Enhance heat transfer in channels. e.g, parallel plate channel, rectangular, triangular, square ducts, U-Bend of strong curvature applications, and grooved channel, [11].
3. Increase heat transfer rate inside or out side tubes, for example, gas flow out side the tube and liquid flow inside the tube and the finned tubes situated in vertical channel.
4. Enhance the cooling capability of gas-cooled nuclear rector, for example, finned nuclear fuel.

5. Increase internal cooling in the passages of modern gas turbine blades and vanes that must be protected from hot gas streams.
6. Improve the aerodynamic performance by using various types of vortex generators, for example, to improve the performance of conical diffusers, or by using thin slender wings to make modern combat airplanes fly at high angles of attack.
7. Decrease vortex losses in channels, for example, in channels of power plants, ventilation systems, and in various pipes, owing to the influence of the positive pressure gradient associated with variation in cross section or bending of the channel intense formation of vortices which takes place as a rule due to flow separation. These formations of vortices cause an increase in hydraulic losses and in degree of no uniformity. A new method of decreasing losses is based on division of vortices by transverse baffles or fins positioned on one side [12].
8. In aerodynamics, in spite of longitudinal (stream wise) vortices, which lead to an improvement of 80%, also a reduction of 5% behind the investigated grids depends on the wavelength and the intensity of the disturbance [13].

1.3. Applications of Heat Exchangers

Flow of this nature can be found in engineering systems of significant technological interest such as heat exchangers, nuclear reactor cores, air-cooled solar collectors, some microelectronic circuit boards, waste water aeration tanks as well as chemical mixers and other chemical engineering applications [14].

1.4. Objective of Present Work Problem

The experimental goals of this study are to: -
1-Investigate the flow and heat transfer phenomena of multi-types vortex generators located in rectangular ducts and to enhance heat transfer in turbulent flows.
2-Set up an experiment model for a duct rig especially designed and manufactured for this study to cover wide range of applications with more accurate tools of measurements for flow pattern and temperature isothermal contours in air and solid domains.
3-Investigate the effect of changing Reynolds number, velocity, temperature, and thermal

performance, and average Nusselt number on ducts and VGs surfaces.

2. Literature Survey

2.1. The Effect of Vortex on Heat Exchanger

Chien-Nan Lin and Jiin-Yuh Jang [15] studied the use of fins with embedded wave-type vortex generators to enhance heat transfer in fin-tube heat exchangers .An infrared thermo vision is used to visualize the temperature distribution on the surface of a scaled-up plain fin and upon fins with embedded vortex generators. Numerical methods are used to investigate the conjugate heat transfer and to perform a 3-D turbulence.
Analysis of the heat transfer and fluid flow associated with wave type vortex generators embedded fins. The current results indicate that heat transfer and friction losses are strongly dependent on the geometric parameters of the vortex generators. This study identifies maximum improvement of (120) % in the local heat transfer coefficient and an improvement of (18.5) % in the average heat transfer coefficient. Furthermore; it is found that a reduction in fin area of approximately (18–20) % may be obtained if vortex generators embedded fins are used in place of plain fins. Finally, it is noted that the magnitude of the attainable fin area reduction increases for higher Reynolds numbers.
Pesteei, et al [16] measured Local heat transfer coefficients on fin-tube heat exchanger with winglets using a single heater of 2 inch diameter and five different positions of winglet type vortex generators. The measurements were made at Reynolds number about 2250. Flow losses were determined by measuring the static pressure drop in the system. Results showed a substantial increase in the heat transfer with winglet type vortex generators. It was observed that average Nusselt number increased by about (46) % while the local heat transfer coefficient was improved by several times as compared to plain fin-tube heat exchanger. The maximum improvement is observed in the re-circulation zone. The best location of the winglets was with DX = 0.5D and DY = 0.5D. The increase in pressure drop for the existing situation was of the order of (18) %.
Torii, et al [17], in their paper propose that can augment heat transfer but nevertheless can reduce pressure-loss in a fin-tube heat exchanger with

circular tubes in a relatively low Reynolds number flow, by deploying delta winglet-type vortex generators. The winglets are placed with a heretofore-unused orientation for the purpose of augmentation of heat transfer. This orientation is called ''common flow up'' configuration. The proposed configuration causes significant separation delay, reduces form drag, and removes the zone of poor heat transfer from the near-wake of the tubes. This enhancement strategy has been successfully verified by experiments in the proposed configuration. In case of staggered tube banks, the heat transfer was augmented by (30) % to (10) %, and yet the pressure loss was reduced by (55) % to (34) % for the Reynolds number (based on two times channel height) ranging from 350 to 2100, when the present winglets were added. In case of in-line tube banks, these were found to be (20%) to (10%) augmentation, and (15%) to (8%) reduction, respectively.

In a Joardar and Jacobi [18] the effectiveness of delta-wing type vortex generators was experimentally evaluated by full-scale wind-tunnel testing of a compact heat exchanger typical to those used in automotive systems. The mechanisms important to vortex enhancement methods are discussed, and a basis for selecting a delta-wing design as a vortex generator is established. The heat transfer and pressure drop performance are assessed at full scale under both dry- and wet-surface conditions for a louvered- fin baseline and for a vortex-enhanced louvered-fin heat exchanger. An average heat transfer increase over the baseline case of (21) % for dry conditions and (23.4) % for wet conditions was achieved with a pressure drop penalty smaller than (7) %. Vortex generation is proven to provide an improved thermal-hydraulic performance in compact heat exchangers for automotive systems.

2.2. Wing and Winglet–Type Vortex Generators

Heat transfer and fluid mechanics data were obtained by Pauley and Eaton [19], for a turbulent boundary layer with arrays of embedded stream wise vortices containing both counter-rotating and co-rotating vortex pairs. The data show that these arrays can cause both large local variations in the heat transfer rate and significant net heat transfer augmentation over large areas. Close proximity of other vortices strongly affects the development of the vortex arrays by modifying the trajectory that they follow. The vortices in turn produce strong distortion of the normal two-dimensional

boundary layer structure, which is due to their secondary flow. When one vortex convects another toward the wall, a strong boundary layer distortion occurs. The heat transfer is elevated where the secondary flow is directed toward the wall and reduced where the secondary flow is directed away from the wall. When adjacent vortices lift their neighbor away from the wall, minimal modification of the heat transfer results . The primary influence of grouping multiple vortex pairs into arrays is the development of stable patterns of vortices. These stable vortex patterns produce vortices that interact with the boundary layer and strongly modify the heat transfer far downstream, even where the vortices have decayed in strength.

Vortex generators are small plats placed in the flow path (Sohal et al)[7] **,** using to generate a secondary flow or vortices by swirl and disability the flow, along the side edges of vortex generator the flow was separated and it generated a longitudinal vortices due to pressure difference between the forward and back side of vortex generators.

Vortex generators such as pins, ribs, wings, winglets have been successfully used as a powerful way for enhanced heat transfer in the development of modern heat exchangers. Vortex generators can be generating a transfer longitudinal vortex with strongly disturbed the flow structure. Longitudinal vortex generated by using wing and winglet and spiral the flow around there axis. Many researchers have studied the effect of vortex generator on heat transfer and pressure drop from the duct wall numerically and experimentally with common type of vortex generated (rectangular and triangular (delta) shapes).

The analogy between heat and mass transfer has been used by Wang et al, [20], to obtain local and average heat transfer characteristics over a complete flat tube-fin element with four VGs per tube. Several types of surfaces involved in heat transfer process such as fin surface mounted with VGs, its back surface (mounted without VGs) and flat tube surface are considered. The mass transfer experiments are performed using naphthalene sublimation method. The effects of the fin spacing and VGs parameters such as height and attack angle on heat transfer and pressure drop are investigated. The comparisons of heat transfer enhancement with flat tube-fin element without VGs enhancement under three constraints are carried out. The local Nusselt number distribution reveals that VGs can efficiently enhance the heat transfer in the region near flat tube on fin surface

mounted with VGs. On its back surface the enhancement is almost the same as on the fin surface mounted with VGs but enhanced region is away from flat tube wall with some distance. Average results reveal that increasing of VGs height and attack angle increases the enhancement of heat transfer and pressure drop, whereas small fin spacing causes greater increase in pressure drop. The heat transfer performance, correlations of Nusselt number and friction factor are also given.

Tiggelbeck et al, [21], Investigated the effect of four types of vortex generators (delta wing, delta winglet rectangular wing and rectangular winglet) as shown in Figure (2) on local heat transfer and drag of plat fins and compared the results between these types of vortex generators and in the Reynolds number range (2000-9000) with angle of attack range of (30°-90°). The results show that the vortex generators increase heat transfer and also the flow losses in channel, and for all vortex generators geometries there exists an optimum angle of attack between (50° and 70°) for maximum heat transfer. However the flow losses increase monotonically with the angle of attack. Results show that the winglet gives better performance than wings and pair of delta winglet performs slightly better than the pair of rectangular winglets.
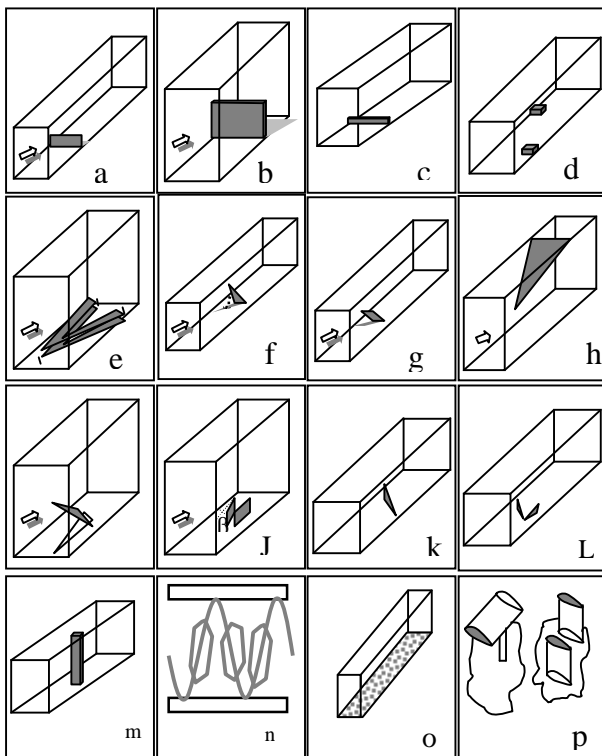

Fig. 2. Triangle and Rectangle Wings and Winglets.

2.3. Vortex Phenomenon

Davis and Moore [22], presented numerical solutions for two-dimensional time-dependent flow about rectangles in infinite domains . The numerical method utilizes a third order upwind differencing for convection and a Leith type of temporal differencing. An attempted use of a lower-order scheme and its inadequacies are also described. The Reynolds-number regime investigated is from 100 to 2,800. Other parameters that are varied are upstream velocity profile, angle of attack, and rectangle dimensions. The initiation and subsequent development of the vortex-shedding phenomenon was investigated. Passive marker particles provide an exceptional visualization of the evolution of the vortices both during and after they are shed. The properties of these vortices are found to be strongly dependent on Reynolds number, as are lift, drag, and Strouhal number. Computed Strouhal numbers were compared well with those obtained from a wind-tunnel test for Reynolds numbers below (1,000).

Yasuo Mori et al, [٢٣], studied experimentally the mechanism of symmetrical vortex shedding behind a cylinder in a uniform, upward flow by heating the wake with fine wires or by using a splitter plate or mesh. In the case of heating the wake the vortices are gradually modified from Karman vortex to symmetrical vortices with increase of heat input. Similar symmetrical vortex shedding is also observed by the increase of the splitter plate length or mesh number behind the cylinder.

An experimental investigation of a longitudinal vortex/boundary layer system was made by Eibeck and Eaton [٢٤], to understand the effects of the vortex on local convective heat transfer coefficients. Measurements in the presence of a single longitudinal vortex embedded in an otherwise two-dimensional turbulent boundary layer included local Stanton number distributions, momentum and thermal boundary layer profiles, and skin friction distributions. The local Stanton number varied, with an increase of (22) % over flat plate values in the downwash region of the vortex, and decreases of (12) % in the up wash region. The vortex imposed spanwise variations of boundary layer parameters such as thickness, wall shear, and profile shape. In spite of this, the heat transfer process was locally dominated by two-dimensional mechanisms, as evidenced by the existence of a log-region in the boundary layer, as well as the applicability of the Reynolds analogy.

The heat transfer effects on an isolated longitudinal vortex embedded in a turbulent boundary layer were examined experimentally by Eibeck and Eaton [25], for vortex circulations ranging from (0.12 to 0.86). The test facility consisted of a two-dimensional boundary-layer wind tunnel, with a vortex introduced into the flow by a half-delta wing protruding from the surface. In all cases, the vortex size was of the same order as the boundary-layer thickness. Heat transfer measurements were made using a constant-heat-flux surface with 160 embedded thermocouples to provide high resolution of the surface-temperature distribution. Three-component mean- velocity measurements were made using a four-hole pressure probe. Span wise profiles of the Stanton number showed local increases as large as 24 percent and decreases of approximately 14 percent. The perturbation to the Stanton number was persistent to the end of the test section, a length of over 100 initial boundary-layer thicknesses. The weakest vortices examined showed smaller heat transfer effects, but the Stanton number profiles were nearly identical for the three cases with circulation greater than $\Gamma/U_\infty\delta_{99}= 0.53$. The local increase in the Stanton number is attributed to a thinning of the boundary layer on the downwash side of the vortex.

Experimental studies on bodies of revolution at high angles of attack have shown that the forces and moments developed are greatly affected by the formation of rolled up vortex cores. Thus it is felt that an accurate model of the vortex would aid in the design of fuselage fore bodies or slender bodies in general. Due to geometric simplicity several mathematical models of the vortex flow over a slender, sharp-edged, delta wing have been formulated. However, these models generally ignore the entrainment effect of the vortex core, and are found to yield results which are not in agreement with experiment, thus, their extension to the more general case would be of little value. A technique referred to as the leading-edge suction analogy, has been found to yield extremely accurate results when compared with experiment. Paul [26], indented to propose a mathematical model of the vortex, which incorporates the previously ignored entrainment effect, and leads to an expression similar to the leading-edge suction analogy.

2.4. Scope of the Present Study

The aim of present study is to investigate turbulent flows in rectangular ducts using two-

shapes of VGs and different locations and dimensions, to know the effect of these small bodies on flow and heat transfer characteristics. Experimental investigations are to be undertaken in the present study. In the experimental part, none of the previous studies have tackled the problem of constant wall temperature along the duct.

Therefore, a rig is to be built to study the velocities and temperatures for a range of Reynolds number (62000-125000) so that the flow become fully development, using accurate tools and modern measurement equipments and devices that can be calibrated accurately.

Also we found correlation between the average Nusselt number and Reynolds number (62000-125000) in different vortex generator shapes (circular, square).

Thus, the layout of research can be demonstrated as follows:

1. Set up an experimental rig to measure the velocity, temperatures.
2. Study the effect of vorticities on the heat transfer on the heat exchanger.
3. Study the obstruction that can produce maximum heat transfer.

2.5. Summary

A conclusion of the available data in literatures for effect of vortex generators on heat exchanger, both wing and winglet – type vortex generators and vortex phenomena was presented. All data related to study friction factor, pressure drop, heat transfer from heat exchanger, and relation between Nusselt number and Reynolds number. From this summary and to the author's knowledge no study of the heat transfer and pressure drop through the heat exchanger by using vortex generators, circular and square shapes was conducted.
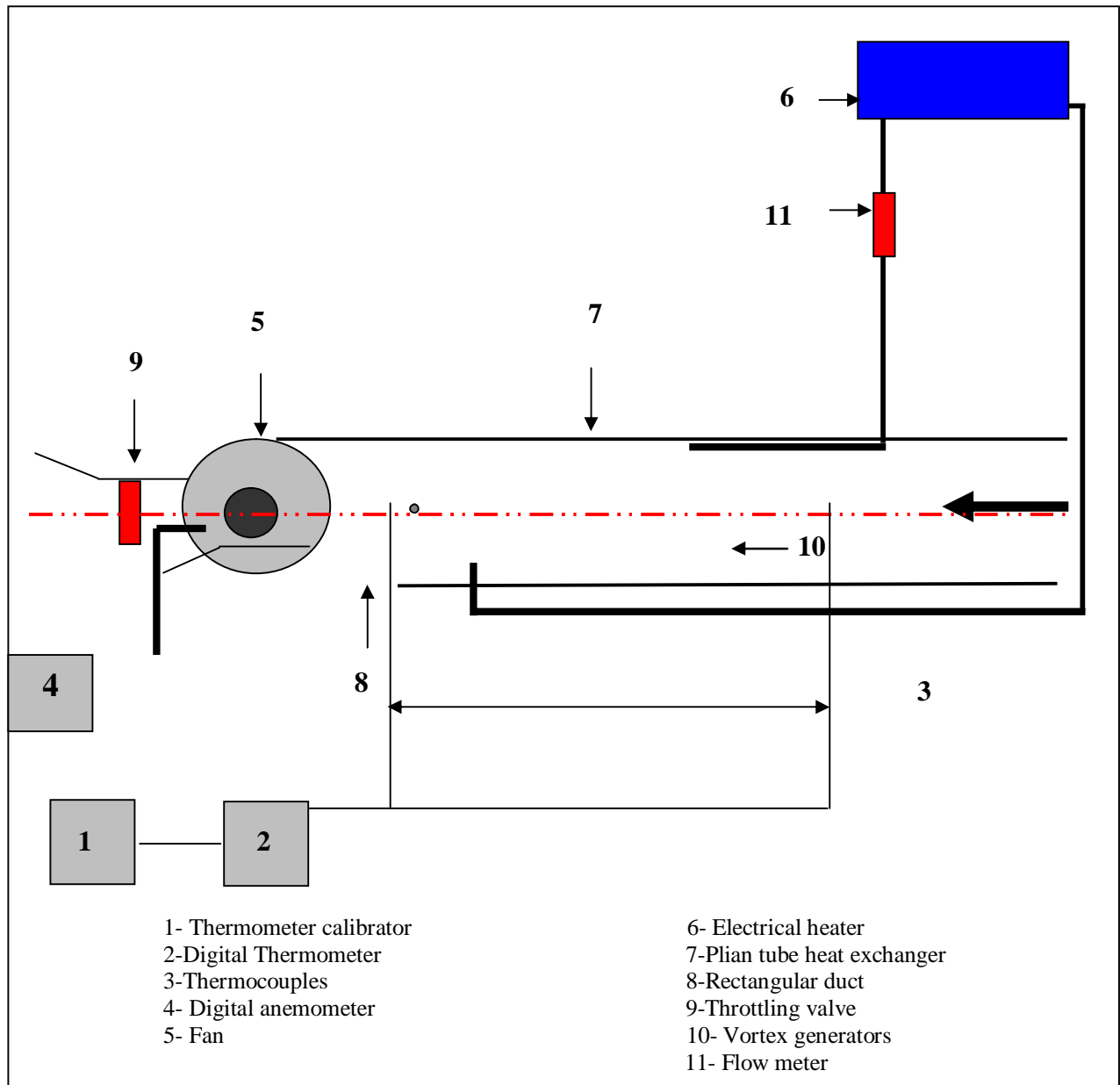
Fig. 3. Scheme Diagram.

1- Thermometer calibrator
2-Digital Thermometer
3-Thermocouples
4- Digital anemometer
5- Fan

6- Electrical heater
7-Plian tube heat exchanger
8-Rectangular duct
9-Throttling valve
10- Vortex generators
11- Flow meter

3. Experimental Work

3.1. Rig Requirement

A schematic diagram given in Figure (3) shows the experimental arrangement. The experiment was carried out at the heat transfer laboratories of the University of Technology using plain tube heat exchanger with six rows tube staggered and vortex generator. The test model was constructed from rectangular wood duct the dimensions of duct were 0.3m height and 0.15m width and 3m length, and the length of duct before the heat exchanger is 0.3 m.

3.2. Rig Description and preparation

The test rig shown in Figure (4) is designed and manufactured to fulfill the requirements of the test system for finned duct. The experimental apparatus consists basically of:

1-The airflow rates supply section.
2-The test section. (Heat exchanger).
3-The heating and control sections.
4-The measuring instruments.
5-Vortex generators.

Most of these parts are designed and manufactured during the current work, and care

was taken to prevent any air leakage between the connected parts; the rig was completely damaged and during the current work so it was rehabilitated reconstructed according to the acceptable wind tunnel standards.

Fig. 4 Rig Description.

3.3. Air Supply Equipment

Suction type axial fan shown in Figure (5) was used to supply the flow of air to the rig working section. The Axial fan [made by Tecquipment in England, se. no. w/4/20029,] is driven by A.C. motor, the flow of air is controlled by using an adjustable throttling valve mounted just at the mouth of the air intake. Since there is no need for any connection in the fan inlet and the throttling valve being fully open to obtain maximum air flow rate , the air delivered by the fan should has a uniform velocity profile with minimum turbulence level.
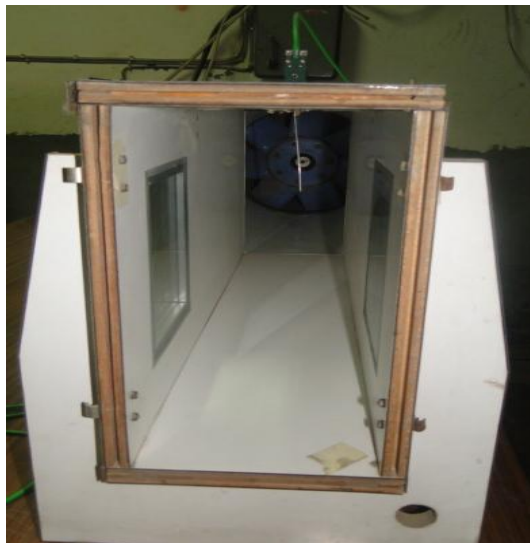

Fig. 5. Axial Fan.

3.4. Air Duct

It consist of a rectangular wood duct as shown in Figure (5) which is constructed of four section clipped tightly together. Identical entry and exist section are separated by a plain center section which can easily be replaced with the optional heat exchanger .The apparatus is supplied with the axial fan connected to the exit . The fan discharges directly to the atmosphere thought an adjustable throttle plate which can be used to vary the volume flow rate. Air flow rate measurement is computed by using a pitot static tube and manometer or anemometer, the dimensions of duct were 0.3m height and 0.15m width and 3m length.

3.5. Plain Tube Heat Exchanger

A bank of pure copper heat transfer tube arranged vertically consists of 33 tube 5/8 inch outer diameter and 1/2 inch inner diameter tube 30 cm length as shown in Figure (6) . Hot water supply and return duct connection are made by means of flexible rubber hoses and plug in connection through heat exchanger. Water temperature is measured by thermocouples.

Fig. 6. Plain Tube Heat Exchanger.

3.6. Vortex Generators

The vortex generator was used to generate the longitude vorticities to make difference in pressure between front surface of heat exchanger flow and the end surface causes enhanced heat transfer from heat exchanger. Most studies used two common shapes of winglets, (Circular and square) shapes as shown in Figure (7a&7b) . In the experimental the following things were fixed:-
There were two types of Grid vortex generator

1- One Grid consisting of (21) pieces of small circular, diameter=2.5 cm. The area of small piece of circular is (4.84) cm^2.
2- The other consisting of (21) pieces of small square, length=2.2cm. The area of small piece of square is (4.84) cm^2.

The purpose of this study is to compare the enhancement heat transfer with vortex generator and without vortex generator.

Fig. 7.b Square Vortex Generator.

3.7. Water Pump

Water Pump of [Q=60 L/min]capacity and a (20) m head is used To circulate Hot Water between heat exchanger and water heater by using flexible pipes as shown in Figure (8).

Fig. 7.a Circular Vortex Generator.

Fig. 8. Water Pump and Heater.

3.8. Supply Unit of Hot Water

Water tank of (150) liter capacity provided with two heaters each of (3) KW capacity, a thermostat is used to control water temperature at 60℃ as shown in Figure (8).

3.9. The Measuring Instruments

3.9.1. Digital Thermometer

This digital thermometer contains Pt 100 ohm thermometer and thermocouple type K/J/R/E/T thermometer. It contains also microcomputer circuit with high performance wide temperature measuring range. It is used to measure temperature. See Figure (4).

3.9.2. Digital Anemometer

This vane-type probe portable anemometer provides fast accurate readings, with digital readability and the convenience of a remote sensor separately. It is used to measure the average air velocity. The low friction ball bearing design allows free vane movement, resulting in accuracy at both high and low velocities. The sensitive balanced vane wheel rotates. Freely in response to air flows. Conventional twisted vane arms eliminate the source of unreliability, see Figure (9).

Fig. 9. Digital Anemometer.

3.9.3. Thermocouples Circuit

The thermocouple circuit consists of a digital electronic thermometer (type TM-200, serial no. 13528) as shown in Figure (4), connected in parallel to the thermocouples by leads through a thermometer, and digital thermometer Calibration (type TM-300, serial no.13645) by using only calibration digital electronic thermometer. Thermocouple (type K), this type can be used in temperature range from -200 to 1300℃,(Chromel 90 % Ni- 10% Cr ; Alumel 95%Ni- 2% Al-3%Mn).

3.9.4. Flow Meter

To measure the average flow rate of hot water , a Rota meter which is a flow meter containing a calibrated glass tube and a float [$0.2^{\vee}$ m^3/hr] and a globe valve was used to control the average flow rate of hot water, see figure (10).

Fig. 10. Flow Meter.

3.10. Calibration of Instruments

3.10.1. Thermometer Calibration

This is a two in one device including type K thermometer and type K thermocouple calibrator. It is a calibrating process device and measuring process signals. Microprocessor circuit assures high accuracy and provides special function and features. Built-in temperature linearity compensation high precision circuit is fitted with standard K input measuring socket. It is used to calibrate the other calibratable digital thermometers see Figure (4).

3.10.2. Anemometer Calibration

The vane-type rotary anemometer is calibrated just after the duct test section because of the large

cross-sectional area of the probe, in the free stream of the outlet region, for the five Reynolds numbers. The static-pitot tube with the manometer is used in that calibration, for checking. For many stations, the average velocity (U_{ave}) is calculated by integration. The average error percentage for all Reynolds numbers Range is around 2%.

3.10.3.   Thermocouples Calibration

All thermocouple were used with leads and calibrated using the melting point of ice made from distilled water as reference point and the boiling points of several pure chemical substances. The calibration results are given in Table (1) and Figure (11a &11b).

Table 1,
Experimental Accuracies.

Independent variables (v)	uncertainty interval (w)
Surface to bulk air temperature	$\pm\ 0.16\ \overset{.}{C}$
Voltage of the heater	$\pm\ 0.04$ volt
Current of the heater	$\pm\ 0.0003$ Amp
Hydraulic diameter	$\pm\ 0.0002$ m
Velocity	$\pm0.2\%$ m/s
Thermometer	$\pm\ (0.2\ \%\ +0.5\ C)$

Fig. 11. a. Thermocouple Calibration Results.

Fig. 11. b. Thermocouple Calibration Results.

3.11. Velocity Measurement

One method to measure and calculate the velocities in this research was the direct measurement by the anemometer, it is used to calculate the streamwise velocity (u_i). The velocity was determined according to [27].

These velocities were used in calculating the Reynolds number and the airflow rate. The mass flow rate for the different flows is calculated from the following:

$$\overset{\&}{m} = \int_{x_1}^{x_{Nx}} \int_{y_1}^{y_{Ny}} r \cdot u_{in} \cdot dy \cdot dx \qquad \ldots(1)$$

where the u_{in} is the inlet streamwise velocity and it is not constant across the duct height but it has a specific profile.

$$\overset{\&}{m} = 1.2 * \int_{x_1}^{x_{Nx}} \int_{y_1}^{y_{Ny}} u_{in} \cdot dy \cdot dx \qquad \ldots(2)$$

So the volumetric flow rate is:

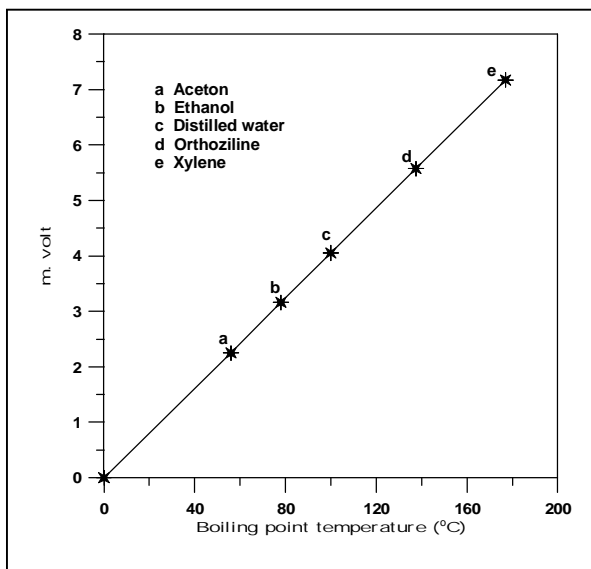$$\overset{\&}{Q} = \overset{\&}{m} / r \qquad \ldots(3)$$

3.12. Temperature Measurement

Temperature distribution at various stations and points inside the duct at inlet and outlet of water inside heat exchanger . However temperatures distribution before vortex generators and after heat exchanger in the test section, infrared thermometers and type K thermocouple. The temperature measurement devices were calibrated.

3.13. Procedure

1. Connect heat exchanger to hot water supply.
2. Set hot water temperature.
3. 3-Plant two thermocouples in air duct to measure inlet and outlet air temperature.
4. Plant two thermocouples to measure inlet and outlet hot water temperature inside heat exchanger.
5. Set water flow rate as desired.
6. Switch on fan.
7. Switch on circulation pump.
8. 8-Take reading every 50 min after steady state condition.

3.14. Data Analysis

Simplified steps were used to analyze the heat transfer process for the air flow and water in heat exchanger.
The local heat transfer coefficient can be obtained as[28]:-

$$h_x = \frac{q}{(T_s)_X - (T_b)_x} \qquad \ldots(4)$$

$q = m^{\circ} c_p \Delta T$

q=heat flux

$(T_b)_x$ = Local bulk air temperature.

$(T_s)_x$ = Local tube surface temperature.

All the air properties are evaluated at the mean film air temperature

$$(T_f)_s = \frac{(T_s)_X + (T_b)_s}{2} \qquad \ldots(5)$$

T_f = Local means film air temperature.

The local Nusselt number (Nu$_z$) then can be determined as:

$$Nu_x = \frac{h_x \times D_h}{k} \qquad \ldots(6)$$

Where:
K=thermal conductivity of air

D_h=hydraulic diameter of duct

$$D_h = \frac{4 A}{P}$$

The average values of Nusselt number Nu$_m$ can be calculated as follows:

$$Nu_m = \frac{1}{L} \int_o^L Nu_x \, dx \qquad \ldots(7)$$

The average values of the other parameters can be calculated based on calculation of average tube surface temperature and average bulk air temperature as follows:

$$\overline{T_s} = \frac{1}{L} \int_{x=0}^{x=L} (T_s)_x \quad dx \qquad \ldots(8)$$

$$\overline{T_b} = \frac{1}{L} \int_{x=0}^{x=L} (T_b)_x \quad dx \qquad \ldots(9)$$

$$\overline{T_f} = \frac{\overline{T_s} + \overline{T_b}}{2} \qquad \ldots(10)$$

$$Re_m = \frac{\rho \, u_{in} \, D_h}{\mu} \qquad \ldots(11)$$

Where; $\quad u_{in} = \dot{V}/A \quad , \quad A = LH$

All the air physical properties ρ, μ and k were evaluated at the average mean film temperature ($\overline{T_f}$).

4. Results and Discussion

4.1. Introduction

The restriction on shape and position of a duct strongly influences fluid flows along the duct.
The main results from the experimental are used in this research, for a fully developed turbulent flow in a rectangular duct for different Reynolds numbers and they are presented graphically.

4.2. Experimental Results

Experimental study was carried out at Reynolds number equal to (62000-125000) for all shapes of vortex generators. The location of the winglets was changed according to longitudinal distance to get the best location of vortex generators at X_m=0.5 cm at circular shape and X_m=2.5 at square shape.

4.3. The effect parameters on the heat transfer

Finding many parameters effect on the heat transfer coefficient, I will recogniz the Nusselt number reference to enhance the heat transfer from the heat exchanger as shown below.

4.3.1. Vortex generator shape effect

Figures (12,13,14) represent the relation between Nusselt number and flow Reynolds number at location (X=0.5, 1.5, 2.5cm) respectively, as shown Nusselt number increases higher by inserting circular and square vortex generators with respect to without turbulator but the increase in Nusselt number is shown to be highest at Reynolds number Also it indicates that the circular vortex generators at location (X=0.5,1.5 cm) increases Nusselt number with respect to the square vortex generators with ratios (28.5%, 13.5%) respectively, because the turbulence flow in the circular vortex generators greater than the square vortex generators is leading to enhancement the heat transfer in the circular shape better than the square shape . The square vortex generators at location (X=2.5 cm) increases Nusselt number with respect to the circular vortex generators with ratio (29.5%).
 The circular vortex generators at location (X=0.5, 1.5, 2.5cm) increases Nusselt number with respect to without turbulator with ratios (56%, 50%, 36%) respectively, and the square vortex generators at location (X=0.5, 1.5, 2.5cm) increases Nusselt number with respect to without turbulator with ratios (39%, 42%, 51%) respectively
For both cases the general equation of this relation is given as equations 12 and 13 for Figures 15 and 16 respectively.

$$Nu= [-21757(X/L)^2 - 4693.8(X/L) + 35.454] +$$

$$[0.855(X/L)^2 + 0.063(X/L) + 0.002]Re +$$

$$[-9 \times 10^{-6} (X/L)^2 - 6 \times 10^{-21} (X/L) + 1 \times 10^{-8}]*Re^2$$

(circular) …(12)

$$Nu= [27720(X/L)^2 - 4766.7(X/L) - 187.18] +$$

$$[-0.45(X/L)^2 + 0.066(X/L) + 0.0069] Re +$$

$$[2 \times 10^{-22} (X/L) - 2\times 10^{-8}] Re^2$$

(square) … (13)

Where:X: location of vortex generator.
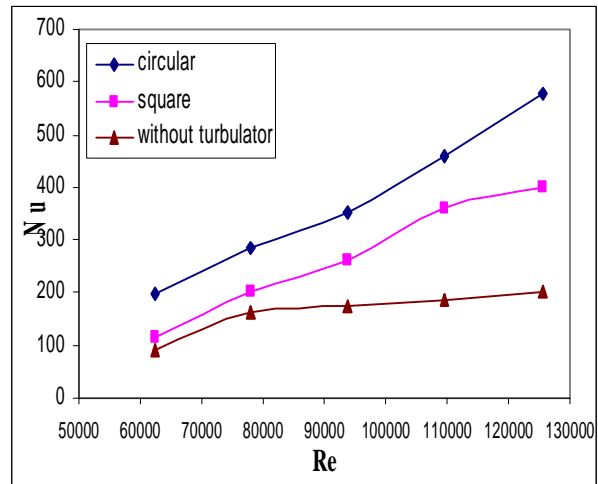L: the distance before heat exchanger.

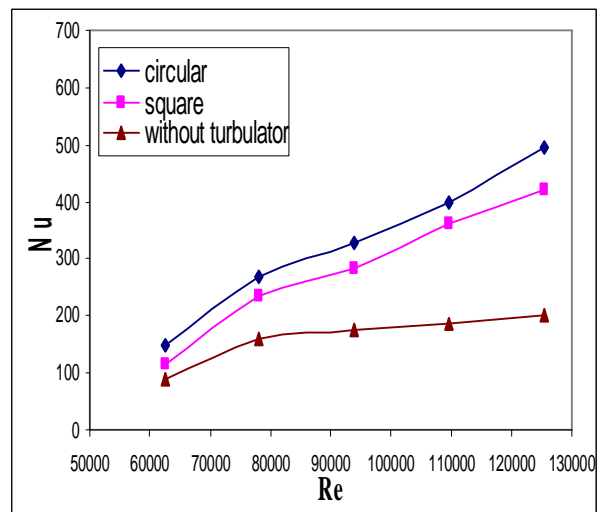**Fig. 12. Experimental Variation of Nusselt Number with Reynolds Number at location (X=0.5 cm) for Vortex Generators.**

Fig. 13. Experimental Variation of Nusselt Number with Reynolds Number at location (X=1.5 cm) for Vortex Generators.
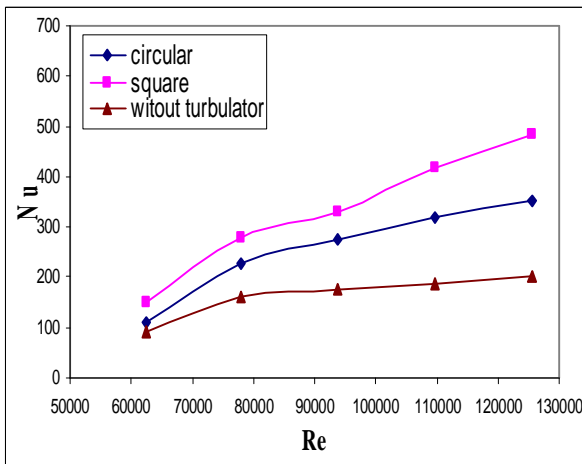
Fig. 14. Experimental Variation of Nusselt Number with Reynolds Number at location (X=2.5 cm) for Vortex Generators.
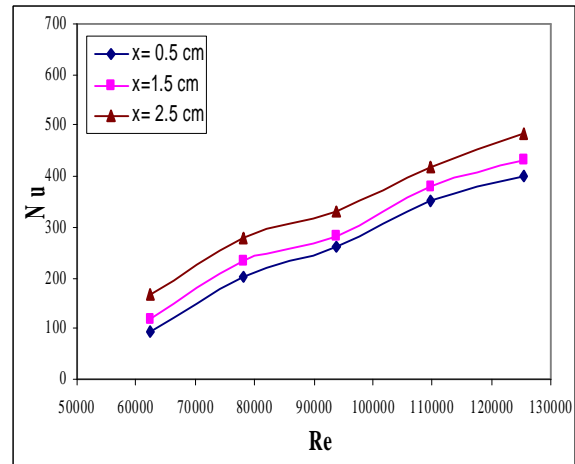
4.3.2. Location of vortex generator

Figures (15, 16) show the relation between Nusselt numbers (with vortex generators, and without vortex generators) for both cases (circular and square) respectively and flow Reynolds number. As shown in these Figures the behavior is the same as that obtained in Figure (12, 13, and 14). But the heat transfer process in circular shape is better than in square shape at location (X=0.5, 1.5 cm) , the square vortex generators at location (X=2.5 cm) is better than circular shape because the square vortex generators in this location provide turbulence flow better than the circular shape as shown in figures.
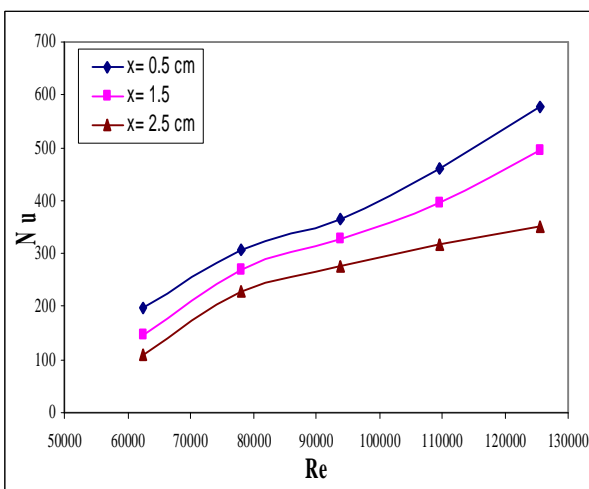
Fig. 15. Experimental Variation of Nusselt Number with Reynolds Number at Circular Vortex Generators.

4.3.3. Reynolds Number

Figures (12, 13, 14, 15, and 16) show that Nusselt numbers are enhanced with Reynolds number increasing for all cases due to increase the inlet velocity (u_{in}) and that will increase the heat transfer from the heat exchanger.

5. Conclusion and Recommendations

5.1. Conclusion

Experimental study for heat transfer around heat exchanger using vortex generators (circular and square) in turbulent flow has been done. In the experimental study, an apparatus was set up to measure the velocity and temperatures around the heat exchanger with constant heat flux using two shapes of vortex generators at a fixed point.

1- There is an effect for the shapes of vortex generators on heat transfer,Temperatures and velocity distribution.
2- Circular shape is the best shape for enhancing heat transfer and the square shape gives minimum heat transfer in the present work.
3- Heat transfer is enhanced (36-56) % when Circular shapes of vortex generators are used.
4- Heat transfer is enhanced (39-51) % when Square shapes of vortex generators are used.
5- Heat transfer increases by using Circular shape when the distance of vortex generators is equal to ($X_m= 0.5, 1.5$ cm) before heat exchanger.

6- Heat transfer increases by using square shape when the distance of vortex generators is equal to (X_m= 2.5 cm) before heat exchanger.

5.2. Recommendation for future work

The following points can be recommended for future work.
1. Numerical investigation can be extended to consider 2-D or 3-D problems.
2. Other shapes of vortex generators can be investigated numerically and experimentally (ellipsoidal, trapezoidal, triangle, rectangular)
3. New fixed location for vortex generators and angle (in front of heat exchanger) can be used.
4. The effect of area can be taken into consideration.
5. Replace air with steam and study its characteristics.
6. Compare the turbulence model used in this research with LES (large eddy simulation) turbulence model.
7. Increasing the number of vortex generators fixed in each study.

Notation

Symbol	Description	Unit
A	Tube surface area	m^2
C_p	Specific heat at constant pressure	J/Kg.ºC
D_h	Hydraulic diameter	m
h	Coefficient of heat transfer	W/m^2.ºC
K	Thermal conductivity	W/m.ºC
L	Length of tube	m
m	Volumetric flow rate	m^3/s
T	Air temperature at any point	ºC

Symbol	Description	Unit
T_b	Bulk air temperature	ºC
T_f	Mean film air temperature	ºC
T_i	Air temperature at tube entrance	ºC
T_s	Tube surface temperature	ºC
u	Axial velocity component	m/s
u_{in}	Axial velocity at tube entrance	m/s
X_m	Longitude distance	Cm

Dimensionless Groups

Symbol	Description	Equation
Nu	Nusselt number	$\dfrac{hD_h}{k}$
Pr	Prandtal number	$\dfrac{mC_p}{k}$
Re	Reynolds number	$\dfrac{u_i D_h}{n}$

Subscript

Symbol	Meaning
s	Surface
a	Air
i	Inter
h	Hydraulic diameter
x	Local
f	Film
m	Meter

Greek letters

Symbol	Description	Unit
μ	Dynamic viscosity	Kg/m.s
ν	Kinematics viscosity	m^2/s
ρ	Air density at any point	Kg/m^3

Abbreviation

Symbol	Description
B.L	Boundary layer
V.G	Vortex generator
H.E	Heat exchanger
DX	Horizontal Distance of Winglet
DY	Vertical Distance of Winglet

6. References

[1] Geiser, P. and Kotteke, V., "Pressure loss, local coefficient of Heat transfer in plat and finned tube heatexchanger",Germany.www.link.aip.org/link/JHTRAO/126/826-pdf, (2000).

[2] Fiebig, M. Brocmeire, U Mitra, N. K. and Guntremann, T."Structure of velocity and

temperature field with longitudinal vortex", Numerical heat transfer parts a, Vol.15, PP.281-302, (1989).

[3] Kreith, F. and Botin, M. S., "Principles of heat transfer", Fifth Edition, (1997).

[4] T.Kuppan, "Heat Exchanger Design", Hand Book, PP.3, (2000).

[5] Tiwari, S. Prasad,P. L. N. And Biswas, G., "A numerical study of heat transfer in fin –tube heat exchanger using winglet – type vortex generators in common flow down configuration" progress in CFD, Vol.3, No.1, PP. 32-41,(2003).

[6] Sohankear, A. and Davidson, L., "Numerical study of heat and flow on a plat –fin heat exchanger with vortex generators", Begell house, Inc. Turbulence heat mass transfer, (2003).

[7] Sohal, M. S. K Torii, K. O,Brien, J. and Biswas, G. , "Application of vortex generators and oval tube to enhance performance of air – cooled condenser and other heat exchanger", Idaho National Engineering and Environmental Laboratory, (2001). Sohalms@inel.gov

[8] Sohal, M. S. and O, Brien, J., "Improving air cooled condenser performance using winglet and oval tube in a geothermal power plan", Geothermal resources council transaction, Vol.25, August, PP.26-29, (2001).

[9] Sabah Tarik Ahmed, "Numerical & Experimental Study on Heat Transfer for Enhancement by Vortex Generator", Ph. D. Thesis, Mech. Eng. Dept., University Of Technology, (2001).

[10] C. M. B. Russell, T. V. Jones and G. H. Lee, " Heat Transfer Enhancement Using Vortex Generators", Heat Transfer Proceedings Of The Seventh International Heat Transfer Conference, FC50, pp.283-288,(1982).

[11] J. R. Maughan and F. P. Incropera, "Regions of Heat Transfer Enhancement for Laminar Mixed Convection in a Parallel Plate Channel", Int. J. Heat Mass Transfer, Vol. 33, No.3, pp.555-570,(1990).

[12] V. K. Migai and I. S. Nosova, "Decreasing Vortex Losses in Channels", Thermal Engineering, Vol.26, No.7, pp.423-425, (1979).

[13] V. Kottke, " Taylor-Goertler Vortices and Their Effect on Heat and Mass Transfer ", Heat Transfer Proceedings Of The Eighth

International Heat Transfer Conference, Vol.3, pp.1139-1144,(1986).

[14] L.C.G Pimentel, R.M.Cotta, S.Kakac, "Fully developed turbulent flow in ducts with symmetric and asymmetric rough walls", Chemical Engineering Journal, Vol.74, PP.147-153, (1999).

[15] Chien-Nan Lin,Jiin-Yuh Jang, "conjugate Heat Transfer and Fluid Flow Analysis in Fin-Tube Heat Exchangers with Wave-Type Vortex Generators ",Journal of Enhanced Heat Transfer,Vol.9,PP.123-136, (2002).

[16] S.M. Pesteei, P.M.V. Subbarao, R.S. Agarwal,"Experimental study of the effect of winglet location on heat transfer enhancement and pressure drop in fin-tube heat exchangers", Applied Thermal Engineering vol.25, pp.1684–1696, (2005).

[17] K. Torii, K.M. Kwak, K. Nishino, "Heat transfer enhancement accompanying pressure-loss reduction with winglet-type vortex generators for fin-tube heat exchangers", international Journal of Heat and Mass Transfer, Vol .45, pp.3795–3801, (2002).

[18] AJoardar, A.M. Jacobi, "Impact of leading edge delta-wing vortex generators on the thermal performance of a flat tube, louvered-fin compact heat exchanger", International Journal of Heat and Mass Transfer, Vol.48, pp.1480–1493, (2005).

[19] W. R. Pauley and J. K. Eaton, " The Effect of Embedded Longitudinal Vortex Arrays on Turbulent Boundary Layer Heat Transfer", Transactions Of The ASME, Journal Of Heat Transfer, Vol.116, pp.871-878,(1994).

[20] L. B. Wang, F. Ke, S. D. Gao and Y. G. Mei, "Local And Average Characteristics Of Heat / Mass Transfer Over Flat Tube Bank Fin With Four Vortex Generators Per Tube", Transactions Of The ASME, Journal Of Heat Transfer, Vol.124, pp.546-552,(2002).

[21] Tiggelbeck, St. Metra, N. K. and Fiebg, M., "Comparison of wing –type vortex generators for heat transfer enhancement in channel flow", ASME, Vol.116, PP 880-885, (1994).

[22] R. W. Davis and E. F. Moore, "A Numerical Study of Vortex Shedding from Rectangles", J. Fluid Mech. Vol.116, pp.475-506, (1982).

[23] Yasuo Morl, Kunjo Hijkikata and Takayoshi Nobuhara, "A Fundamental

Study of Symmetrical Vortex Generation Behind a Cylinder By Wake Heating or by Splitter Plate or Mesh", Int. J. Heat Mass Transfer, Vol.29, No.8, pp.1193-1201, (1986).

[24] Pamela A. Eibeck and John K. Eaton, "The Effects of Longitudinal Vortices Embedded in a Turbulent Boundary Layer on Momentum and Thermal Transport", Proceedings of The Eighth International Heat Transfer Conference, Vol.3, pp.1115-1120, (1986).

[25] P. A. Eibeck and J. K. Eaton, "Heat Transfer Effects of a Longitudinal Vortex Embedded in a Turbulent Boundary Layer", Transactions of The ASME, Journal of Heat Transfer, February, Vol.109, pp.19-24, (1987).

[26] Paul L. Coe JR, "A Vortex Entrainment Model Applied to Slender Delta Wings", AIAA Journal, January, Vol.12, No.1, pp.110-112, (1974).

[27] Fuijta, H. and Yokosava, H., "The numerical prediction of fully developed turbulent flow and heat transfer in a square duct with two roughened facing walls", Nagoya University, Nagoya, Japan, (1984).

[28] Mohmood, G.I., Ligrani, P.M., and Won, S.Y. ,"Spatially-Resolved heat transfer and flow structure in a rectangular channel 45oangled rib turbulators", Proceedings of ASME Turbo Expo, (2002)

دراسة عملية عن تأثير شكل وموقع مولدات الدوامات عند مدخل المبادل الحراري

وسام عبد كاظع

قسم هندسة المكان والمعدات / الجامعة التكنولوجية

البريد الألكتروني: wisam_bd@yahoo.com

الخلاصة

دراسة عملية أجريت لفحص تأثير مولد الدوامات (الشبكة الدائرية ، الشبكة المربعة) على الجريان و انتقال الحرارة عند مواقع (X = 0.5, 1.5, 2.5 cm) قبل مبادل حراري ضمن مدى لرقم رينولد 125000 <Re < 62000 و فيض حراري $3000 \leq q \leq 8000$ W/m^2.في الدراسة العملية تم نصب و صيانة جهاز مختبري لقياس السرعة و درجة الحرارة حول المبادل الحراري.

أظهرت النتائج أن لوجود مولد الدوامات اثّر كبير على تحسين انتقال الحرارة ويعتمد هذا على شكل المولد وموقعهِ. الشبكة الدائرية هي الأفضل لعملية نقل الحرارة عند موقع [X$_m$=0.5 cm] قبل المبادل الحراري. الشبكة المربعة هي الأفضل لعملية نقل الحرارة عند موقع [X$_m$=2.5 cm] قبل المبادل الحراري.

قورنت النتائج العملية في حالة وجود مولد الدوامات مع عدم وجود مولد الدوامات. أظهرت هذه المقارنة تحسن في انتقال الحرارة حول المبادل الحراري بنسب(36% ,50% , 56%) عند مواقع (X=0.5, 1.5, 2.5cm) على التوالي بأسنخدام مولد الدوامات الدائري الشكل نسبة الى عدم وجود عوائق جريان،وانتقال الحرارة حول المبادل الحراري يتحسن بنسب (51% ,42% , 39%) عند مواقع (X=0.5, 1.5, 2.5cm) على التوالي بأسنخدام مولد الدوامات المربع الشكل نسبة الى عدم وجود عوائق جريان.

Channel Estimation and Prediction Based Adaptive Wireless Communication Systems

Khalifa A. Salim*   **Mohammed A. Abdalla****

*Department of Information and Communication Engineering/Al-Khawarizmi College of Engineering/
University of Baghdad
** Department of Information and Communication Engineering/College of Information Engineering/
University of Al-Nahrain
* Email: Khalifa.kcebu@uobaghdad.edu.iq
* Email: mohammedalmushdany@yahoo.com

Abstract

Wireless channels are typically much more noisy than wired links and subjected to fading due to multipath propagation which result in ISI and hence high error rate. Adaptive modulation is a powerful technique to improve the tradeoff between spectral efficiency and Bit Error Rate (BER). In order to adjust the transmission rate, channel state information (CSI) is required at the transmitter side.

In this paper the performance enhancement of using linear prediction along with channel estimation to track the channel variations and adaptive modulation were examined. The simulation results shows that the channel estimation is sufficient for low Doppler frequency shifts (<30 Hz), while channel prediction is much more suited at high Doppler shifts with same SNR and target BER=10^{-4}. It was shown that the performance at higher Doppler frequency shifts (>30Hz) was improved by more than 2dB over channel estimation at target BER=10^{-4} and 32QAM constellation used.

Keywords: channel estimation, adaptive communication.

1. Introduction

Wireless communications is an emerging field, which has seen enormous growth in the last several years [1]. The transmission performance and throughput of wireless communication systems is limited due to random variation of the channel. The exponential growth of the internet had resulted in an increased demand for new methods to obtain high capacity wireless networks. The wireless radio channel poses a severe challenge as a medium for reliable high-speed communication. It is not only susceptible to noise, interference, and other channel impediments, but these impediments change over time [2].

The basic idea behind adaptive transmission is to maintain a constant Signal to Noise Ratio (SNR). Thus, without sacrificing Bit Error Rate (BER), these schemes provide high average spectral efficiency by transmitting at high speeds under favorable channel conditions, and reducing throughput as the channel degrades [3]. Extensive research work was carried to improve the transmission rate over wireless link and efficient use of allowable bandwidth, using Adaptive transmission techniques, such as adaptive modulation, channel coding, power control, and antenna diversity [4,5,6]. The transmission scheme is selected relatively to the channel characteristics [7]. For very slowly fading channels, outdated CSI is sufficient for reliable adaptive communication while for faster fading, even small delay will cause significant degradation of performance since channel variation due to large Doppler shifts usually results in a different channel at the time of transmission than at the time of channel estimation. Due to unavoidable delays involved in signal estimation, feedback transmission, and

modulation adjustment; the adaptation needs to be based on predicted channel rather than estimated one [7].

The rest of the paper is organized as follows. In the next section M-ary Quadrature amplitude modulation MQAM technique was presented. Wireless channel modeling, estimation, prediction are discussed in section 3، system architecture and simulation in section 4 and results and conclusions are discussed in section 5.

2. M-ary Quadrature Amplitude Modulation MQAM

Spectrum is the most precious commodity in wireless communications. Along with SNR, it determines the data rate at which the information can be transmitted.

In spectrally efficient M-ary QAM (MQAM), there are a total of (M) possible states for the signal with transition from any state to any other state at every symbol time. Since M=2^m, *m* bits per symbol can be sent. In Adaptive MQAM the transmission parameters are varied according to variation of the channel state.

For every modulation mode, its error probability is directly related to the received SNR. The symbol error rate (SER) of MQAM is given as [8]:

$$P_{s,MQAM}(\gamma) = \frac{2(\sqrt{M}-1)}{\sqrt{M}} Q\left(\sqrt{\frac{3}{M-1}\gamma}\right) \qquad \ldots(1)$$

Where (γ) is the received SNR. This approximation to the error probability is good for all values of *M*. When the Gray coding is used in the mapping of bits to constellation symbol, the equivalent bit error rate (BER) for MQAM is well approximated by [8]:

$$P_{b,MQAM}(\gamma) = \frac{1}{log_2\sqrt{M}} P_{s,MQAM}(\gamma) \qquad \ldots(2)$$

In adaptive MQAM system, modulation is selected according to the channel state which is obtained in the form of Signal to Noise Ratio.

3. Channel Modeling

Unreliable wireless communication channel is resulted due to temporal and spatial variations of the received signal [8]. Besides the path loss, shadowing, and multipath fading the inherent noise from the receiver's electronics and

interference from competing transmissions complicated the recovery of the original signal.

Multipath fading is the dramatic variation in signal power that occurs when the received signal is a sum of multipath components each with independent amplitude, phase, and frequency components. Fading is caused by a phenomenon known as the Doppler Effect [8].

$$f_d = f_c \frac{v}{c} \cdot \cos\theta = f_{dmax}\cos\theta \qquad \ldots(3)$$

Where f_c is the carrier frequency, θ is the angle of arrival of the received signal, v is the relative velocity, and f_{dmax} is the maximum Doppler frequency. The received signal was modeled as a sum of non-resolvable multipath components each with independent amplitude, phase and frequency components. The channel is thus modeled in a complex baseband as [9,10].

$$c(t) = \sum_{i=1}^{N} A_i \cdot e^{j(2\pi f_{di}t+\theta_i)} \qquad \ldots(4)$$

Where N is the number of scatterers, A_i is the amplitude, and f_{di} is the Doppler frequency shift of the ith complex sinusoid. Figure(1) shows a typical Rayleigh fading channel simulated over different Doppler frequency shifts. The multipath fading channel was modeled as a linear finite impulse response FIR filter using MATLAB7.6. The envelope of the channel was faded throughout the channel samples. The fading rate is highly dependent upon Doppler frequency shift.
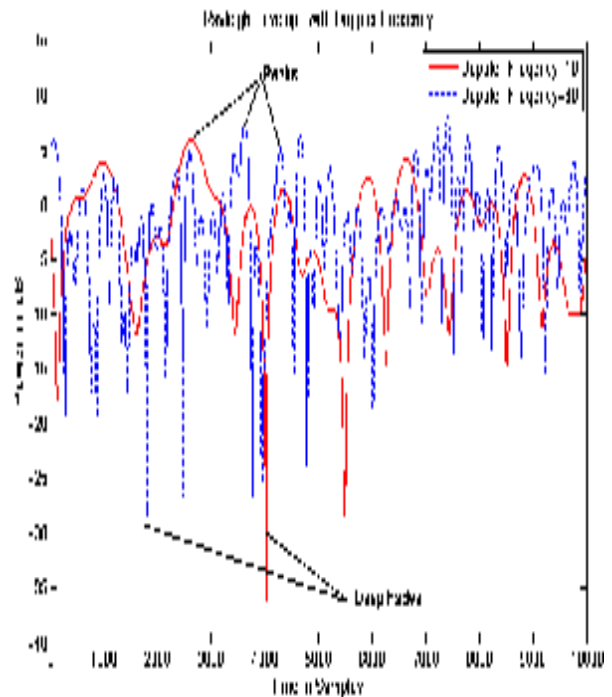

Fig. 1. Rayleigh Fading Envelope.

4. Proposed System Architecture

Figure (2) shows the proposed system block diagram. Where r(t), s(t), c(t) and n(t) is the received, transmitted, channel and noise signal respectively.

A pilot symbol which does not convey useful information is inserted every Lth channel symbol for real time channel monitoring, where each frame starts with a pilot symbol. The frame length (L) can be adjusted depending on the channel quality. The proposed system uses bandwidth efficient MQAM modulation technique with different levels. The randomly generated symbols are first mapped into M possible phases using Gray coding.
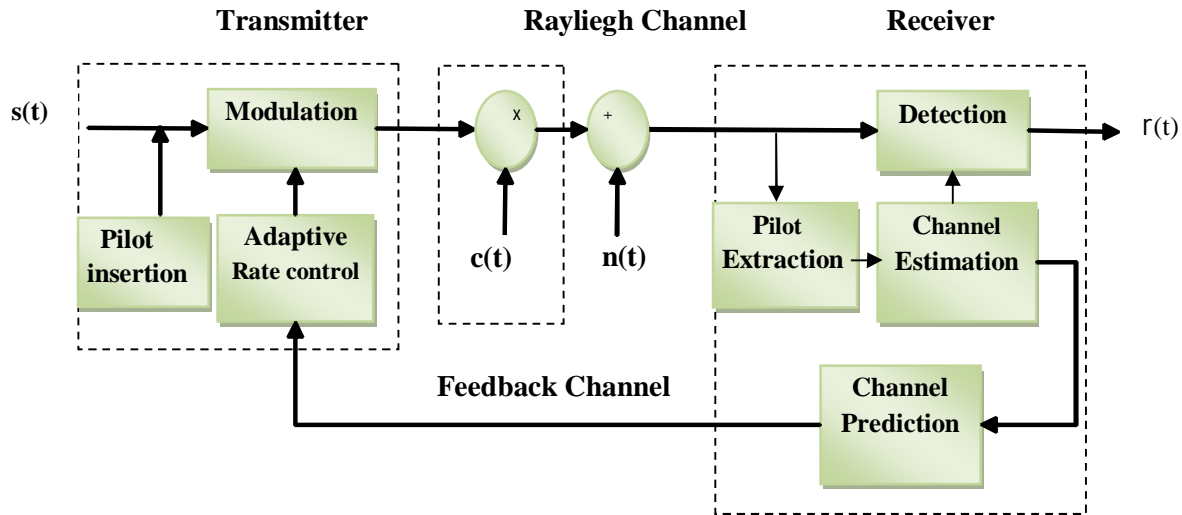
Fig. 2. System Architecture.

Received pilot symbols are extracted and used for channel estimation. The modulated symbols are then converted back to baseband bits with appropriate demodulation and Gray decoding. Coherent demodulation is used in order to achieve an undistorted bit stream. In order to cope with channel variations, the received data are fed through a baseband equalizer to reduce signal distortion. It is worthy to note that perfect clock and carrier recovery is assumed.

The estimated channel values are fed back to the transmitter to adjust the transmission mode suitable for the channel state at the transmission time.

4.1. Adaptive Modulation Boundaries

Switching between different modulation schemes was based on BER threshold which is directly related to the channel SNR, at the receiver.

Recall equation (2) SNR can be found as:

$$\gamma = 10 * log_{10} \frac{\left(Q^{-1}\left(\frac{P_{b,MQAM}(\gamma)*\sqrt{M}*log_2\sqrt{M}}{2(\sqrt{M}-1)}\right)\right)^2}{3/(M-1)} \dots(5)$$

Where Q^{-1} is the inverse of the Q-function. Proper switching boundaries are decided based on target BER selected specified depending on the type of information to be transmitted over the channel (voice, video, data,…etc). This means that the system will try to keep a BER lower than a target BER with the most spectrally efficient modulation scheme whenever possible. Figure (4) shows the BER performance for MQAM over AWGN channel with target BER=10^{-3}.
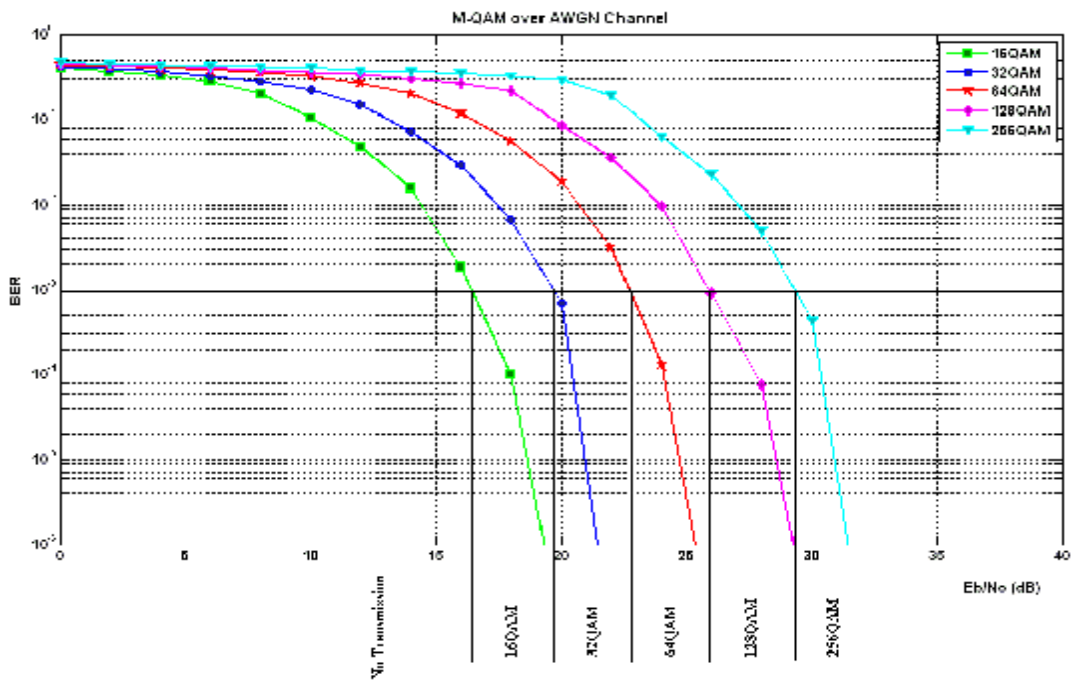
Fig. 4. BER Performance for MQAM in AWGN Channel with Threshold BER=10^{-3} .

Different modulation techniques were simulated over a Rayleigh fading channel with different Doppler frequency shifts. Fig. (5) and Fig. (6) show the BER performance for 64QAM and 256QAM over Rayleigh fading channel.
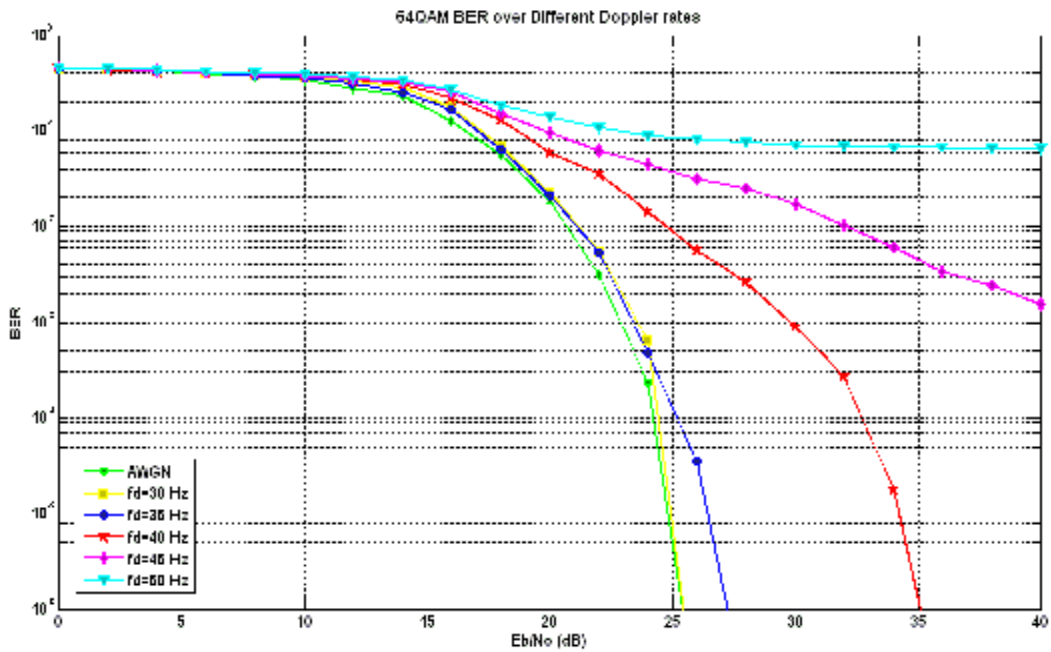

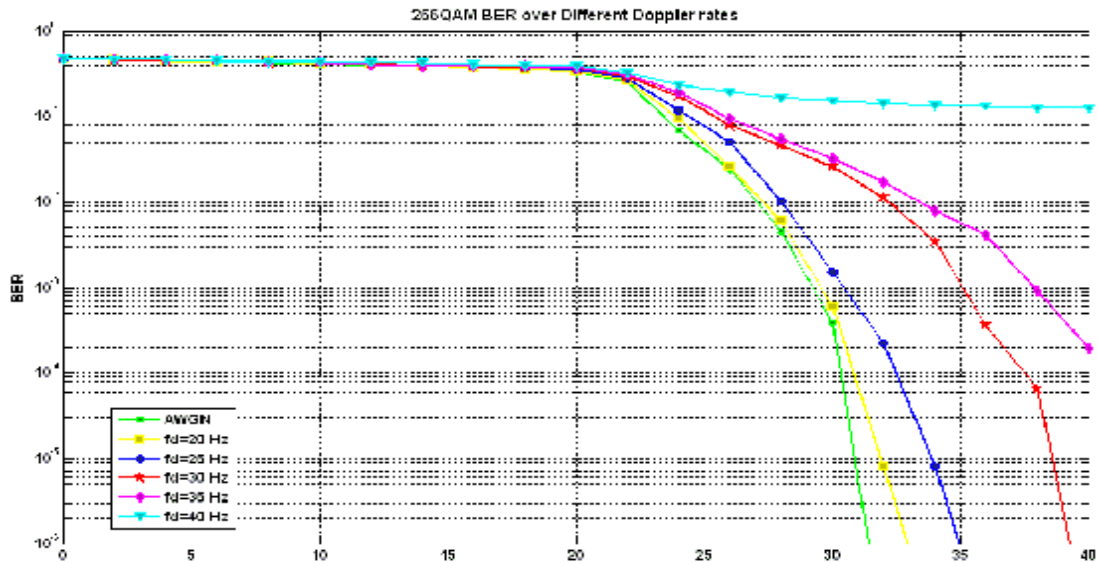**Fig. 5. 64QAM BER Performance Over Rayleigh Channel .**

Fig. 6. 256QAM BER Performance over Rayleigh Channel .

4.2. Channel Estimation

The ultimate goal at the receiver is to recover the transmitted signal that was subjected to both time varying attenuation and phase distortion. Using pilot symbols accurate channel values can be obtained at the pilot times. In order to obtain the channel impulse response, the channel values can be interpolated. FFT-based interpolation approach was used to interpolate in between channel values.

The input data to the channel estimator is the ratio of the received pilot symbols to the known pilot symbols g(n) [7]. This factor gives a measure of the distortion that the pilot symbol has undergone due to the channel fading.

$$G(K) = \sum_{n=0}^{N_p-1} g(n)\exp\left(-\frac{j2\pi nk}{N_p}\right) \qquad \ldots(6)$$

Where N_p is the number of pilot symbols used to create channel estimate.

Both SNR and the Doppler frequency shift have a strong impact on the performance of channel estimation and hence rate adaptation. The effect of different values of Doppler frequency shift on channel estimation was simulated as shown in Figure (7).
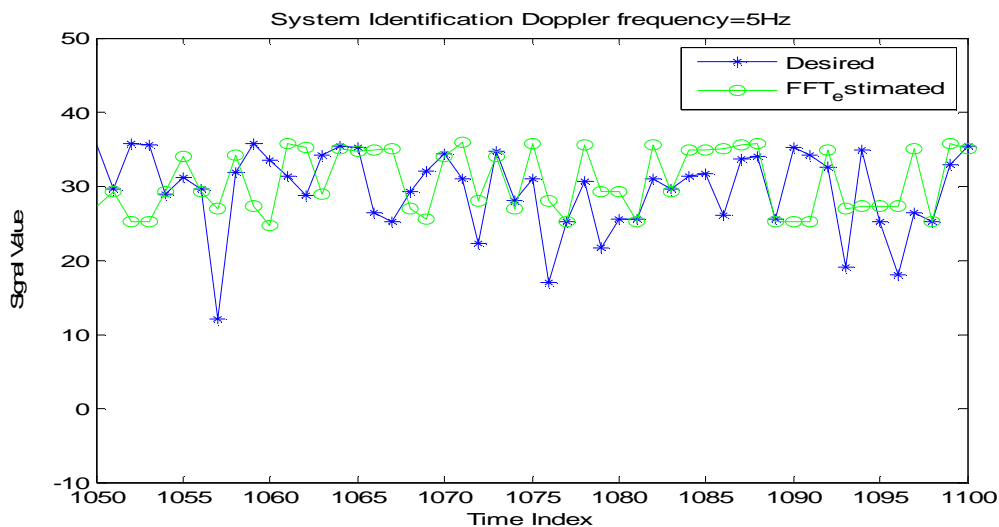
a. Doppler Frequency= 5 Hz.
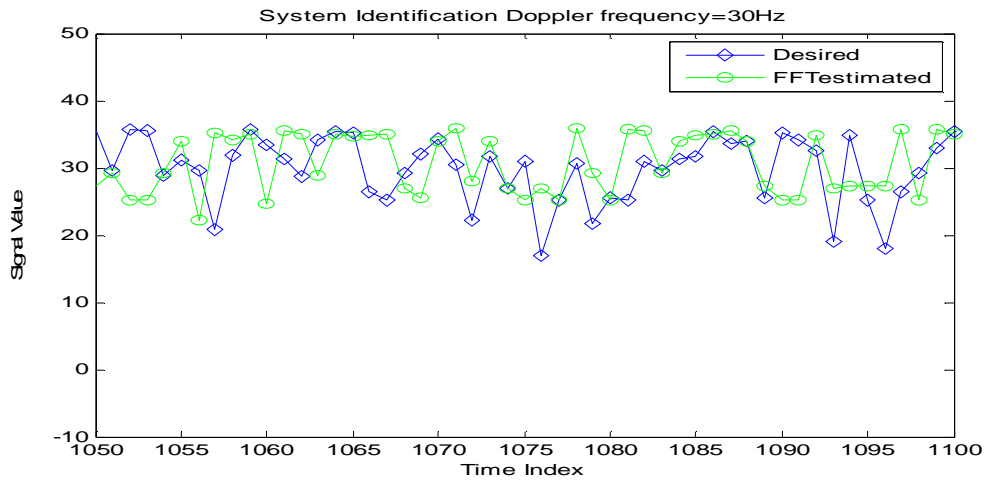
b. Doppler Frequency=30 Hz.
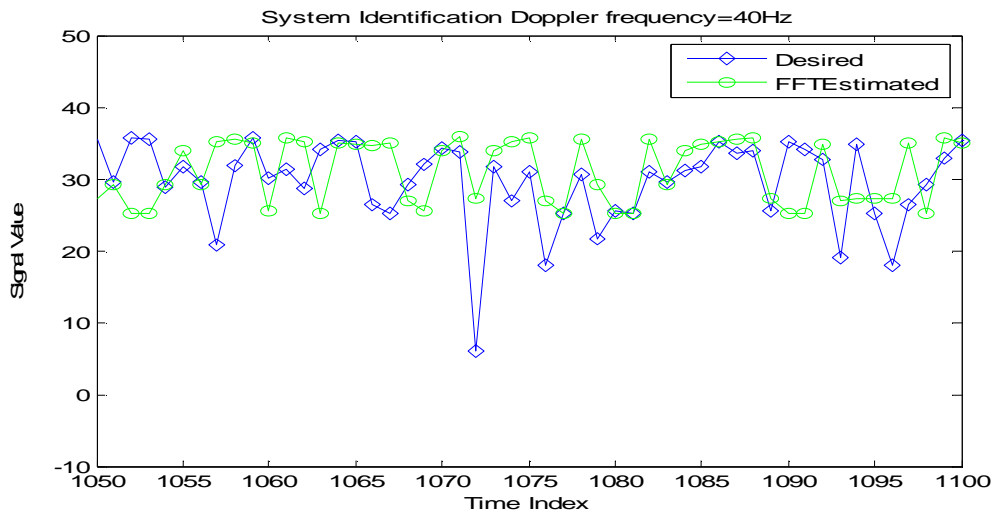
c. Doppler Frequency=40 Hz

Fig. 7. FFT Estimation of Signal Transmitted over Rayleigh Fading Channel.

4.3. Channel Prediction

In channel prediction, the future power level of the channel can be estimated using past and present channel samples [11].

Unlike AWGN the channel is correlated from sample to sample. Therefore, advantage of the deterministic properties can be taken and what the value of the channel will be at a later time can be predicted. In the linear prediction (LP) model, the current sample is approximated by a linear combination of past samples of the input signal [10,12,13]:

$$\grave{c}_n = \sum_{j=1}^{p} d_j \, c_{n-j} \qquad \qquad \ldots(7)$$

Where $\grave{c}_n$ is the predicted value based on the linear combination of (p) previous values (c_{n-j}) multiplied by the prediction coefficients (d_j). And the error generated by this estimate is [14]:

$$e_n = c_n - \grave{c}_n \qquad \qquad \ldots(8)$$

Where c_n is the true channel value.

In order to predict multiple samples in the future, the latest predicted sample is just treated as an actual sample. In linear prediction the state of the channel will be up to date at the time the transmitter receives the control information from the receiver hence propagation delay of the feedback channel will be less of a problem.

In order to predict the Rayleigh fading channel, channel estimation followed by linear prediction will be employed. A linear predictor is used to predict the channel status based on the outdated estimates.

Figures from (8) to (10) show the prediction of future channel values. The prediction efficiency is depending on the number of symbols that could be predicted ahead. As the number of symbols increases, the accuracy of the prediction would be decrease.
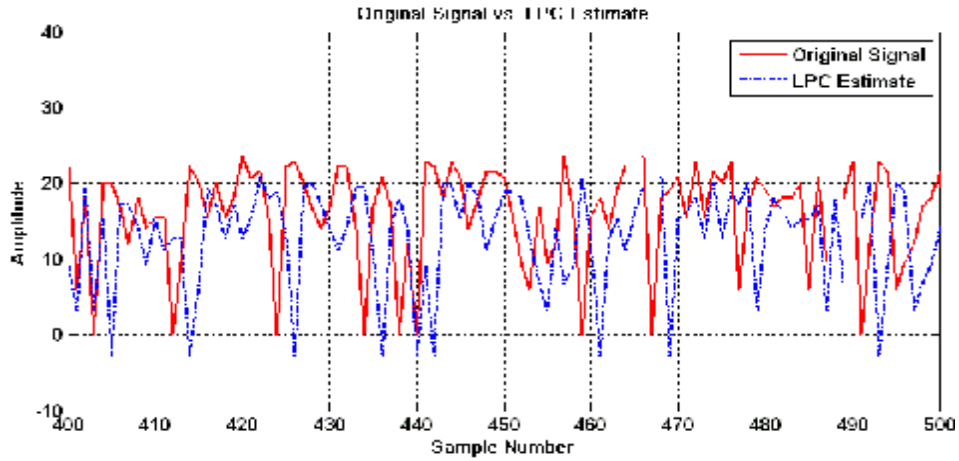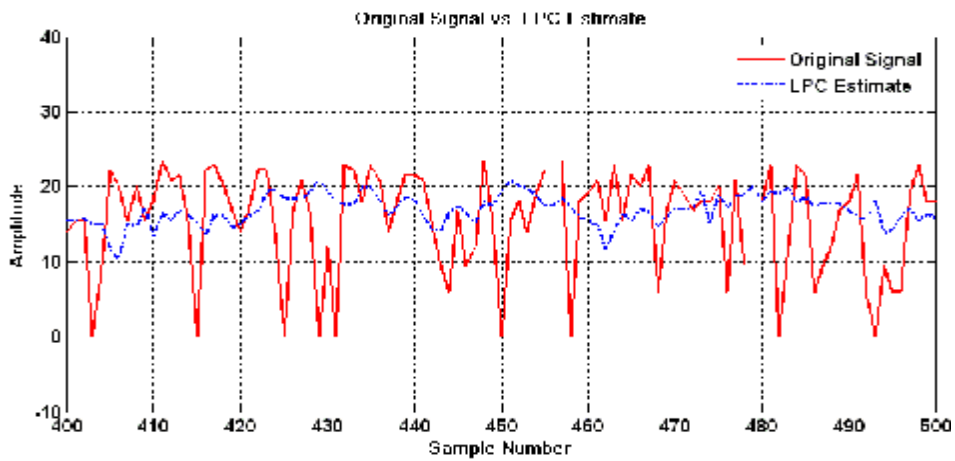

Fig. 8. Linear Prediction for 1 Symbols Ahead.

Fig. 9. Linear Prediction for 10 Symbols Ahead.
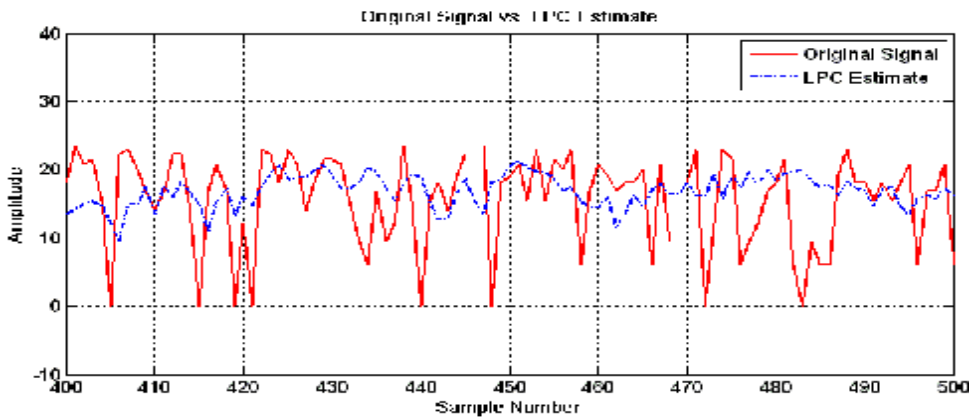
Fig. 10. Linear Prediction for 20 Symbols Ahead.

BER performance of 64QAM and 256QAM simulated over predicted channel with different prediction depth (10 and 20 samples ahead) is shown in Fig. (11) and Fig. (12).
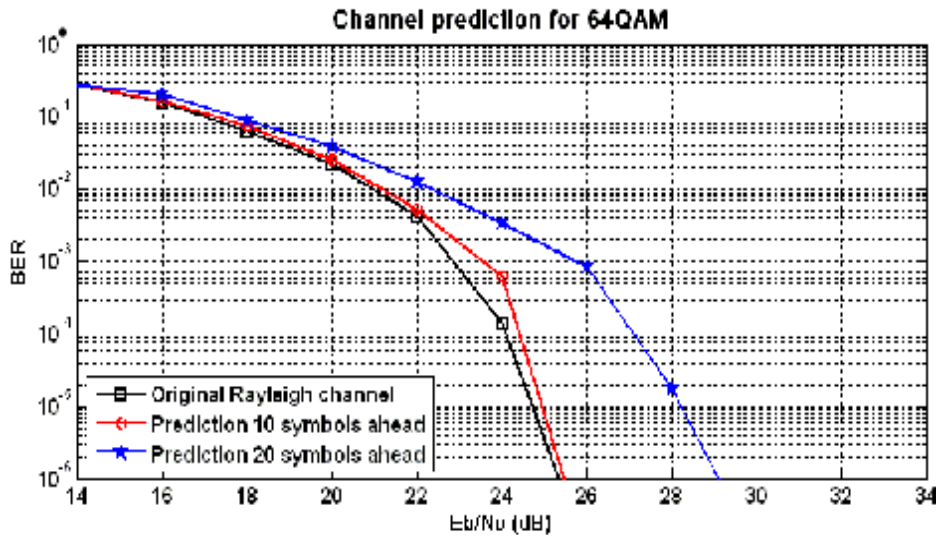
Fig. 11. 64QAM BER Performance for Predicted Rayleigh Fading Channel .
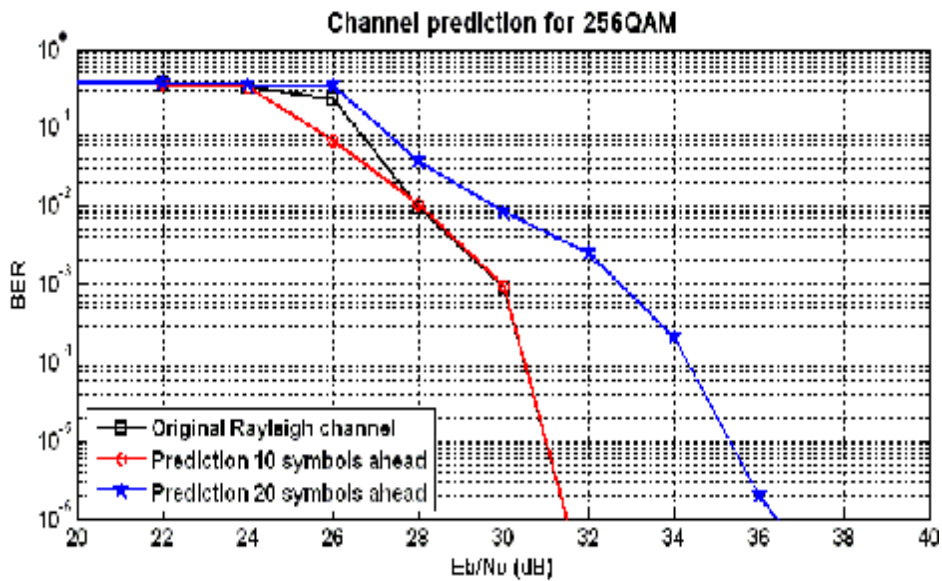
Fig. 12. 256QAM BER Performance for Predicted Rayleigh Fading Channel .

5. Results and Conclusions

It is worthy to note that the channel estimation and prediction at the receiver side differ from the original Rayleigh channel because of the error due to estimation and prediction process. As Doppler frequency increases, the BER also increases because of the deep fades that occur on Rayleigh channel during data transmission.

From previous results it can be concluded that the BER performance over predicted channel with 10 symbols ahead is better than the BER performance over predicted channel with 20 symbols ahead since as farther as many samples predicted, the less accuracy of the channel will be observed because of accumulated error.

Figures (13-14-15) show the BER performance for 32QAM, 64QAM and 256QAM constellations with different values of Doppler frequency shift for each case simulated over original, estimated, and predicted Rayleigh fading channels.

The results clearly reveal that the channel estimation was sufficient for low Doppler

frequency shifts (<30 Hz). At higher Doppler shifts the channel estimator fails to track the channel variations due to high fading rate, while channel prediction is much more suitable at high Doppler shifts and same SNR.

Channel prediction based on the estimated channel samples was simulated and tested for target BER=10^{-4}. It was shown that the performance at higher Doppler frequency shifts was improved by more than 2dB over channel estimation and 32QAM modulation used. Higher constellation size is more sensitive to increased Doppler shift.

Fig. (16) shows that the BER performance of adaptive system is much better than static system because it provides efficient spectral efficiency at any given SNR. The reason for such improvement is that when a channel encounters a deep fade, it is better to use a modulation with lower constellation size in order to get low error probability, while in good channel state it is better to transmit as many bits as possible. As a result, in order to overcome the outdated CSI ,when channel estimation is used, past and present channel symbols can be used to predict future channel symbols.
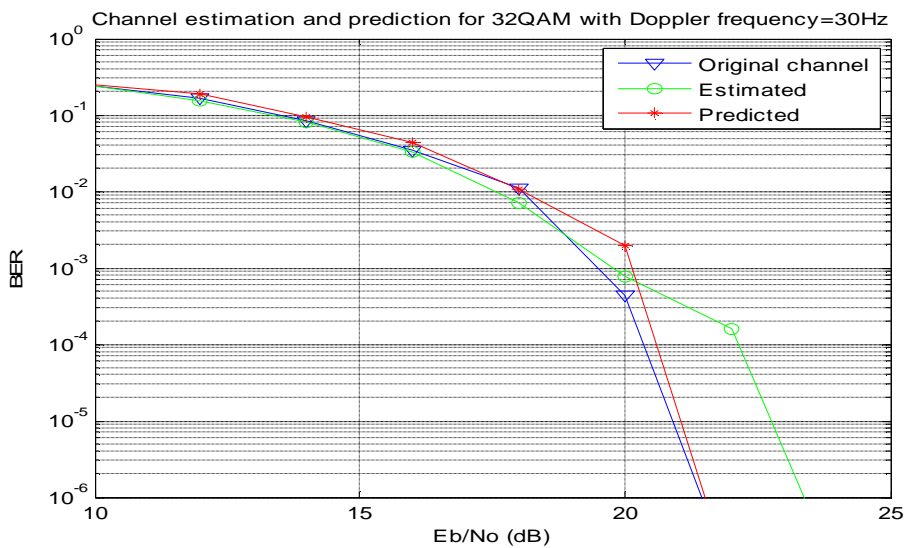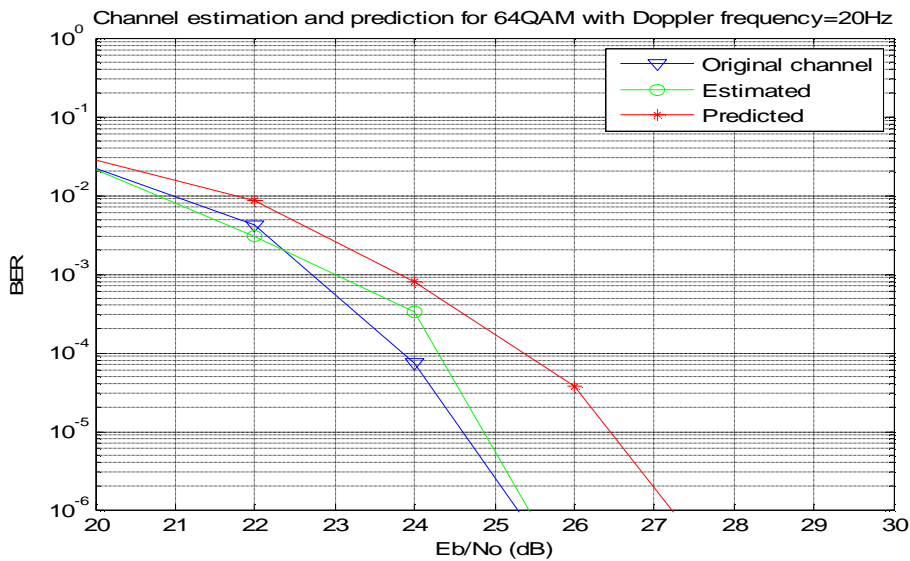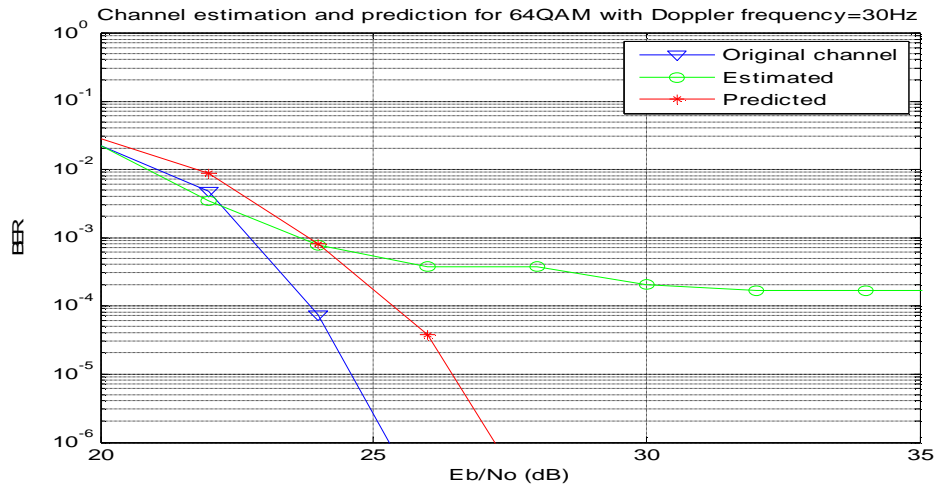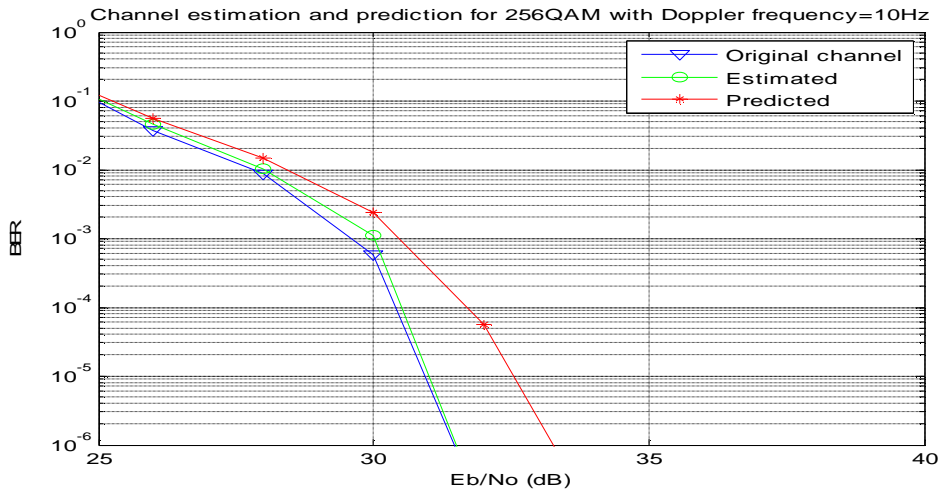

Fig. 13. Channel Estimation and Prediction 32QAM.
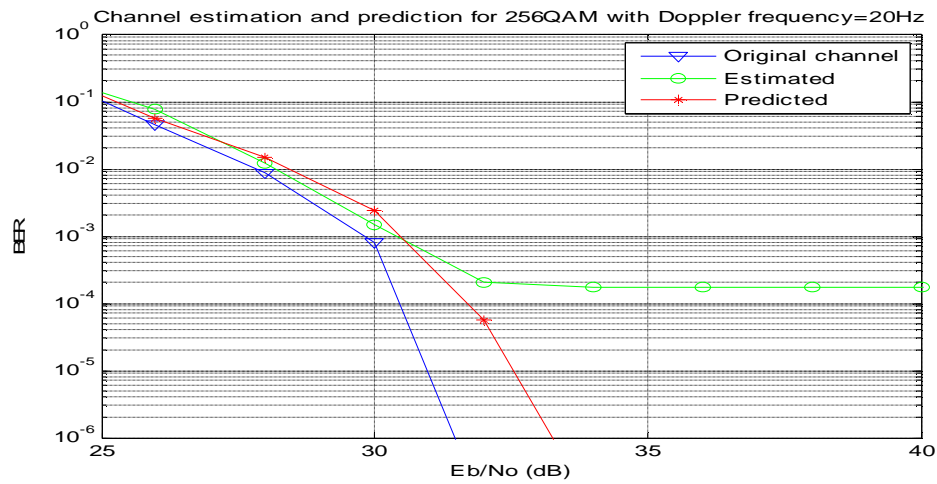

a.   Doppler Frequency=20 Hz.

b.   Doppler Frequency=30 Hz.

Fig. 14.Channel Estimation and Prediction for 64QAM.

a.   Doppler Frequency=15 Hz.

b.   Doppler Frequency=20 Hz.

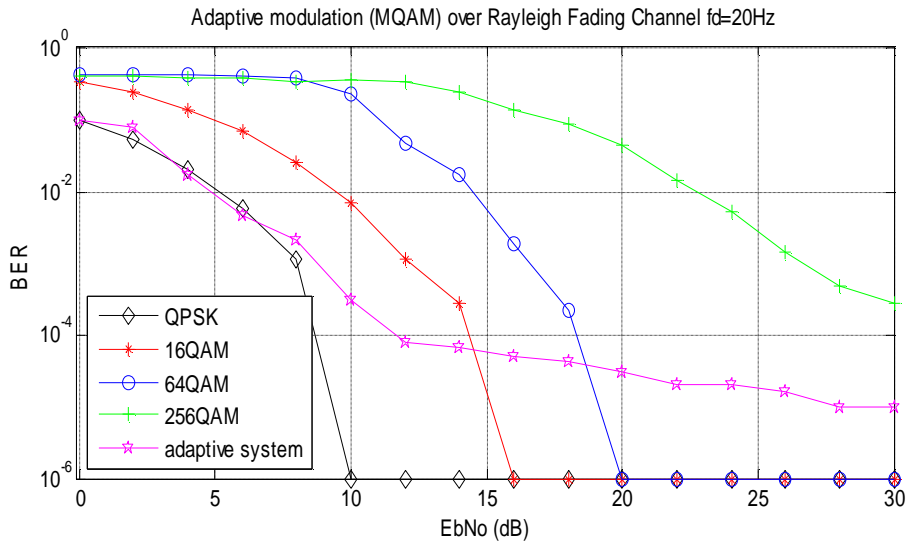**Fig. 15.Channel Estimation and Prediction 256Q AM.**

Fig. 16. BER Performance of Adaptive System.

Fig. (17) shows the spectral efficiency throughput for estimated and predicted Rayleigh fading channel taken over BER threshold 10^{-4} and Doppler frequency shift f_d =20 Hz and 40 Hz. It is clear that when the Doppler frequency increases the channel estimation alone fails to track the channel variations, and hence low spectral efficiency, while channel prediction is much more efficient with high spectral efficiency.
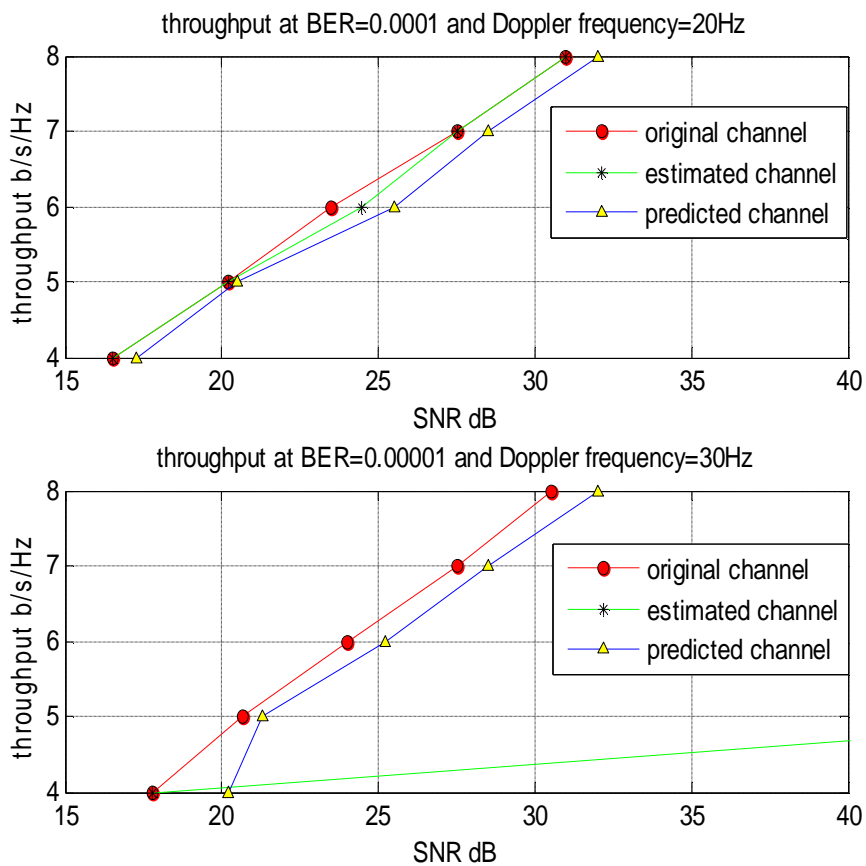

Fig. 17. Throughput of Predicted and Estimated Channel f_d=20Hz, and 30Hz BER=10^{-4} .

6. References

[1] Eric Phillip, Adaptive Techniques for Multiuser OFDM, Ph.D. Thesis in Electrical and Computer Engineering, School of Engineering, James Cook University, December/2001.

[2] Andrea Goldsmith, Wireless Communications, by Cambridge University Press, 2005.

[3] Andrea J. Goldsmith and Soon-Ghee Chua, Variable-Rate Variable-Power MQAM for Fading Channels, IEEE Transactions on Communications, volume 45, no. 10, October/1997.

[4] Sang Wu Kim, Adaptive Rate and Power DS/CDMA Communications in Fading Channels, IEEE Communications Letters, volume 3, no. 4, April/1999.

[5] Thanh Thi Ngoc Do, Improving Performance of Wireless Communication Systems Using Adaptive Space-Time Scheme, International Symposium on Electrical & Electronics Engineering, HCM City, Vietnam, October/24-25/2007.

[6] Siavash M. Alamouti, A Simple Transmit Diversity Technique for Wireless Communications, IEEE Journal on Select Areas in Communications, volume 16, no. 8, October/1998.

[7] A.O. Kadhim " Channel Estimation and Prediction based adaptive communication" Msc. Thesis, information Eng. Al-Nahrain University 2010

[8] T. S. Rappaport, Wireless Communications: Principles and Practice, 2nd edition, by Prentice Hall, 2002.

[9] Alexandra Duel-Hallen, Shengquan Hu, Hans Hallen, Long Range Prediction of Fading Signals: Enabling Adaptive Transmission for Mobile Radio Channels, IEEE Signal Processing Magazine, May/2000.

[10] Shengquan Hu, Alexandra Duel-Hallen, Hans Hallen, Adaptive Modulation Using Long Range Prediction for Flat Rayleigh Fading Channels, in Proc. 2000 IEEE Int. Symp. Inform. Theory, Sorrento, Italy, p. 159, June/2000.

[11] P. P. Vaidyanathan, The Theory of Linear Prediction, by Morgan & Claypool, 2008.

[12] Mathieu Lagrange, Sylvain Marchand, Martin Raspaud, and Jean-Bernard Rault, Enhanced Partial Tracking Using Linear Prediction, Proc. of the 6th Inernational Conference on Digital Audio Effects (DAFx-03), London, UK, September/8-11/2003.

[13] Tung-Sheng Yang, Performance Analysis of Adaptive Transmission Aided by Long Range Channel Prediction for Realistic Single- and Multi-Carrier Mobile Radio Channels, Ph.D. Thesis in Electrical Engineering, North Carolina State University, 2004.

[14] M. H. Hayes, Statistical Digital Signal Processing and Modeling, by John Wiley & Sons, 1996.

تخمين ألقناة لأغراض ألأتصالات أللاسلكية ألمتكيفة

**خليفة عبود سالم *			محمد أحمد المشهداني****

*قسم هندسة المعلومات والأتصالات/ كلية الهندسة الخوارزمي/ جامعة بغداد

**قسم هندسة المعلومات والأتصالات/ كلية تكنولوجيا المعلومات/ جامعة النهرين

الخلاصة

يعتبر التضمين المتكيف احد التقنيات الكفوءة لتحقيق التوازن بين سعة القناة ومقدار نسبة الخطأ الحاصلة في ارسال البيانات. لغرض تغيير سرعة ارسال البيانات فأنه يتطلب معرفة حالة القناة عند جهة الارسال.ان المنظومة المقترحة تتضمن ارسال رموز معروفة لتخمين حالة القناة من خلالها. وجد ان اداء المنظومة يكون جيدا في الحالات التي يكون فيها تردد دوبلر قليل، ولكن عند زيادة تردد دوبلر(30Hz>) فان تخمين القناة لا يعطي نتائج جيدة بسبب ان التخمين لا يستطيع ملاحقة التغييرات المتسارعة للقناة والتي تحدث بسبب معاملات الاضمحلال. لذلك تم اللجوء الى التنبؤ بحالة القناة لفترة قادمة من خلال التنبؤ الخطي ووجد بأنه يعطي تحسين مقداره اكبر من ٢ ديسيبل مقارنة بحالة التخمين ونسبة الخطأ المستهدفة = 10^{-4} عند استخدام 32QAM.

Effect of Journal Misalignment on the Static Characteristics of Porous Journal Bearings Lubricated with Couple Stress Fluid

Lekaa' H. Abd Al-shaheed

Department of Mechanical Engineering /Babylon University
Email: lekaa_hameed@yahoo.com

Abstract

In this paper, a theoretical study to the effect of journal misalignment on the static characteristics of oil filled porous journal bearing when lubricated with couple stress fluid has been carried out.

The analytical model used through this work is for a bearing with isotropic permeability. Considering isotropic permeability the Reynolds' equation for the oil film is modified to include a so – called filter term and the effect of fluid coupled stress. The pressure equation for the porous medium is obtained from Darcy's law and continuity equation. The equation which was used to evaluate the oil film thickness was modified to include the effect of possible misalignment in longitudinal and transverse directions. The governing equations with appropriate boundary conditions are numerically solved using a suitable numerical technique. A computer program has been prepared to solve the governing equations. The validity of the program has been tested by comparing the results obtained through this work with that published in available works. The comparison shows a good agreement between the results obtained through this work and that published by other workers.

By comparing the behavior of aligned and misaligned bearing it was found that the journal center misalignment has a considerable effect on the performance parameters of the bearing which can not be neglected.

Key words: Static Characteristics, Self Lubricated Bearing, Misaligned Bearing, Uniform Permeability, Coupled Stress.

1. Introduction

In most theoretical investigations of hydrodynamic lubrication it has been assumed that the journal and the bearing axis are aligned. This is an unrealistic assumption for the bearing operating with small film thickness since the bearings often operate in misaligned condition. Bearing misalignment can vary in magnitude and direction. The most important cases to be considered are vertical , twisting , and horizontal misalignment or combination of these can also occur.

Most investigators in this area confined their work to solid bearing. A little work has been found related to the behaviour of aligned porous bearing lubricated with coupled stress fluid, while most works found related to study the behaviour of porous bearing lubricated with Newtonian – lubricant as can be seen in references [1 – 8]. It

was found that the Newtonian fluid constitutive approximation is not satisfactory engineering approach to many lubrication problems. Hence the effects of non – Newtonian behaviour must be taken into account in the realistic study of these bearings. Many micro continuum theories have been developed to describe the behaviour of non – Newtonian fluids. Airman et. al. [9,10] developed a micro continuum theory to describe the behaviour of fluids containing structure such as polymer. Naduvinamani et. al. [11] used the couple stress theory to analyze the squeeze film lubrication of a short porous bearing. A main conclusion through this work is that under cyclic load the couple stress fluid provide a reduction in journal velocity and an increase in minimum permissible height of squeeze. The surface roughness effect in a short porous journal bearing lubricated with a couple stress fluid was studied by Naduvinamani et. al. [12]. It was

observed during this work that the effect of surface roughness on the bearing characteristics are more pronounced for couple stress fluids as compared with Newtonian fluids. Using the couple stress theory to investigate the lubrication mechanism of synovial joints was carried out by Bujurke and Ramesh [13]. They showed that the effects of surface roughness are considerably prounced for poroelastic bearings with couple stress fluid as lubricant compared to classical case.

Recently the flow and heat transfer of couple stress fluid in a porous channel with expanding and contracting walls have been investigated by Srinivasacharya and Srinivasecharyulu [14]. Graphs for velocity components and temperature distribution are presented for different values of the fluid and geometric parameters. Naduvinamani and Patil [15] used a numerical solution to the finite modified Reynolds' equation for couple stress squeeze film lubrication of porous journal bearing. They concluded that under

a cyclic load, the effect of couple stress is to reduce the velocity of the journal center and to increase the minimum permissible height of the squeeze film.

So far it seems that all the above researches ignore the effect of journal center misalignment. The effect of bearing misalignment on the bearing characteristics such as the mean load carrying capacity, mean frictional force, and the other bearing characteristics are investigated during this work.

2. Numerical analysis

2.1. Model of the misaligned porous journal bearing

The model of misaligned porous journal bearing lubricated with couple stress fluid shown in Figure (1) is adopted through the present work.
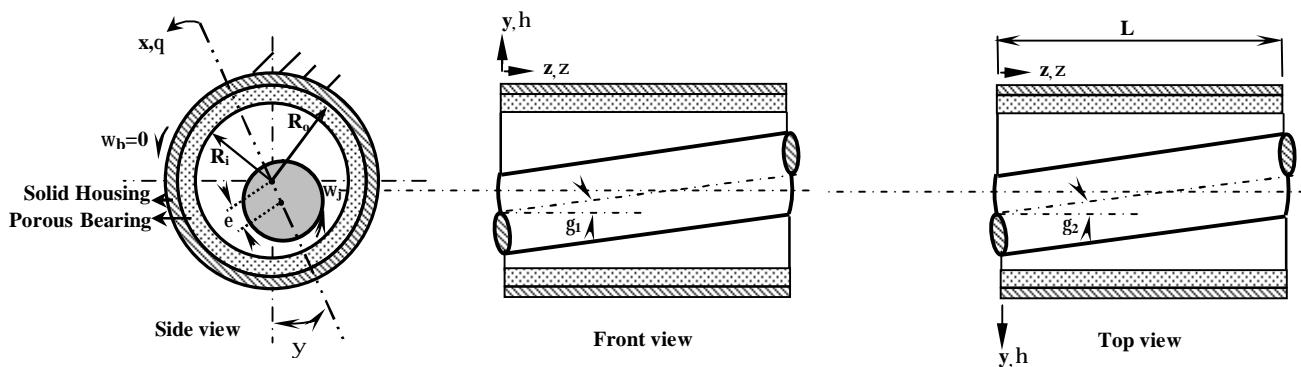

Fig. 1. Geometrical Configuration of the Misaligned Porous Journal Bearing.

2.2. Governing Equations

The governing equation for the pressure distribution in the oil – film is given by the modified Reynolds' equation including a so – called filter term and coupled stress effect. For a journal bearing lubricated with coupled stress fluid with a constant viscosity the modified Reynolds' equation can be written as [12]:-

$$\frac{\partial}{\partial x}\left\{\left[g(h,t)+\frac{12kd}{(1-b)}\right]\frac{\partial P}{\partial x}\right\}+\frac{\partial}{\partial z}\left\{\left[g(h,t)+\frac{12kd}{(1-b)}\right]\frac{\partial P}{\partial z}\right\}$$
$$=6mU\frac{\partial h}{\partial x} \qquad \ldots(1)$$

Where:
$$t=\sqrt{m/h}$$

Equation (1) can be written in dimensionless form as follows:-

$$\frac{\partial}{\partial q}\left\{\left[g^{\wedge}(h^{\wedge},l_c^{\wedge})+\frac{12j}{(1-b)}\right]\frac{\partial P^{\wedge}}{\partial x}\right\}+$$
$$\frac{1}{4a^2}\frac{\partial}{\partial z^{\wedge}}\left\{\left[g^{\wedge}(h^{\wedge},l_c^{\wedge})+\frac{12j}{(1-b)}\right]\frac{\partial P^{\wedge}}{\partial z^{\wedge}}\right\}=6\frac{\partial h^{\wedge}}{\partial q} \qquad \ldots(2)$$

Where: [15]

$$g^{\wedge}(h^{\wedge},l_c^{\wedge})=h^{\wedge^3}-12l_c^{\wedge^2}h^{\wedge}+24l_c^{\wedge^3}\tanh\left(\frac{h^{\wedge}}{2l_c^{\wedge}}\right) \ldots(3)$$

$$b=\left(\frac{h}{m}\right)\Big/k \qquad \ldots(4)$$

Where β represents the ratio of microstructure size to the porous size. For a vary small β, i.e. β<<1, the polar additives percolate into the porous matrix. It in clear that when β→0, the flow become Newtonian flow.

It can be shown that the couple stress parameter (l_c) has a units of length and it may be regarded as chain length of polar additives and can be evaluated as [15,16]:

$$l_c = \sqrt{h/m} \qquad \ldots(5)$$

The fluid film thickness in cooperating the effect of journal misalignment in both directions (axial and twisting) can be expressed in non–dimensional form as follows [17]:-

$$h^\wedge = 1 + e\cos q - zs_1\cos q + zs_2\sin q \qquad \ldots(6)$$

Where:

$$s_1 = 2\left(\frac{R_i}{C}\right)\left(\frac{L}{D}\right)\tan g_1 \qquad \ldots(7)$$

$$s_2 = 2\left(\frac{R_i}{C}\right)\left(\frac{L}{D}\right)\tan g_2 \qquad \ldots(8)$$

The two independent misalignment angles (γ_1 and γ_2) are measured from ξ=0; it is clear from equation (6) that the oil gap geometry depends on (θ and ξ).

Due to the continuity of the fluid motion at the porous matrix, the oil pressure inside the porous matrix satisfies the Laplace equation which can be expressed as [12, 15]

$$\frac{\partial^2 P^*}{\partial x^2} + \frac{\partial^2 P^*}{\partial y^2} + \frac{\partial^2 P^*}{\partial z^2} = 0.0 \qquad \ldots(9)$$

The classical Reynolds' boundary conditions are adopted through this work. The Reynolds' conditions can be expressed as [1,18];

$$\left.\begin{array}{l} P^\wedge(q,0) = P^\wedge(q,1) = P^{\wedge*}(r^\wedge,q,0) = P^{\wedge*}(r^\wedge,q,1) = 0 \\[4pt] P^\wedge(0,z) = P^{\wedge*}(r^\wedge,0,Z) = 0 \\[4pt] P^\wedge(q,Z) = P^{\wedge*}(r^\wedge,q,Z)\,at(r^\wedge) = 1 \\[4pt] P^{\wedge*}(r_o^\wedge,q,1/2) = P_s^\wedge \\[4pt] \hat{P} = \dfrac{\partial \hat{P}}{\partial q} = 0\,at\,q = p + a_c \end{array}\right\} \qquad \ldots(10)$$

Where a_c is the angle at which cavitations starts.

2.3. Bearing Parameters

After evaluating the pressure field through the oil film, the bearing performance parameters can be calculated as follows:-

The radial and tangential components of the load are found as :

$$\left.\begin{array}{l} \left(\hat{W}_R\right) = -\int_0^1 \int_{0_1}^{p+a_c} \left(P^\wedge(q,x)\cos q\right) dqdx \\[10pt] \left(\hat{W}_T\right) = \int_0^1 \int_0^{p+a_c} \left(P^\wedge(q,x)\sin q\right) dqdx \end{array}\right\} \qquad \ldots(11)$$

The total bearing load carrying capacity can be expressed in dimensionless form as;

$$\left(\hat{W}\right) = \sqrt{\left(\hat{W}_R\right)^2 + \left(\hat{W}_T\right)^2} \qquad \ldots(12)$$

The attitude angle can be found as:-

$$(\Psi) = \tan^{-1}\left(W_T^\wedge / W_R^\wedge\right) \qquad \ldots(13)$$

The friction force can be expressed in dimensionless form as [16] ;

$$F_h^\wedge = \int_0^1 \int_0^{p+a_c} \left(\frac{1}{h^\wedge} + \frac{h^\wedge}{2}\frac{\partial P^\wedge}{\partial q}\right) dq dz^\wedge \qquad \ldots(14)$$

The coefficient of friction can be evaluated as:

$$f(R/C) = \frac{F_h^\wedge}{W^\wedge} \qquad \ldots(15)$$

The oil side leakage flow for the porous journal bearing can be evaluated as [16];

$$Q_s^\wedge = \int_0^1 \int_0^{p+a_c} \frac{\partial P^\wedge}{\partial z^\wedge}\bigg|_{z^\wedge=1} h^\wedge *$$
$$\left\{y^{\wedge 2}h^{\wedge 2} - y^\wedge h^{\wedge 2} + 2l_c^{\wedge 2}\left[1 - \frac{\cosh\left(\dfrac{2y^\wedge h^\wedge - h^\wedge}{2l_c^\wedge}\right)}{\cosh\left(\dfrac{h^\wedge}{2l_c^\wedge}\right)}\right]\right\} dqdy^\wedge$$
$$\ldots(16)$$

2.4. Method of solution

The pressure distribution in the oil film can be obtained by solving the modified Reynolds' equation (1), the Laplace equation (9) coupled with the modified oil film thickness equation (6) with the Reynolds' boundary conditions equation

(10) simultaneously using iterative numerical scheme. The field of solution is divided into grid spacing ($N_1=8$, $N_2=180$, $N_3=12$); each has a mesh size $\Delta r^\wedge * \Delta\theta * \Delta z^\wedge$ for porous matrix and grid spacing ($N_2=180$, $N_3=12$); each has a mesh size $\Delta\theta * \Delta z^\wedge$ for oil film thickness.

Gauss Siedel iterative scheme with successive under relaxation has been used to solve the governing equation of the problem. The iterations are stooped when the following convergence criteria are satisfied.

For the oil pressure inside the porous matrix the convergence criterion can be expressed as:-

$$\left(\frac{\sum\sum\sum \left| P_{i,j,k}^{\wedge *(n+1)} - P_{i,j,k}^{\wedge *(n)} \right|}{\sum\sum\sum \left| P_{i,j,k}^{\wedge *(n)} \right|} < 10^{-5} \right) \qquad \dots(17)$$

While for the oil pressure in the bearing oil film the convergence criterion can be expressed as:-

$$\left(\frac{\sum\sum \left| P_{j,k}^{\wedge(n+1)} - P_{j,k}^{\wedge(n)} \right|}{\sum\sum \left| P_{j,k}^{\wedge(n)} \right|} < 10^{-5} \right) \qquad \dots(18)$$

A computer program written in FPRTRAN – 90 language has been used to solve the governing equations of the problem. Figure (2) shows the flow chart of the computer program used during this work.
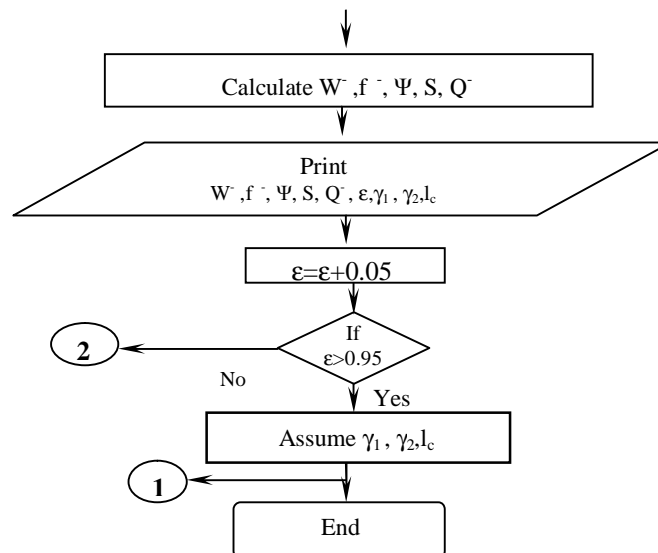

Will be continue

Calculate $\bar{W}$,$\bar{f}$, Ψ, S, $\bar{Q}$

Print
$\bar{W}$,$\bar{f}$, Ψ, S, $\bar{Q}$, ε,γ_1 , γ_2,l_c

$\varepsilon=\varepsilon+0.05$

If
$\varepsilon>0.95$

2

No

Yes

Assume γ_1 , γ_2,l_c

1

End
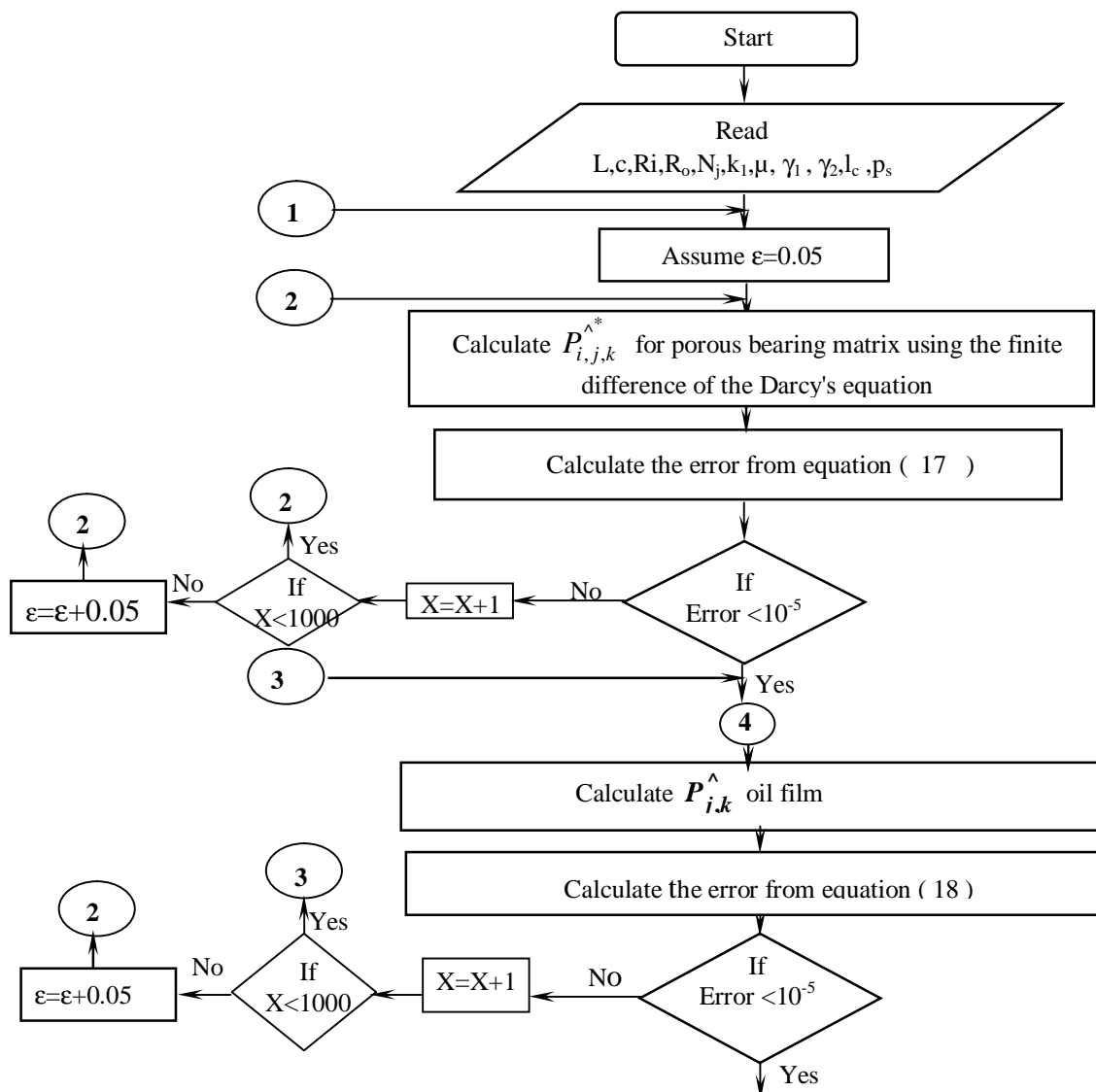
Fig. 2.Flow Chart of the Computer Program.

3. Results and discussion

The combined effect of couple stress and journal center misalignment on the performance of porous journal bearing is predicted through this work. The effect of couple stress is taken into consideration on the basis of stokes couple stress fluid model for lubricant. A finite porous journal bearing operated under steady conditions is analyzed. All bearing characteristics such as the load carrying capacity (W), frictional coefficient f(R/C) , friction force, the lubricant side leakage and the attitude angle are functions of the couple stress parameter (l_c) and the eccentricity ratio (ε).

The computer program prepared to solve the governing equations of the present work is verified by comparing the obtained results with those obtained by Mokhiamer (1999). Figures (1) and (2) shows a comparison between the pressure distribution obtained in this work with that obtained by Mokhiamer (1999) for eccentricity ratio of (0.4, 0.6) respectively. It can be shown from these figures that the maximum percentage of error between the obtained and the published results is (6.25% and 5%) respectively, while Figure (3) shows that the maximum error between the attitude angle obtained during this work in comparison with that obtained by Mokhiamer (1999) did not exceed (6%). The percentages of error mentioned above are based on the difference between the calculated and published data divided by the published data. It is clear from the above figures' that the results obtained through this work are in a good agreement with the published results and give a reasonable reliability to the program used to analyze the problem of the present work.

Figure (4) shows that the load carrying capacity of the bearing decreases when combined misalignment (axial and twisting) which gives an indication that the oil film thickness increases when the bearing suffers from the combined misalignment is taken into consideration. A maximum decrease of (28%) in load carrying capacity is noticed in this case. A greater decreases in load carrying capacity is noticed when axial misalignment of the bearing is taken into consideration especially for low values of eccentricity ratio. The maximum reduction is calculated and found to be about (35%) , which indicates an increase in oil film thickness in this range of eccentricity ratios. A slight increase in load carrying capacity is noticed when the twisting misalignment is considered especially for low values of eccentricity ratio (i.e. to about $\varepsilon = 0.4$) while it has no effect for higher values of eccentricity ratio.

A decrease in attitude angle is seen when combined axial and twisting misalignment is taken into consideration as shown in Figure (5). A maximum decrease is calculated and found to be (20%). This can be attributed to the variation in load carrying capacity components mentioned before. An increase in attitude angle is noticed when axial misalignment of the bearing is taken into consideration. This is due to the increase in oil film thickness in this case.

A slight decrease in coefficient of friction is shown when the twisting misalignment is considered as shown in Figure (6) , which indicates a lower shearing rate of the oil in this case. An increase in coefficient of friction is shown when twisting and combined misalignment

is taken into consideration. This is due to the increase of the shearing rate of the lubricant in this case.

Figure (7) shows that the side leakage flow rate of the bearing deceases when the axial misalignment of the journal bearing is taken into consideration. This can be attributed to the increase in oil film thickness, which affects the velocity component in axial direction, and the pressure gradient in circumferential direction. A decrease in side leakage flow rate of (20%), is noticed in this case. An increase in side leakage flow rate has been shown when axial and twisting misalignment of the journal bearing have been taken into consideration. A higher increase in side leakage is noticed when the twisting misalignment only is taken into consideration which indicate the increase in oil film thickness of the lubricant.

Figure (8) shows that the load carrying capacity for a porous bearing lubricated with couple stress fluid is higher than that obtained when the bearing lubricated with Newtonian lubricant for different values of the eccentricity ratios. This can be attributed to the higher viscosity of the couple stress lubricant than that of Newtonian lubricant. It is clear from this figure that a higher enhancement is obtained when the bearing is lubricated with couple stress lubricant of higher couple stress parameter (l_c). About (40%) enhancement in load carrying capacity is shown for the bearing lubricated with a lubricant of couple stress parameter of ($l_c = 0.2$).

The bearing attitude angle is seen to have lower values for the bearing lubricated with couple stress lubricant than that lubricated with Newtonian lubricant as shown in Figure (9). This

is attributed to the increase in load carrying capacity component mentioned above when lubricating the bearing with couple stress fluid. The decrease in attitude angle becomes higher when the bearing lubricated with couple stress lubricant of higher couple stress parameter.

A decrease in friction coefficient of the bearing has is when the bearing lubricated with couple stress lubricant rather than that lubricated with Newtonian lubricant as shown in Figure (10). The decrease in coefficient of friction become higher when the bearing lubricated with a couple stress lubricant with higher couple stress parameter. This can be explained if we know that the load carrying capacity of the bearing is increased in this case, since the coefficient of friction is inversely proportional to the value of the load.

Figure (11) shows a slight increase in oil side leakage from the bearing lubricated with couple stress lubricant than that for lubricated with Newtonian lubricant. A couple stress parameter (l_c) is shown to have a slight effect on the oil side leakage of the bearing. A slight increase in oil side leakage is shown with increasing values of (l_c). The increase oil side leakage can also be attributed to the effect of combined misalignment of the bearing which causes larger oil film thickness.

The effect of length to diameter ratio of the bearing on the load carrying of the bearing is shown in Figure (12). It is clear that the load carrying capacity increase for the bearing with higher length to diameter ratio, while the coefficient of friction decreases as shown in Figure (13).
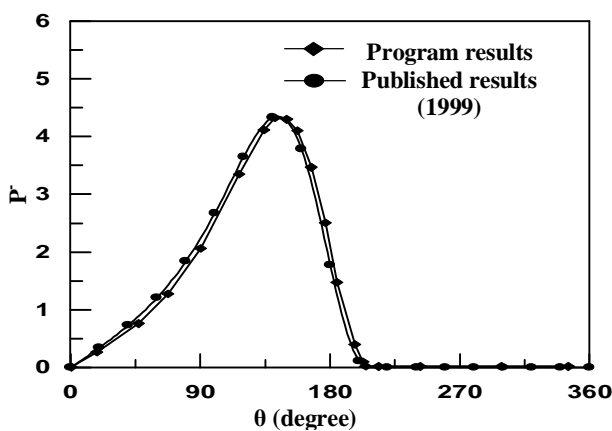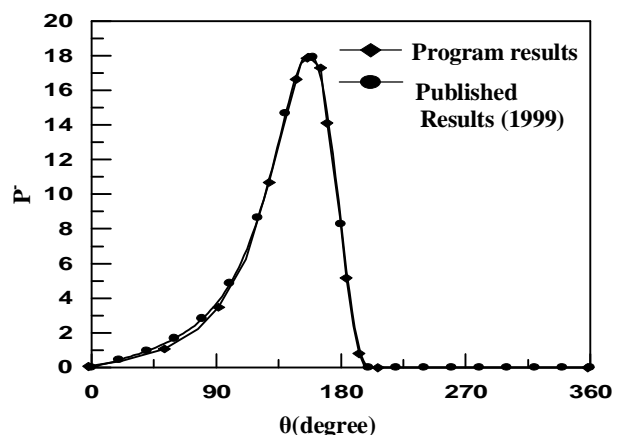

Fig. 1. Comparison Pressure Distribution Between Present and Published Result U.M.Mokhiamer et. al. (1999) at P_s= 0.1, l_c^-=0.4,R/L=0.5 ,g_1=0.0 , g_2=0.0 and e=0.4.

Fig. 2. Comparison Pressure Distribution Between Present and Published Result U.M.Mokhiamer et. al. (1999) at P_s= 0.1, l_c^-=0.4,R/L=0.5 ,g_1=0.0 , g_2=0.0 and e=0.6.
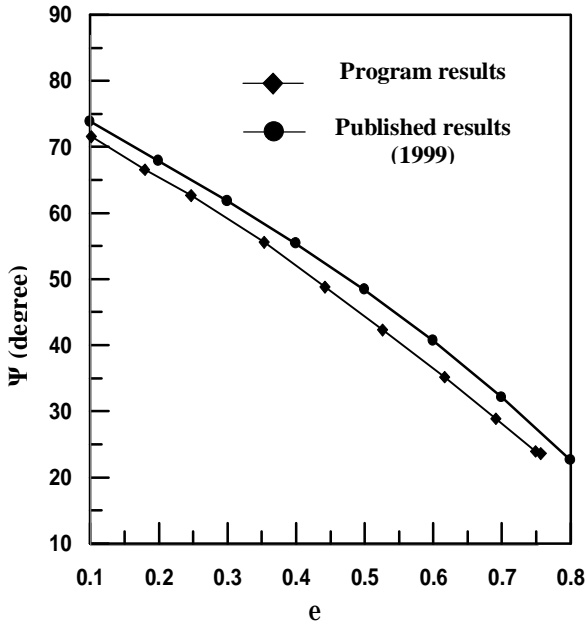
Fig. 3. Comparison attitude angle versus eccentricity ratio between present and published result U.M.Mokhiamer et. al. (1999) at P_s = 0.1, l_c^- =0.4,R/L=0.5 ,g_1=0.0 , g_2=0.0 and e=0.4.
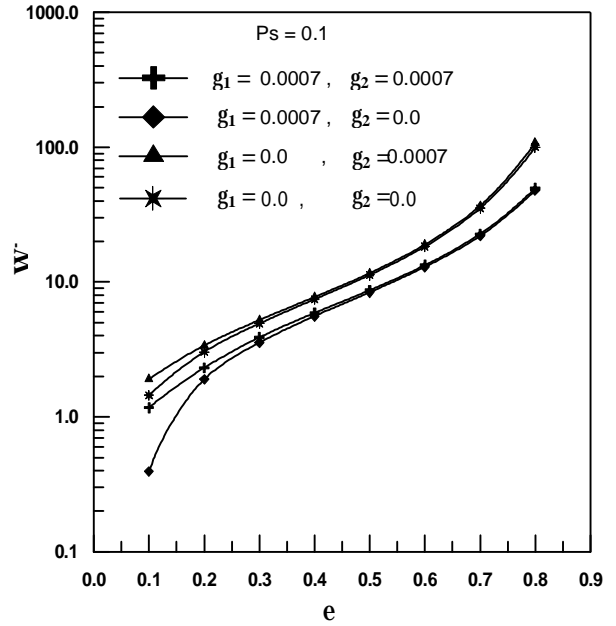

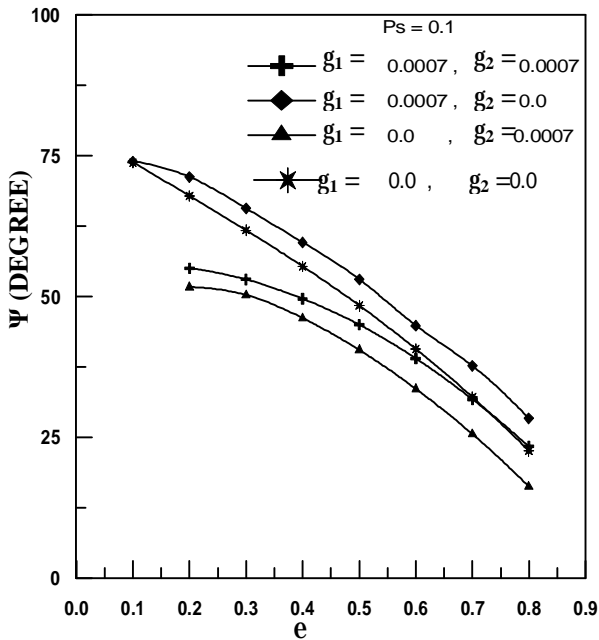**Fig. 4. Load carrying capacity verse eccentricity ratio for different misalignment ratios at l_c^- = 0.4.**

Fig. 5. Attitude angle verse eccentricity ratio for different misalignment ratios at l_c^- = 0.4.
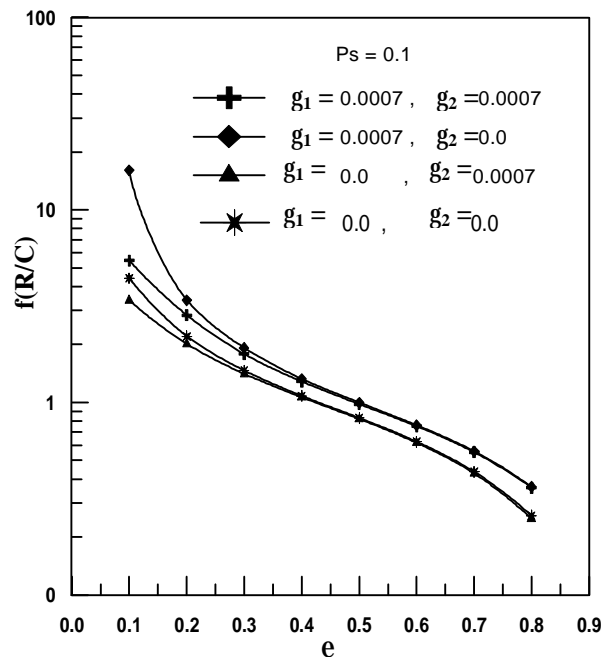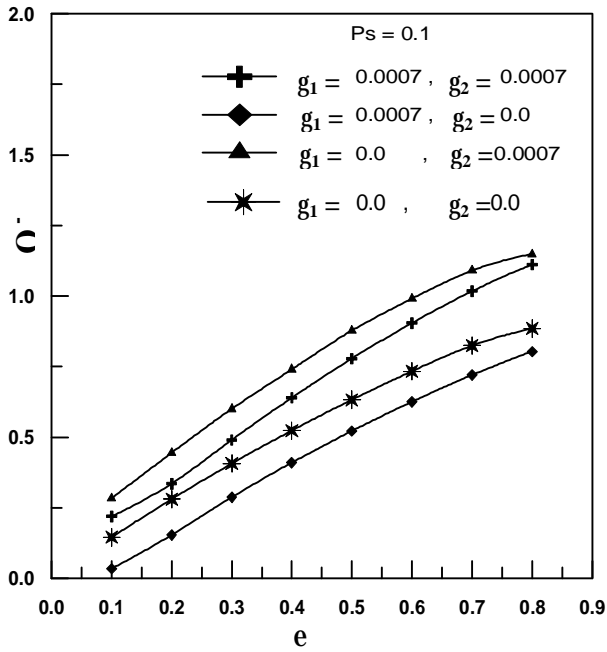

Fig. 6. Coefficient of friction verse eccentricity ratio for different misalignment ratios at l_c^- = 0.4.

Fig. 7. Dimensionless Side Flow Verse Eccentricity Ratio for Different Misalignment Ratios at $l_c^- = 0.4$.
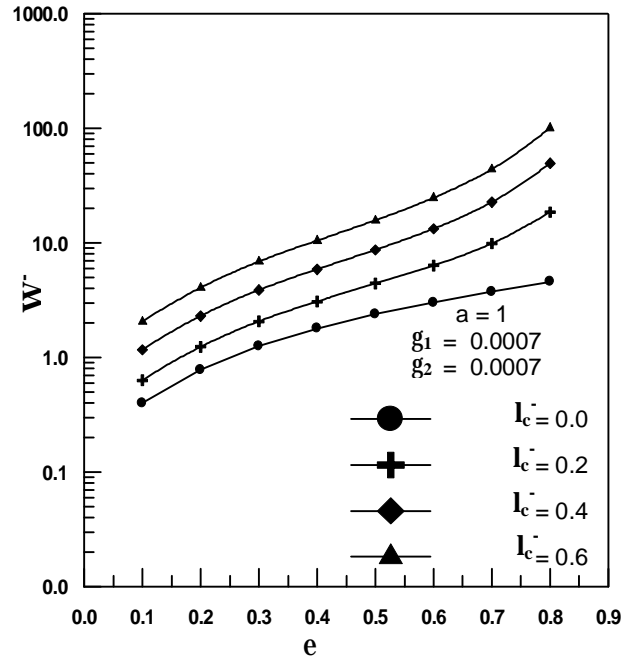

Fig. 8. Load Carrying Capacity Verse Eccentricity Ratio for Various Values of Couple Stress parameter.
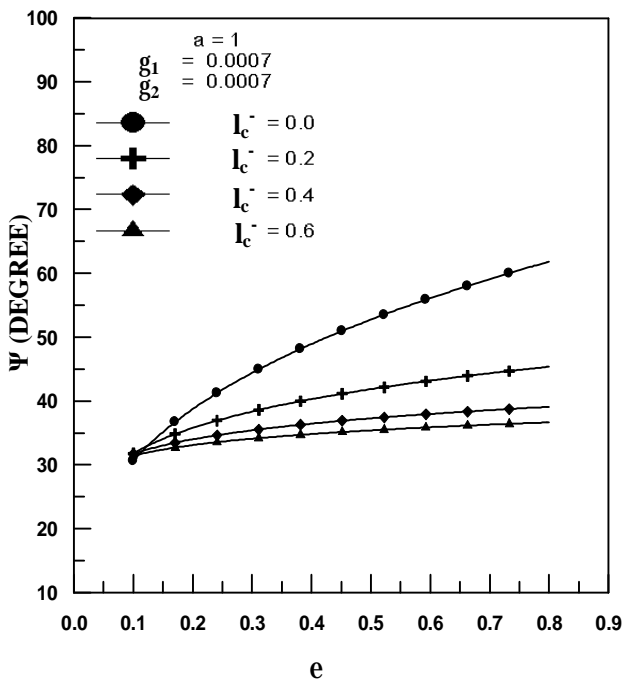

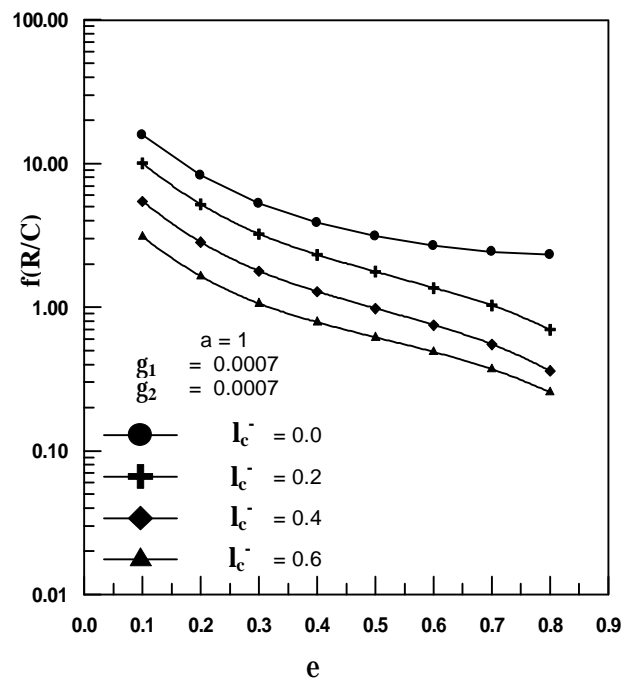**Fig. 9. Attitude Angle Verse Eccentricity Ratio for Various Values of Couple Stress Parameter.**

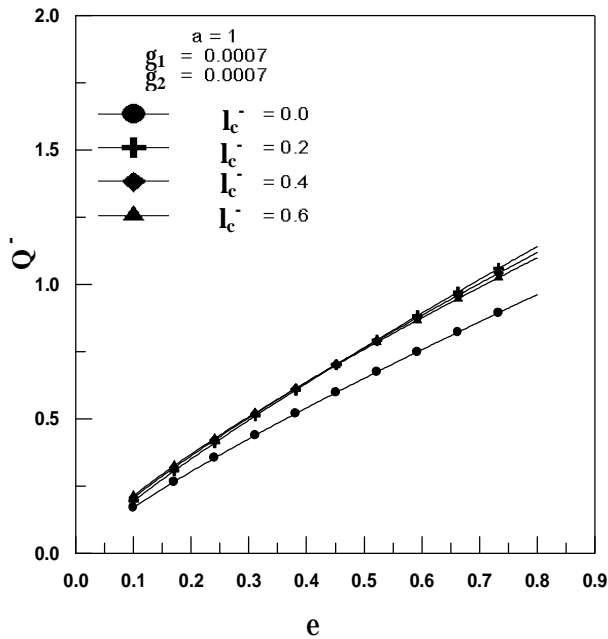**Fig. 10. Coefficient of Friction Verse Eccentricity Ratio for Various Values of Couple Stress Parameter.**

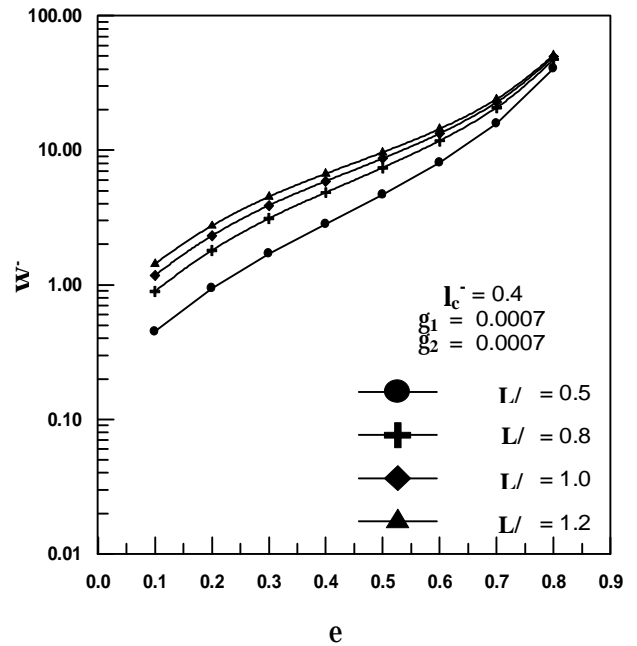**Fig. 11. Dimensionless Side Flow Verse Eccentricity Ratio for Various Values of Couple Stress Parameter.**

Fig. 12. Load Carrying Capacity Verse Eccentricity Ratio for Various Values of L/D Ratios.
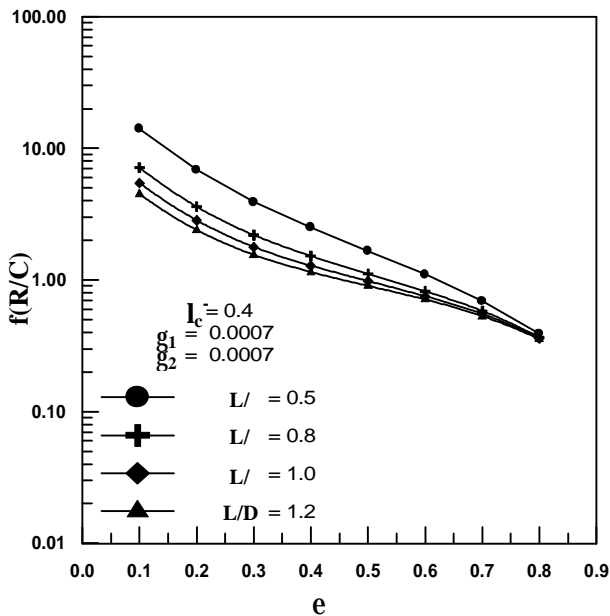

Fig. 13. Friction Factor Verse Eccentricity Ratio for Various Values of L/D Ratios.

4. Conclusions

On the basis of microcontinum theory developed by Stokes, the present investigation reveals the effect of couple stresses on the performance of misaligned finite length porous

journal bearing. The results obtained through this work leads to the following main conclusions:-

1- The journal center misalignment has a considerable effect on the performance parameters of the bearing which can not be neglected. The presence of combined misaligned (axial and twisting) causes a decreases of the load carrying capacity and attitude angle.

2- The presence of bearing axial misalignment causes a slight increase in load carrying capacity and attitude angle, while a decrease in side leakage of the bearing, is noticed in this case.

3- Using the coupled stress fluid as a lubricant seems to improve some of the steady state characteristics of the porous bearings in comparison with the bearing lubricated with Newtonian lubricant. An increase in load carrying capacity, a decrease in attitude angle, friction coefficient and slight increase in side leakage flow have been noticed.

5. Nomenclature

The following symbols are used throughout this work.

a	ratio of length to diameter
c	Journal Bearing Clearance (m)
D	diameter of bearing (m)
F	friction force (N)
$F^{\wedge}$	Dimensionless friction force , $F^{\wedge} = (Fc/\mu\omega_j r^2 L)$
$f^{\wedge}$	Dimensionless Friction Coefficient, $f^{\wedge} = (R/c)f$
$h^{\wedge}$	Dimensionless Film Thickness, ($h^{\wedge} = h/c$)
L	Length of the Bearing (m)
L_c	characteristics length of the additive
$L_c^{\wedge}$	dimensionless coupled stress parameter , $L_c^{\wedge} = L_c/c$
k	Permeability parameter (m^2)
N_j	Journal Rotational Speed (r.p.m)
$P^{\wedge}$	Dimensionless Oil-Film Pressure, $P^{\wedge} = c^2 P/(r^2 \mu\omega_j)$
$P^{\wedge*}$	Dimensionless Oil – Film Pressure Inside the Porous Matrix, $P^{\wedge*} = c^2 P^*/(r^2\mu\omega_j)$
P_s	Supply Pressure (N/m^2)
$Q^{\wedge}_s$	Dimensionless side leakage flow, $Q^{\wedge}_s = Q_s L/U_j R^2 c$
$r^{\wedge}$	Normalized radial coordinate, $r^{\wedge} = r/r_i$
R_j	inner radius of porous bearing (m)
R_o	outer radius of porous bearing (m)
r_i	Inner Radius (m)
r_o	Outer Radius (m)
S	Sommerfeld Number , $S = (R\mu\omega_j L / W)*(r_i / c)^2$
U_j	Journal Velocity (m/s)
$W^{\wedge}$	Dimensionless Load Carrying Capacity, $W^{\wedge} = (W c^2 / \eta\omega_j\, r_i^3\, L)$
$W^{\wedge}_r$	Dimensionless Component of Oil Film Force Along the Line of Centers
$W^{\wedge}_T$	Dimensionless Component of Oil Film Force Perpendicular to the Line of Centers
$y^{\wedge}$	Dimensionless bearing coordinates in axial direction, $y^{\wedge} = y/h$
$Z^{\wedge}$	non – dimensional axial co- ordinate $Z^{\wedge} = z/L$

Greek Symbols

ε	Eccentricity Ratio
μ	Absolute Viscosity of lubricant (pa . s)
η	material constant responsible for the couple stress parameter
θ	Angular Coordinate from Maximum Film Thickness Position (Degree)
ρ	Density of oil (kg/m^3)
δ	porous layer thickness (m)
Φ	Permeability parameter , $\Phi = k*\delta/c^3$
ψ	Attitude Angle (degrees)
r, θ, z	Bearing coordinates in radial, circumferential and axial directions.
γ_1, γ_2	tilt angles (rad)
σ_1, σ_2	two independent misalignment parameters
ξ	Normalized axial coordinate (z/L)
ω_j	journal rotational speed (rad/sec)

Subscript

b	Referring to Bearing
j	Referring to Journal

Superscript

^	Dimensionless Quantity
•	Porous Parameter

6. References

[1] C. Cusano, , 1979, "An analytical Study of Starved Porous Bearings", Transactions of the ASME, January, vol. 101, pp. 38 – 47.

[2] S. Kaneko, , 1989, "static and dynamic characteristics of porous journal bearings with Anisotropic permeability" JSME International journal, series III, vol. 32, no. 1, 1989.

[3] S. Kaneko, and S. Obara, , 1990, "Experimental Investigation of Mechanism of Lubrication in Porous Journal Bearings: Part 1- Observation of Oil Flow in Porous Matrix", Transaction of ASME, October, vol. 112, pp. 618 – 623.

[4] N. M. Bujurke and H. P. Patil, , 1991, "An analysis of squeeze film action in porous layered bearings", Wear, 145, pp. 385 – 397.

[5] Kaneko, S., Ohkawa, Y., Hashimoto, Y., 1994, "A Study of Mechanism of Lubrication in Porous Journal Bearings: Effect of Dimensionless Oil –Feed Pressure on Static Characteristics Under Hydrodynamic Lubrication Conditions",

Transactions of the ASME, July, vol. 116, pp. 606 – 611.

[6] S. Kaneko, and Y. Hashimoto, 1995, "A Study of the Mechanism of Lubrication in Porous Journal Bearings: Effect of Dimensionless Oil – Feed Pressure on Frictional Characteristics", Journal of Tribology, April, vol. 117, pp. 291 – 296.

[7] S. Kaneko, Y. Hashimoto, and I. Hiroki, 1997, "Analysis of Oil – Film Pressure Distribution in Porous Journal Bearings Under Hydrodynamic Lubrication Conditions Using An Improved Boundary Condition", Journal of Tribology, January, vol. 119, pp. 171 – 178.

[8] Yasunaga Mitsuya, Zhisheng Deng, and Masahiro Ohka, 1997, "Derivation of Rarefaction – Modified Reynolds Equation Considering Porosity of Thin Lubricant Film", Journal of Tribology, October, vol. 119, pp. 653 – 659.

[9] T. Ariman, M. A. Turk, and N. D. Sylvester, 1973, "Microcontinuum Fluid Mechanics – A Review" , Int. Engng Sci., Vo. 11, pp. 905 – 930.

[10] T. Ariman, M. A. Turk, and N. D. Sylvester, 1974, "Application of microcontinuum Fluid Mechanics" Int.J. Engng Sci., Vo. 12, pp. 273.

[11] N. B. Naduvinamani. P. S. Hiremath, and G. Gurubasavaraj, 2001, "Squeeze film lubrication of a short porous journal bearing with couple stress fluids", Tribology International, 34, pp. 739 – 747.

[12] N. B. Naduvinamani. P. S. Hiremath, and G. Gurubasavaraj, 2002, "Surface roughness effects in a short porous

journal bearing with couple stress fluid", Fluid Dynamic Research, 31, pp. 333 – 354.

[13] N. M. Bujurke, and Ramesh B. Kudenatti, 2006, "An analysis of rough poroelastic bearings with reference to lubrication mechanism of synovial joints", Applies Mathematics and Computation , 178, pp. 309 – 320.

[14] D. Srinivasacharya , N. Srinivasecharyulu AND o. Odelu, 2009, "Flow and heat transfer of couple stress fluid in a porous channel with expanding and contracting walls", International Communications in heat and mass Transfer, 36, pp. 180 – 185.

[15] N. B. Naduvinamani and S. B. Patil, 2009, "Numerical solution of finite modified Reynolds equation for couple stress squeeze film lubrication of porous journal bearings", Computers and Structures, 87, pp. 1287 – 1295.

[16] U. M. Mokhiamer, W. A. Crosby and H. A. El – Gamal, 1999, "Astudy of a journal bearing lubricated by fluid with couple stress considering the elasticity of the liner", Wear, 224, pp. 194 – 201.

[17] y. Jin jang and chong – ching chang, 1987, "adiabatic solutions for a misaligned journal bearing with non – Newtonian lubricants", tribology international, vol. 20, no. 5, pp. 267 – 275

[18] Jaw – Ren Lin, 1997, "Effect of couple stresses on the lubrication of finite journal bearings", Wear, 206, pp. 171 – 178.

تأثير انحراف المحور على الخصائص الساكنة للمساند المقعدية ذاتية التزييت المشبعة بمائع ذو أجهاد مزدوج

لقاء حميد عبد الشهيد

قسم الهندسة الميكانيكية/ جامعة بابل

البريد الالكتروني:lekaa_hameed@yahoo.com

الخلاصة

يتضمن هذا البحث دراسة نظرية لتأثير أنحراف المحور على الخصائص الساكنة للمساند المقعدية ذاتية التزييت المشبعة بمائع ذو أجهاد مزدوج. الموديل التحليلي المستخدم في البحث الحالي يختص بالمساند ذات النفاذية منتظمة التوزيع. مع الأخذ بنظر الاعتبار النفاذية المنتظمة للمسند المقعدي فان معادلة رينولدز عدلت لتأخذ بنظر الاعتبار تأثير النفاذية ونوعية الزيت (الزيت مزدوج الأجهاد). معادلة الضغط للطبقة المسامية استحصلت من معادلة دارسي ومعادلة الاستمرارية. المعادلة التي استخدمت لاحتساب سمك طبقة الزيت عدلت لتأخذ بنظر الاعتبار تأثير انحراف المحور بالاتجاهين الطولي والمستعرض. تم حل المعادلات الحاكمة مع الشروط الحدية المناسبة عدديا باستخدام تقنية عددية مناسبة. تم أعداد برنامج حاسوبي لحل المعادلات الحاكمة وتم التأكد من موثوقية البرنامج عن طريق مقارنة بعض النتائج المستحصلة في هذا البحث مع تلك المنشورة في بعض البحوث المتوفرة وقد أظهرت عملية المقارنة تقاربا جيدا في النتائج المستحصلة مع تلك المنشورة. ومن خلال مقارنة تصرف المساند المنحرفة والغير منحرفة وجد بأن لانحراف محور المسند المقعدي تأثيرا لا يمكن إهماله.

Effect of Stiffeners on Shear Lag in Steel Box Girders

Mohannad H. M. Al-Sherrawi   Ghaidak Ahmed Fadhil

Department of Civil Engineering/ College of Engineering/University of Baghdad
Email: mhnd7@yahoo.com

Abstract

This paper studies the effects of stiffeners on shear lag in steel box girders with stiffened flanges. A three-dimensional linear finite element analysis using STAAD.Pro V8*i* program has been employed to evaluate and determine the actual top flange stress distribution and effective width in steel box girders. The steel plates of the flanges and webs have been modeled by four-node isoparametric shell elements, while the stiffeners have been modeled as beam elements. Different numbers (4, 8, and 15) for the steel stiffeners have been used in this study to establish their effects on the shear lag and longitudinal stresses in the flange. Using stiffeners reduced the magnitude of the top flange longitudinal stresses about 40%, but didn't affect the shear lag.

Keywords: Shear lag, effective width, box girder, stiffeners.

1. Introduction

A box girder is a beam which has the shape of a hollow box. The box girder normally comprises either structural steel, prestressed concrete, or a composite of steel and reinforced concrete. The box is typically rectangular or trapezoidal in cross-section. Box girder bridges are commonly used for highway flyovers and for modern elevated structures of light rail transport. Although normally the box girder bridge is a form of beam bridge, box girders may also be used on cable-stayed bridges and other forms.

1.1. Advantages and Disadvantages

Compared to I-beam girders, box girders have a number of key advantages and disadvantages. Box girders offer better resistance to torsion, which is particularly of benefit if the bridge deck is curved in plan. Additionally, larger girders can be constructed, because the presence of two webs allows wider and hence stronger flanges to be used. This in turn allows longer spans. On the other hand, box girders are more expensive to fabricate, and they are more difficult to maintain, because of the need for access to a confined space inside the box.

1.2. Shear Lag

The conventional engineering theory of bending assumes that plane sections remain plane, which means that shearing strains are neglected. The term shear lag is used to describe the discrepancies between the approximate engineering theory, and the real behavior that results in both the increases in the stresses in the flange component adjacent to the web component in a steel box girder, and to the decreases in the stresses in the flange component away from the web.

As shown in Figure (1), the longitudinal stress $\sigma_x(y)$ at the flange of a box section distributes uniformly with σ_b along the y-axis based on the elementary beam theory. However, at the intersection of the flange and web where $y = \pm b$, the actual maximum longitudinal stress $\sigma_{x,max}(y = \pm b)$ is higher than the average longitudinal stress of σ_b. This high stress of the transfer of the shear force from the web to the

flange edge is called the shear lag phenomenon (Timoshenko and Goodier 1970).

In the analysis of any box girder, it is important to take the effects of shear lag into account since these effects can lead to a significant increase in the longitudinal stresses developed in the flanges.
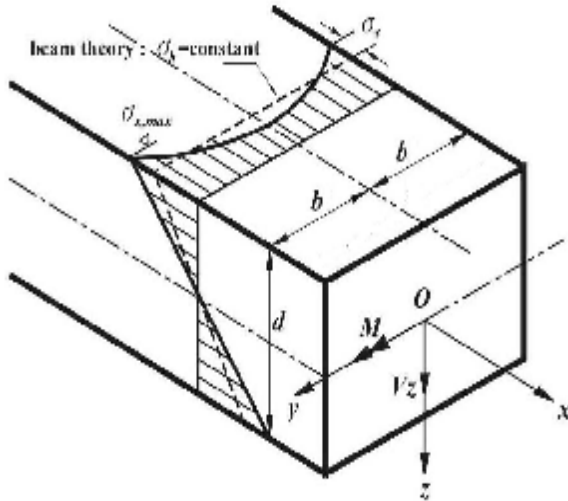

Fig. 1. Typical Box Section under Bending (Timoshenko and Goodier, 1970) .

1.3. STAAD.Pro V8i

STAAD.Pro V8*i* is a comprehensive and integrated finite element analysis and design offering, including a state-of-the-art user interface, visualization tools, and international design codes. It is capable of analyzing any structure exposed to static loading, a dynamic response, soil-structure interaction, wind, earthquake, and moving loads. STAAD.Pro V8*i* is the premier finite element method analysis and design tool for any type of project including towers, culverts, plants, bridges, stadiums, and marine structures

2. Review of the Previous Studies

Shear lag has long been of interest to researches. Firstly, shear lag in box girders was studied by Reisser (1946). Malcolm and Redwood (1970) suggested analytical procedure using stiffener-sheet solution. Moffatt and Dowling (1975) studied the shear lag phenomenon in steel box girder bridges by means of the finite element method of analysis. Kuzmanovic' and Graham (1981) found the minimum potential energy principle which was a suitable approach to evaluate the shear lag in box girders. Foutch and

Chang (1982) investigated the effects of shear lag and shear deformation on the static and dynamic response of tapered thin-walled box beams. Dezi and Mentrasti (1985) discussed nonuniform normal longitudinal stress distribution (shear lag) in a trapezoidal box beam with lateral cantilever. Chang and Zheng (1987) analyzed shear lag and negative shear lag effect in cantilever box girders through variation approach and finite element techniques. The substructuring analysis method for shear lag stress using the conditions of compatibility and equilibrium was introduced by Fafitis and Rong (1996) Lee and Wu (2000) improved the inefficiency of traditional finite element analysis using uniform meshes in the solution of shear lag stress. Wang (1997) derived an energy equation for the lateral buckling of thin-walled members with openings considering shear lag phenomenon. Also, Luo et al. (2001) studied the negative shear lag in box girder with varying depth. However, these studies recognized that the complicated equations are not so practical for the design of steel box girders. Luo et al. (2002) carried out experimental study on the shear lag effect of box girder with varying depth. Hwang et al. (2004) presented shear lag parameters for beam-to-column connections in steel box piers. Zhibin Lin and Jian Zhao (2010) used an energy-based variation analysis to evaluate the AASHTO provisions for effective flange width.

2.1. Shear Lag in Box Beam

Under symmetrical flexure, the distributions of bending stress across wide flanges of a girder cross section are non-uniform. The bending stress near the web is much larger than that far from the web, as shown in Figure (2-a). This phenomenon is usually noted as positive shear lag (Chang and Zhang, 1987).

In a cantilever box girder with constant depth, under uniform load, at the region beyond 1/4 the cantilever length from the built-in end, the bending stress near the web is much smaller than that far from the web. This result is opposite to positive shear lag and is called negative shear lag as shown in Figure (2-b) (Chang and Zhang, 1987).
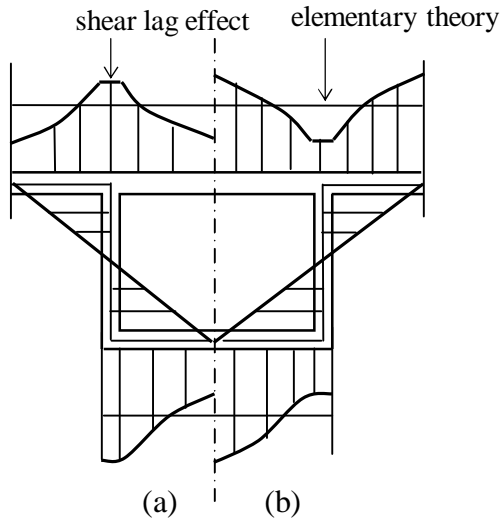
Fig. 2. Shear Lag Effecta) Positive shear lag, b) Negative Shear lag (Chang and Zhang, 1987).

2.2. Effective Flange Width

The effective width of a flange is the width of a hypothetical flange that compresses uniformly across its width by the same amount as the loaded edge of the real flange under the same edge shear forces. Alternatively, the effective width can be thought of as the width of theoretical flange which carries a compression force with uniform stress of magnitude equal to the peak stress at the edge of the prototype wide flange when carrying the same total compression force (Hamply, 1976).

The effective width concept has been widely recognized and implemented into different codes of practice around the world.

The effective width of a girder flange varies along the span and depends significantly on the load distribution, cross-sectional properties, and boundary conditions, as well as the plan dimensional of the girder (Moffatt and Dowling, 1975).

Effective width may be defined in a variety of ways depending on which design parameter is deemed more significant. It is generally obtained by integrating the rigorously calculated longitudinal stress in the flange, and dividing by the peak value of stress. And therefore $\bar{b}$ is calculated here by considering flange stress and is given by:

$$\bar{b} = \frac{\int_0^b \sigma_x \, dy}{(\sigma_x)_{max.}} \qquad \ldots(1)$$

Where $\bar{b}$ is one-side effective flange width, b is half flange width, σ_x represent the normal stress in the longitudinal direction, and $(\sigma_x)_{max.}$ is the maximum normal stress between $0 \leq y \leq b$. In this work, the numerator of Equation (1) was calculated by the approximate method by using trapezoidal rule; these calculations have been done by a computer program written for that purpose.

The main aim of the present study is to investigate the effect of the stiffeners on the top flange longitudinal stress distribution and effective width in steel box girders by using finite element method to idealize the steel box girder.

3. Finite Element Modeling

STAAD.Pro 2007 program was used to create three dimensional finite element model of the steel box girder. Three-dimensional four-node isoparametric shell elements were used to model the steel plates, while the stiffeners were modeled by beam elements. The steel model used for all components in the girder model was linear/elastic, the elastic modulus used was 29,000 ksi and the Poisson's ratio was 0.3 (ASTM A36).

The steel box girder used as a reference throughout this paper is based on the cross-section shown in Figure (3). The simply supported girder has a width that equals 144 in., a depth that equals 72 in., and a length that equals 720 in. The thickness of the steel plates equals 0.5 in. The stiffeners of each flange is 4.5 in. ×1 in. @ 9 in. c/c (total = 15). Same stiffeners wear used for top and bottom flanges to fix the distance between the neutral axis and the top flange as the stiffener ratio changed.
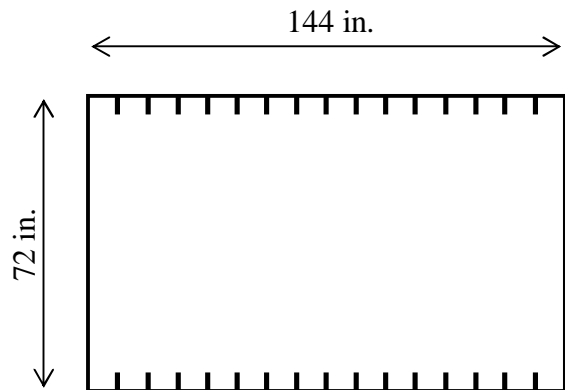

Fig. 3. Cross Section of the Reference Steel Box Girder .

The three-dimensional finite element mesh for the reference steel box girder used in STAAD.Pro V8*i* program is shown in Figure (4).
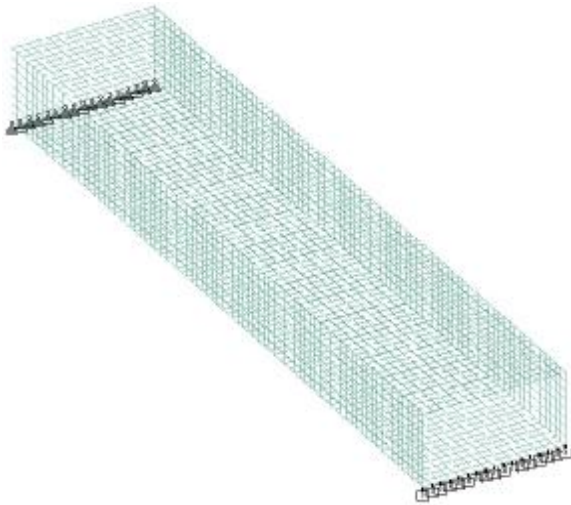

Fig. 4. Three-Dimensional Finite.

4. Parametric Study

In this section, influence of various parameters on top flange stress distribution and effective width in steel box girders were investigated. The parameters studied can be summarized as follows:

1. Stiffener ratio (area of stiffeners/area of top flange).
2. Distribution of Stiffeners.
3. Type of loading.
4. Depth/width of the section.
5. Length of girder.

In this work, two types of loading are investigated, the magnitude of the two loads was selected to give equal deflection at the mid-span, and these two cases will be referred to in the following as:

a. Uniformly distributed load (UDL) (150 kips) (on the overall flange).
b. Two concentrated loads (CL) (2×47 kips) at midspan (one on each web).

The maximum top flange stresses (over the web) for different stiffener ratios with respect to the two types of loading (UDL and CL) are listed in Table (1), and the distributions of the top flange stresses are shown in Figures (5 and 6) respectively. Each set of lines represent the edge of the effective width for one web. Adding stiffeners with area that equals the flange area decreases the maximum top flange stress in about 40%. The effective flange widths for different stiffener ratios with respect to the two types of loading are shown in Table (2), and the distribution of the effective flange widths is shown in Figures (7 and 8) respectively. It can be seen from the results obtained that:-

- The top flange longitudinal stresses decrease as the stiffener ratio increases. The decreasing ranged between 18% and 40%. This is due to the share of the stiffeners in the forces makes the stresses in the flange decrease.
- The maximum top flange longitudinal stress over each web decreases as the stiffener ratio increases. The decreasing reached 40%.
- The addition of stiffeners to the flanges results no effect on shear lag because the shear lag phenomenon does not affect the shape of the flange.
- The effective width decreases slightly as the stiffener ratio increases (5% in case of UDL and 13% in case of CL).

Table 1,
Maximum Top Flange Stresses for Different Stiffener Ratios with Respect to the Two Types of Loading (UDL and CL).

	Maximum Top Flange Stress									
Stiffener Ratios	**UDL**					**CL**				
	Beam Length Percentage					**Beam Length Percentage**				
	0.1 L	**0.2 L**	**0.3 L**	**0.4 L**	**0.5 L**	**0.1 L**	**0.2 L**	**0.3 L**	**0.4 L**	**0.5 L**
0.0	1067	1551	1964	2234	2328	664	1109	1627	2211	3356
0.5	880	1190	1464	1653	1719	521	813	1178	1625	2642
1.0	780	999	1195	1334	1385	436	646	930	1302	2239

Table 2,
Effective Flange Widths for Different Stiffener Ratios with Respect to the Two Types of Loading.

Stiffener Ratios	Effective Flange Width									
	UDL					CL				
	Beam Length Percentage					Beam Length Percentage				
	0.1 L	0.2 L	0.3 L	0.4 L	0.5 L	0.1 L	0.2 L	0.3 L	0.4 L	0.5 L
0.0	93	127	135	136	136	104	139	143	140	111
0.5	80	119	129	132	133	92	134	140	135	103
1.0	73	113	125	128	129	86	131	138	132	96

Another parameter, investigated is changing the number (4, 8, and 15) of the stiffeners with keeping the same area of the stiffeners. Effect of distribution of stiffeners on maximum top flange stress and the effective flange widths are listed in Table (3). Figures (9 and 10) show the distribution of the top flange stress and the effective flange respectively. The results declare that there are no effects because the stiffeners have the same area in all three cases.

Table 3,
Effect of Distribution of Stiffeners on Maximum Top Flange Stress and the Effective Flange Widths.

Number of Stiffeners	Maximum Top Flange Stress					Effective Flange Width				
	Beam Length Percentage					Beam Length Percentage				
	0.1 L	0.2 L	0.3 L	0.4 L	0.5 L	0.1 L	0.2 L	0.3 L	0.4 L	0.5 L
4	797	1022	1220	1361	1411	72	115	126	129	130
8	784	1005	1202	1339	1389	73	113	125	129	130
15	781	999	1195	1335	1385	73	113	125	128	129

Table (4) shows the maximum top flange stresses and effective flange widths according to type of loading. The distribution of longitudinal normal stresses in the top flange has different shapes along the flange according to type of loading as shown in Figure (11). The distribution of the effective flange widths which is due to type of loading is shown in Figure (12).

Table 4,
Maximum Top Flange Stresses and Effective Flange Widths According to Type of Loading.

Type of Loading	Maximum Top Flange Stress					Effective Flange Width				
	Beam Length Percentage					Beam Length Percentage				
	0.1 L	0.2 L	0.3 L	0.4 L	0.5 L	0.1 L	0.2 L	0.3 L	0.4 L	0.5 L
UDL	781	999	1195	1335	1385	73	113	125	128	129
CL	436	647	930	1302	2240	86	131	138	132	95

Effect of the ratio depth/width on the maximum top flange stresses and the effective flange widths is listed in Table (5), and the effect on the top flange stresses distribution and the effective flange widths distribution for different ratios is shown in Figures (13 and 14) respectively.

Table 5,
**Effect of the Ratio of Depth/Width on Maximum Top Flange Stresses and Effective Flange Widths.**

Depth/Width	Maximum Top Flange Stress Beam Length Percentage					Effective Flange Width Beam Length Percentage				
	0.1 L	0.2 L	0.3 L	0.4 L	0.5 L	0.1 L	0.2 L	0.3 L	0.4 L	0.5 L
0.5	781	999	1195	1335	1385	73	113	125	128	129
1.0	151	420	541	606	630	116	111	122	127	128

Table (6) shows the effect of length of girder on the maximum top flange stresses and effective flange widths and Figure (15 and 16) show the top flange stress distribution and the distribution of the effective flange widths for different lengths of the girder.

Table 6,
Effect of Length of Girder on Maximum Top Flange Stresses and Effective Flange Widths.

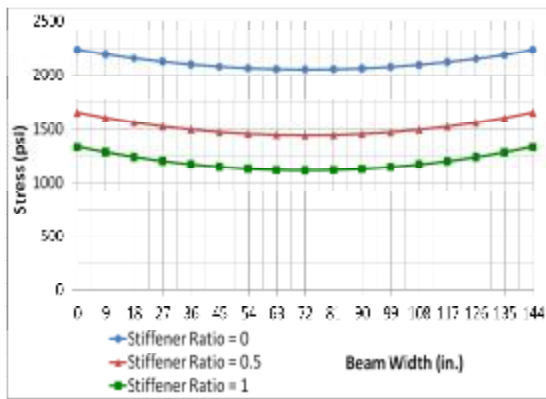| Length of Girder	Maximum Top Flange Stress Beam Length Percentage					Effective Flange Width Beam Length Percentage				
	0.1 L	0.2 L	0.3 L	0.4 L	0.5 L	0.1 L	0.2 L	0.3 L	0.4 L	0.5 L
37.5	333	560	603	636	651	52	78	98	107	110
60.0	781	999	1195	1335	1385	73	113	125	128	129
82.5	1203	1667	2112	2392	2487	96	128	134	135	136
105.0	1676	2579	3330	3787	3940	114	135	137	138	139
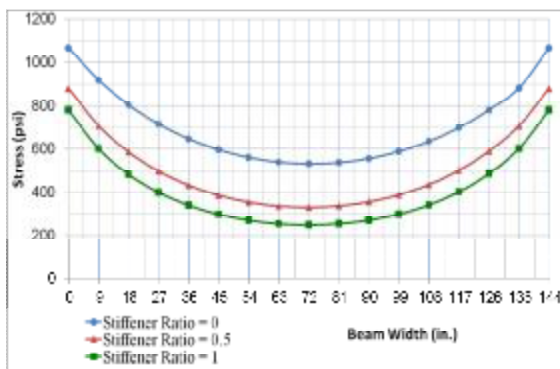
(a)
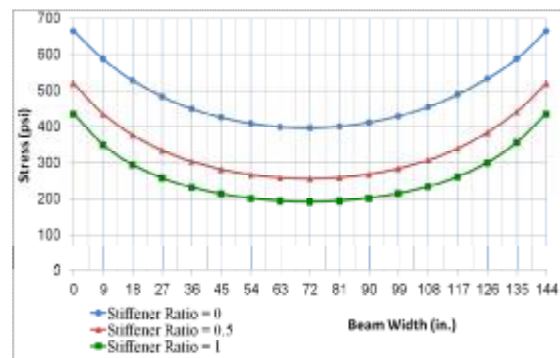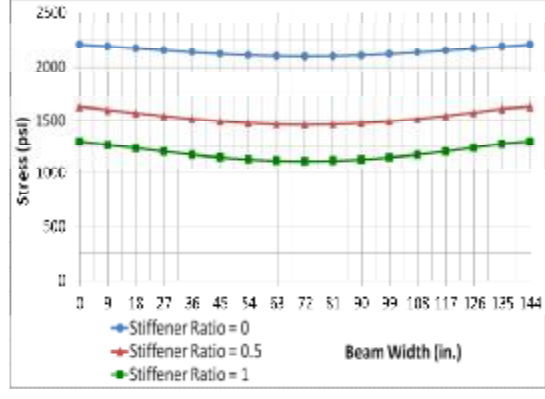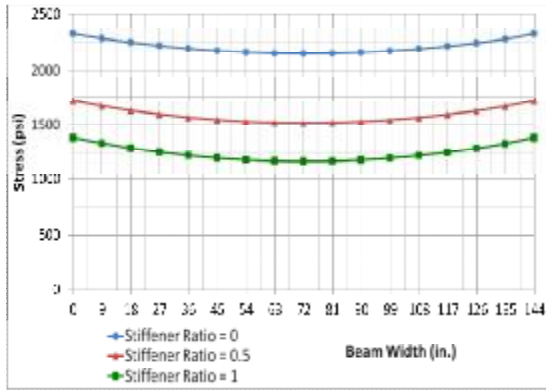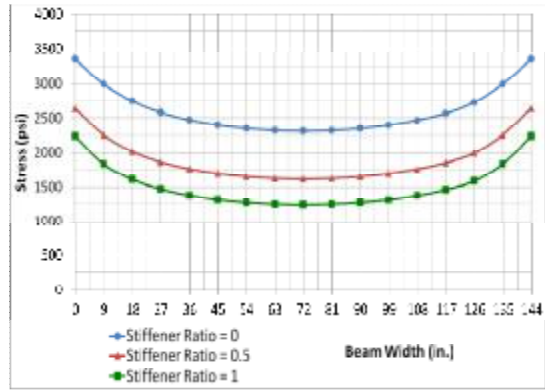

(a)
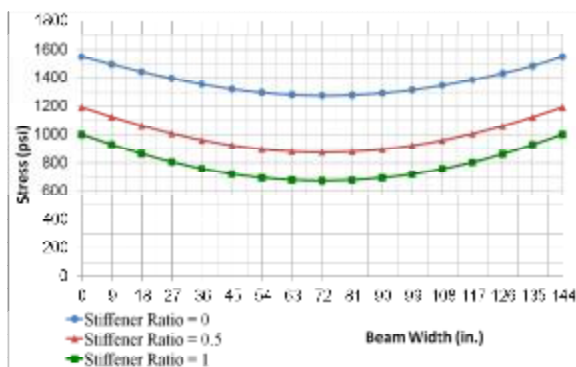
(b)
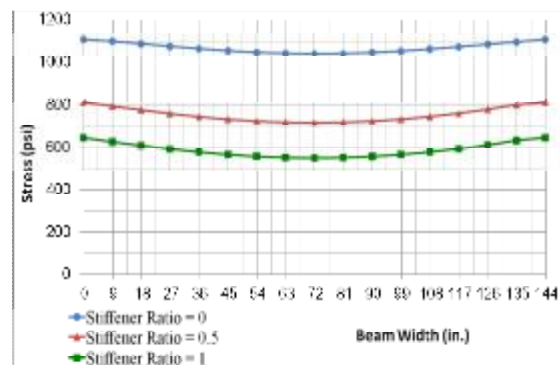
(b)
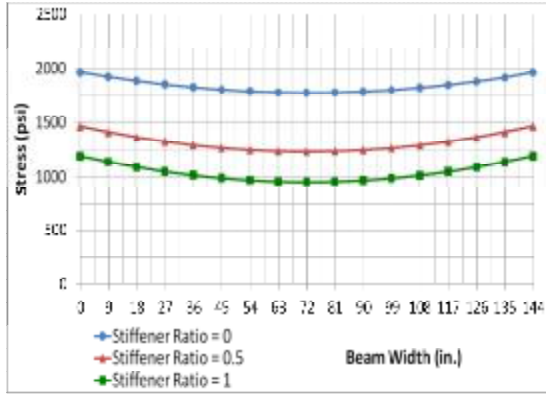
(c)
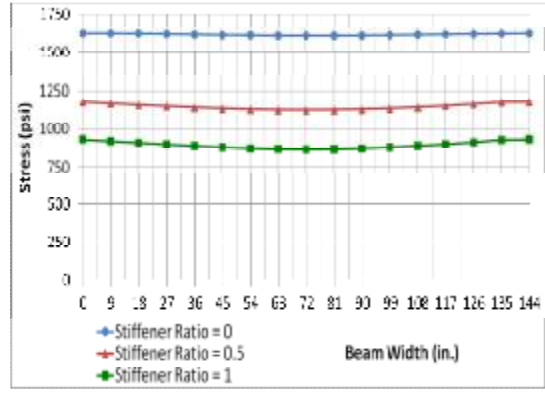
(c)

(d)

(d)

(e)

(e)

Fig. 5. Effect of Stiffener Ratio on Top Flange Stress Distribution (UDL). (a) At 0.1 L   (b) At 0.2 L (c) At 0.3 L   (d) At 0.4 L   (e) At 0.5 L.

Fig. 6. Effect of Stiffener Ratio on Top Flange Stress Distribution (CL). (a) At 0.1 L   (b) At 0.2 L (c) At 0.3 L   (d) At 0.4 L   (e) At 0.5 L
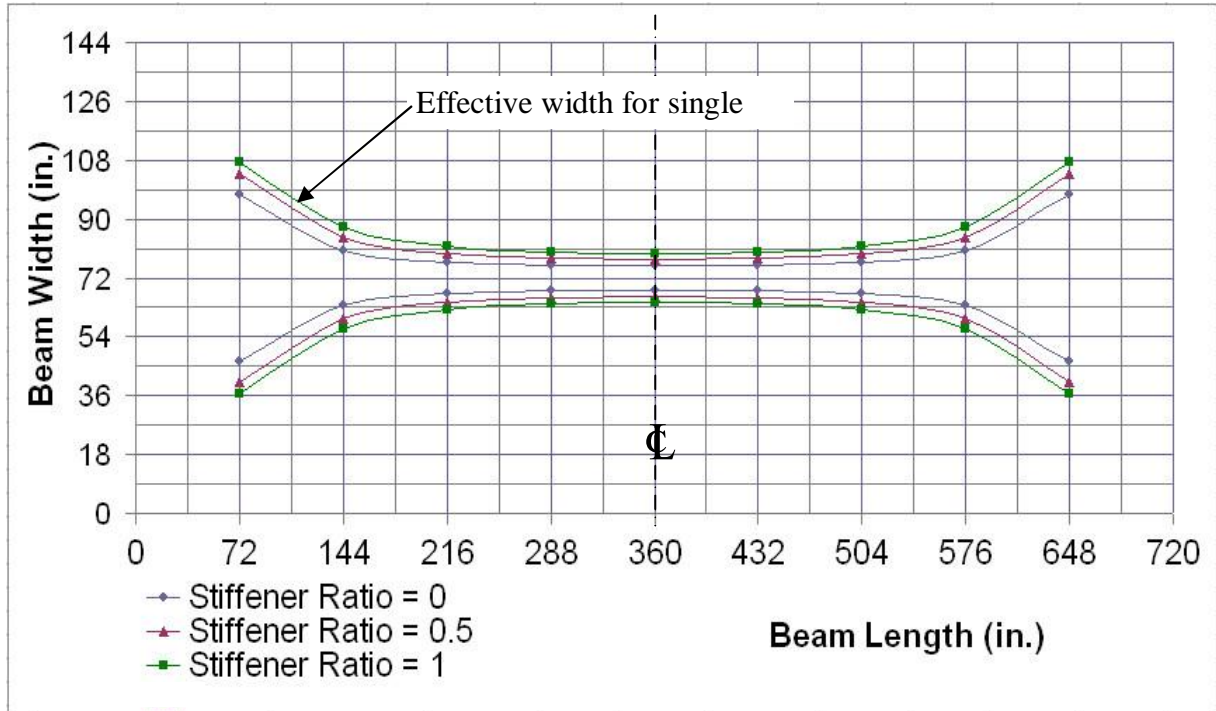
Fig. 7. Effect of Stiffener Ratio on the Distribution of the Effective Flange Widths (UDL).
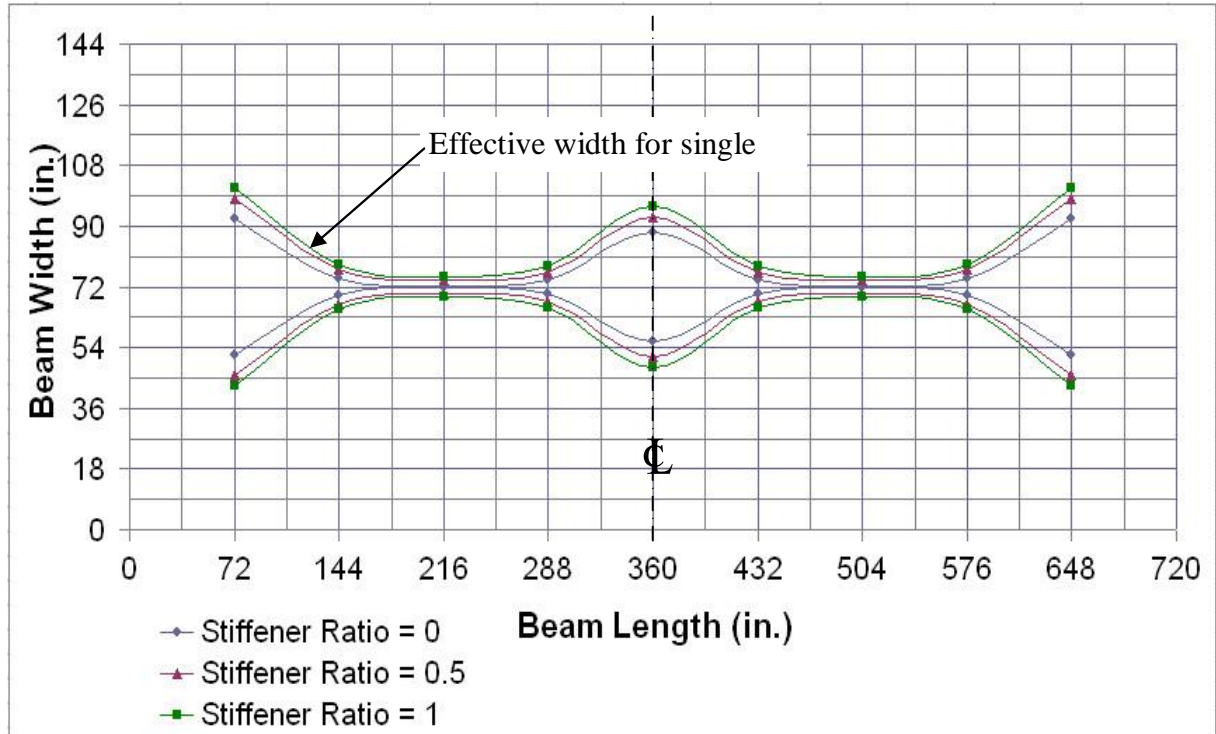

Fig. 8. Effect of Stiffener Ratio on the Distribution of the Effective Flange Widths (CL).
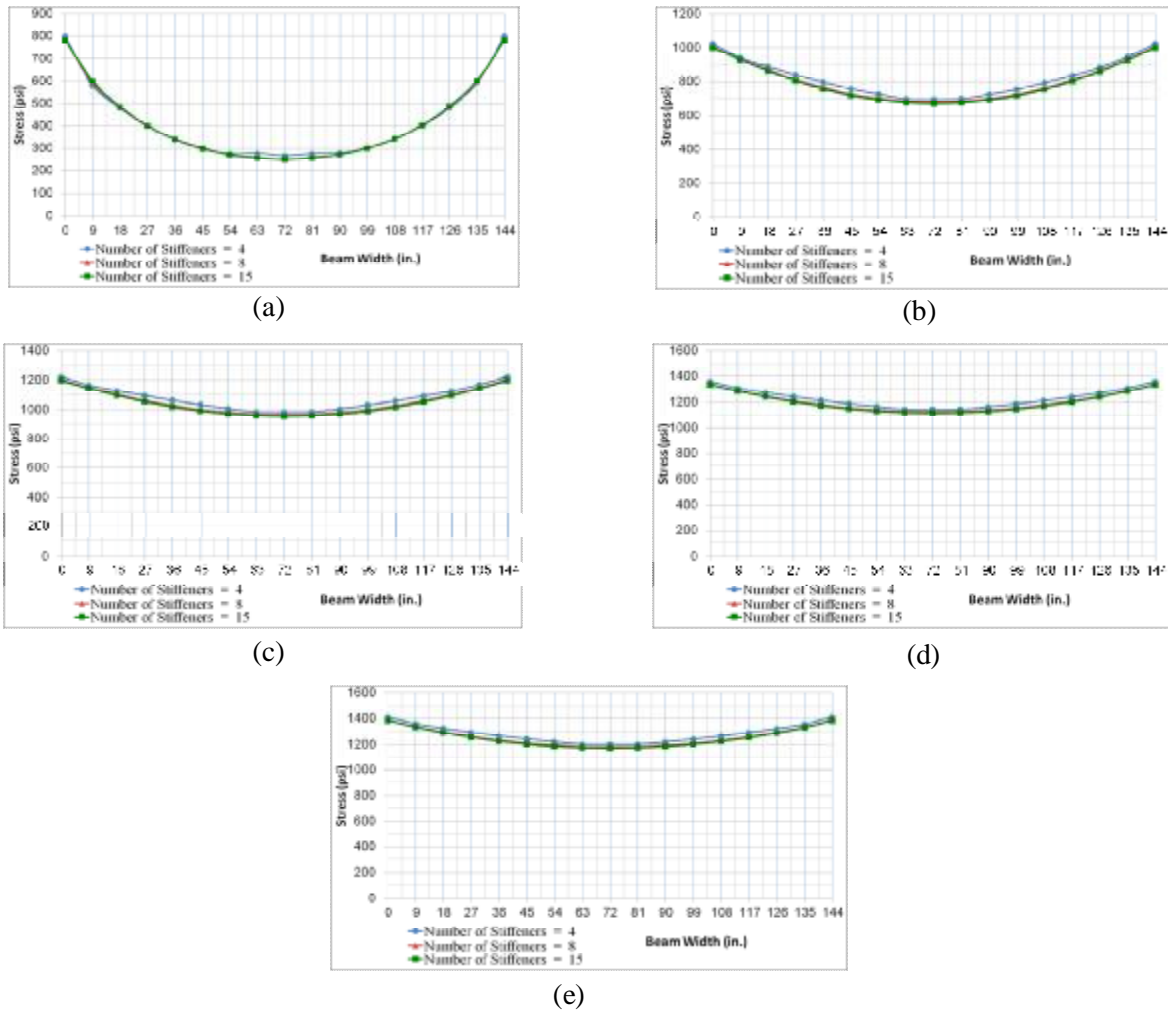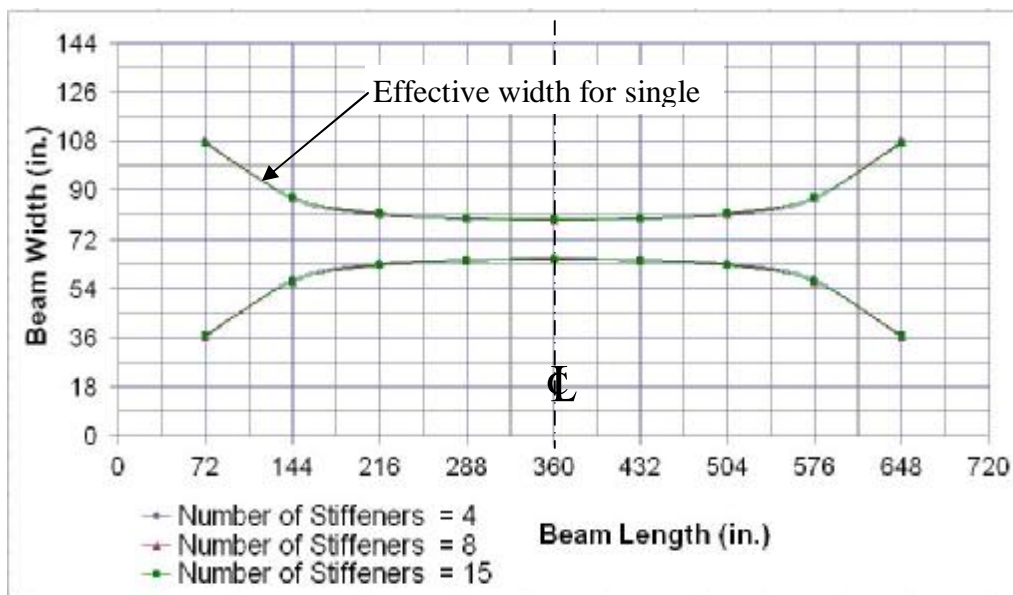
(a)   (b)   (c)   (d)   (e)

Fig. 9. Effect of Distribution of Stiffeners on Top Flange Stress Distribution .
(a) At 0.1 L   (b) At 0.2 L   (c) At 0.3 L   (d) At 0.4 L   (e) At 0.5 L.
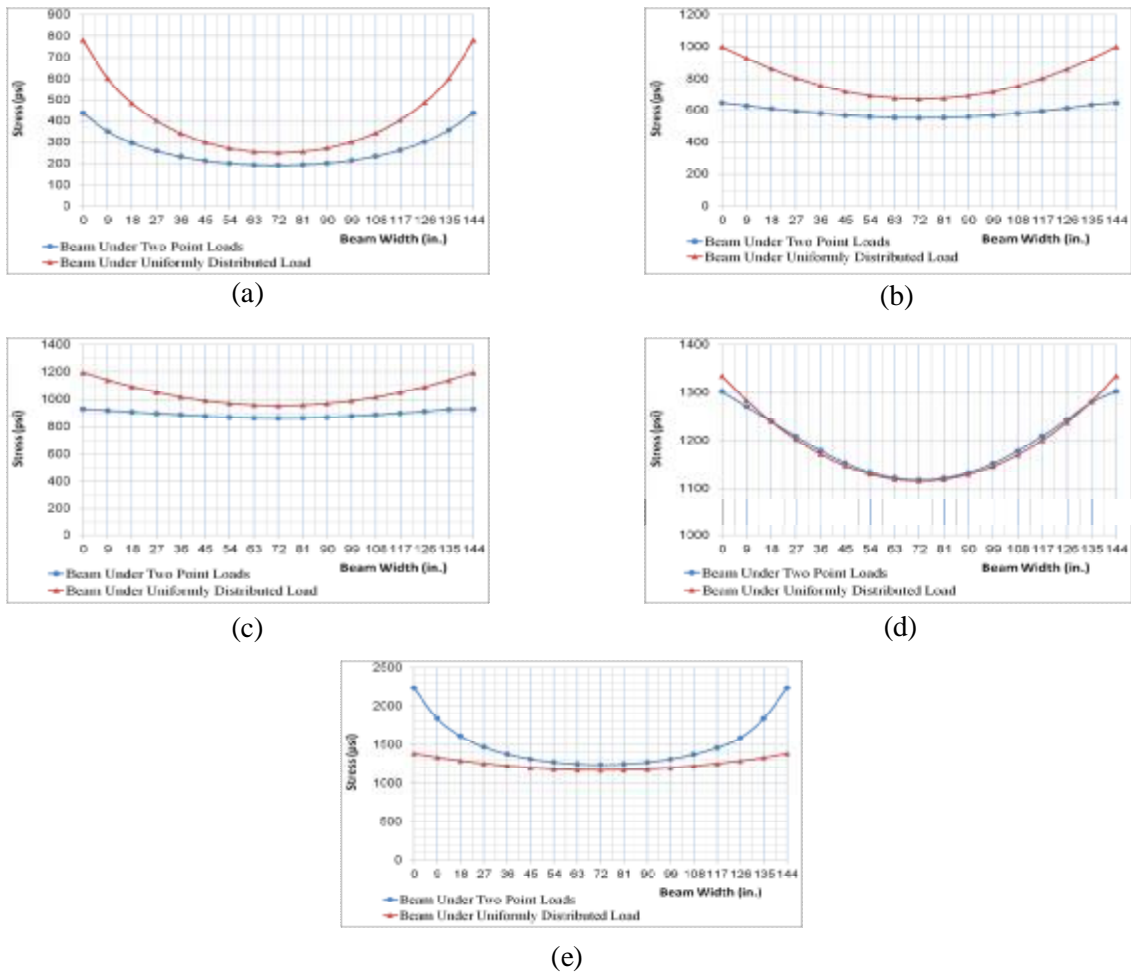
Fig. 11. Effect of Loading on Top Flange Stress Distribution.
(a) At 0.1 L   (b) At 0.2 L   (c) At 0.3 L   (d) At 0.4 L   (e) At 0.5 L.
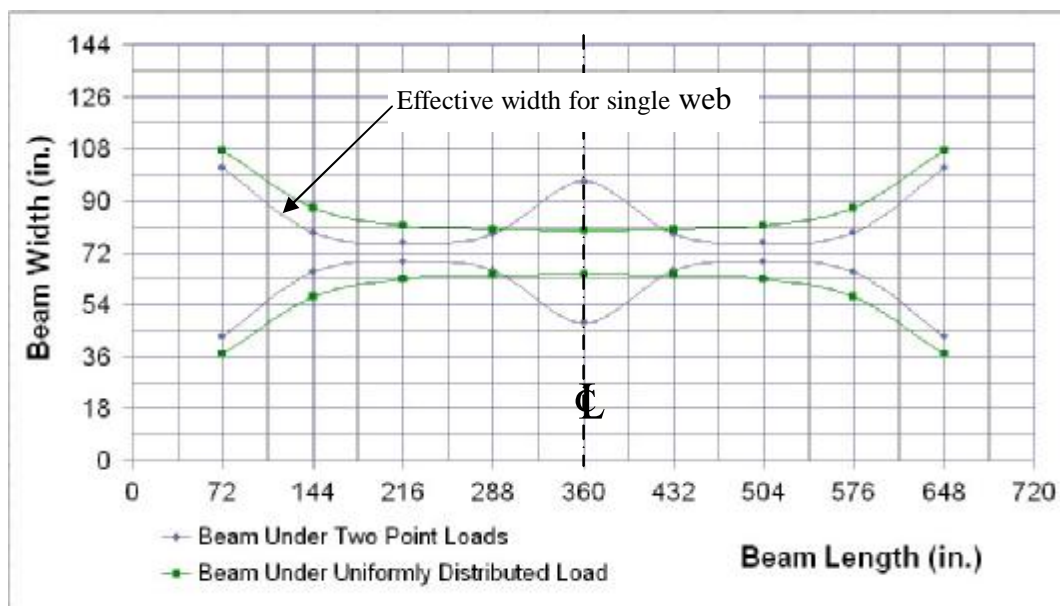

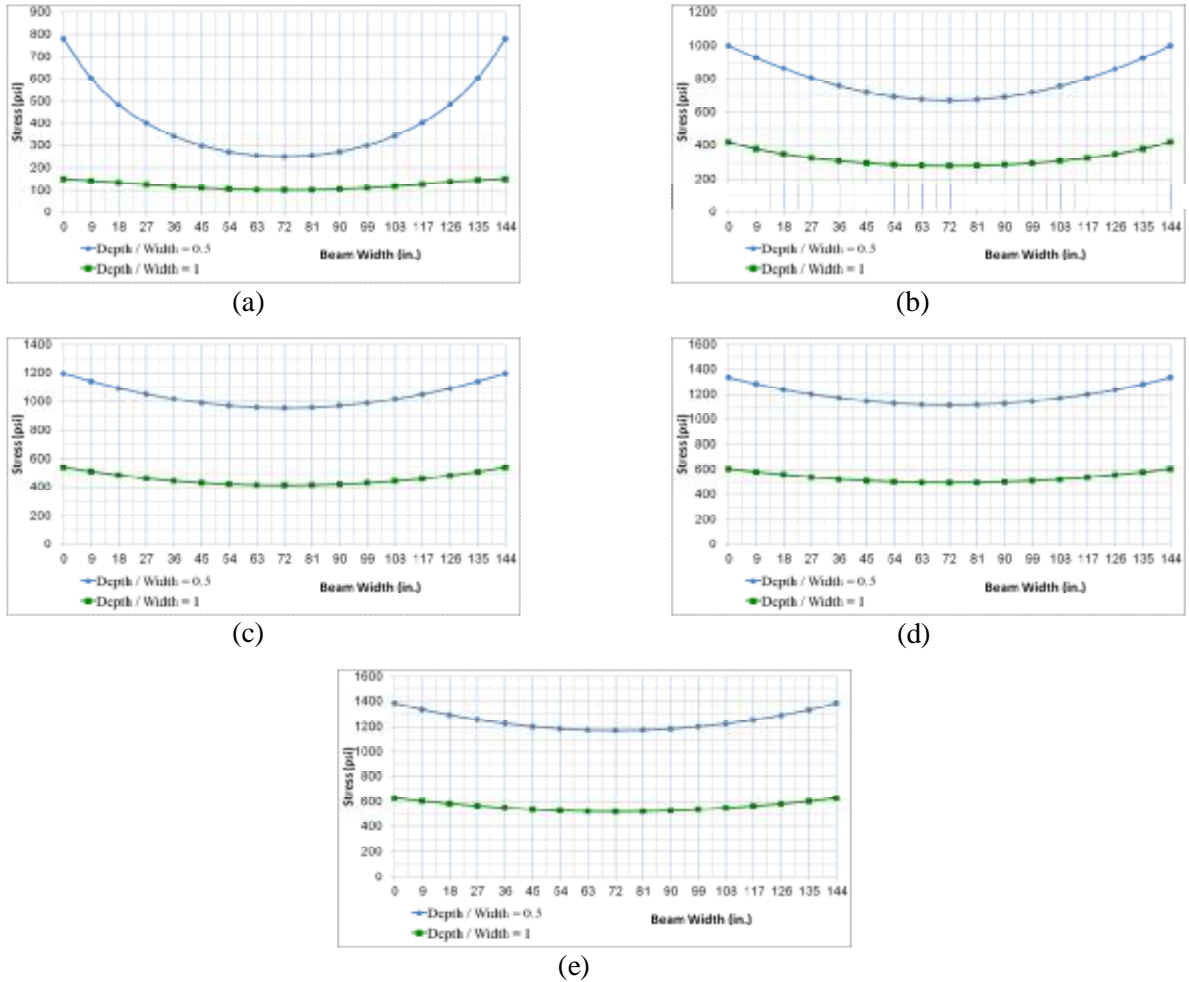**Fig. 12. Effect of Loading on the Distribution of the Effective Flange Widths .**

Fig. 13. Effect of Depth/Width on Top Flange Stress Distribution.
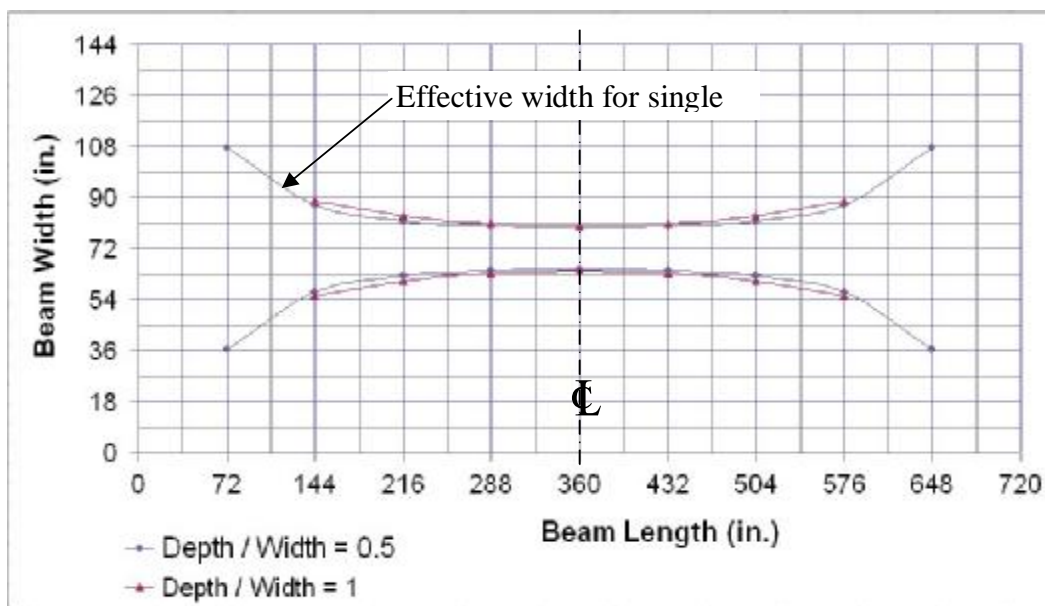**(a) At 0.1 L   (b) At 0.2 L   (c) At 0.3 L   (d) At 0.4 L   (e) At 0.5 L.**

Fig. 14.Effect of Depth/Width on the Distribution of the Effective Flange Widths.
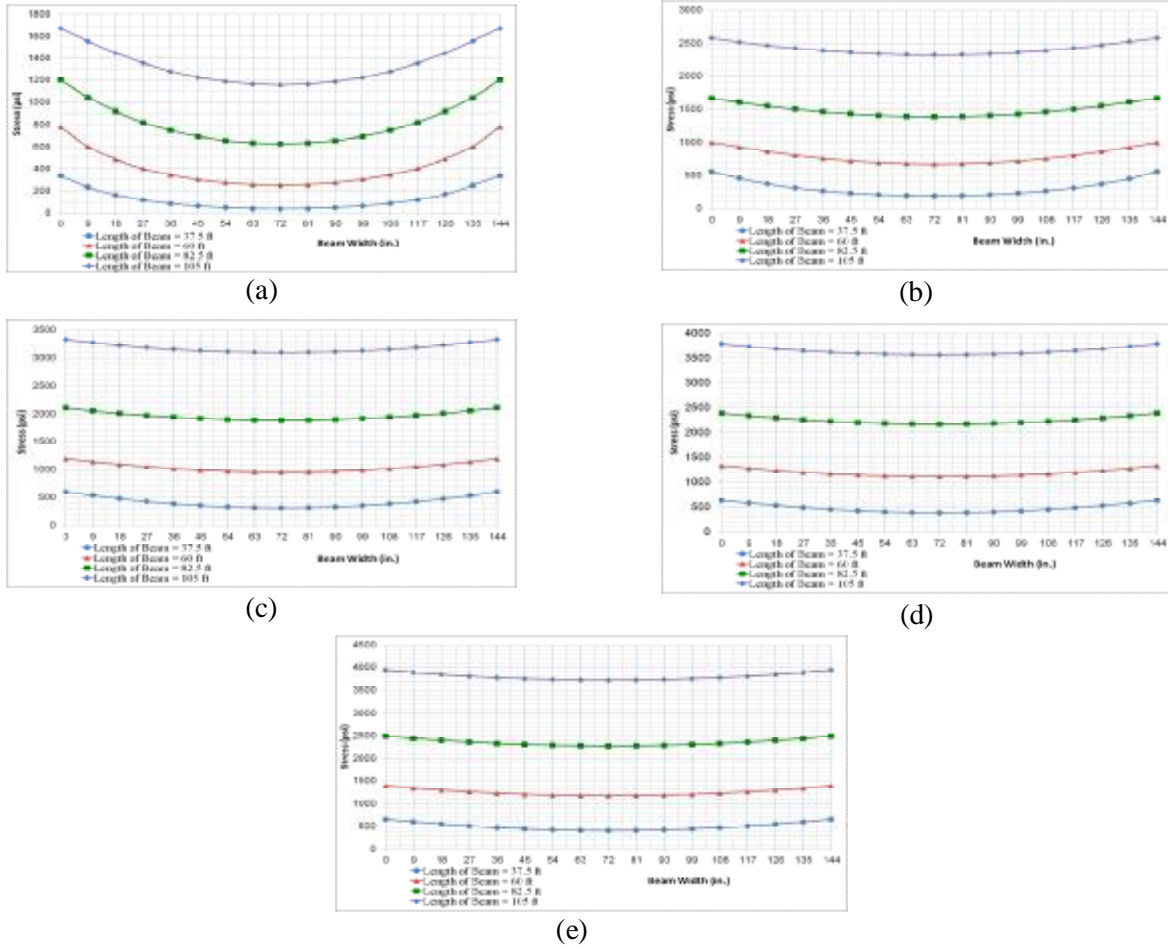
(a)

(b)

(c)

(d)

(e)

Fig. 15. Effect of Length of Girder on Top Flange Stress Distribution.
(a) At 0.1 L   (b) At 0.2 L   (c) At 0.3 L   (d) At 0.4 L   (e) At 0.5 L.
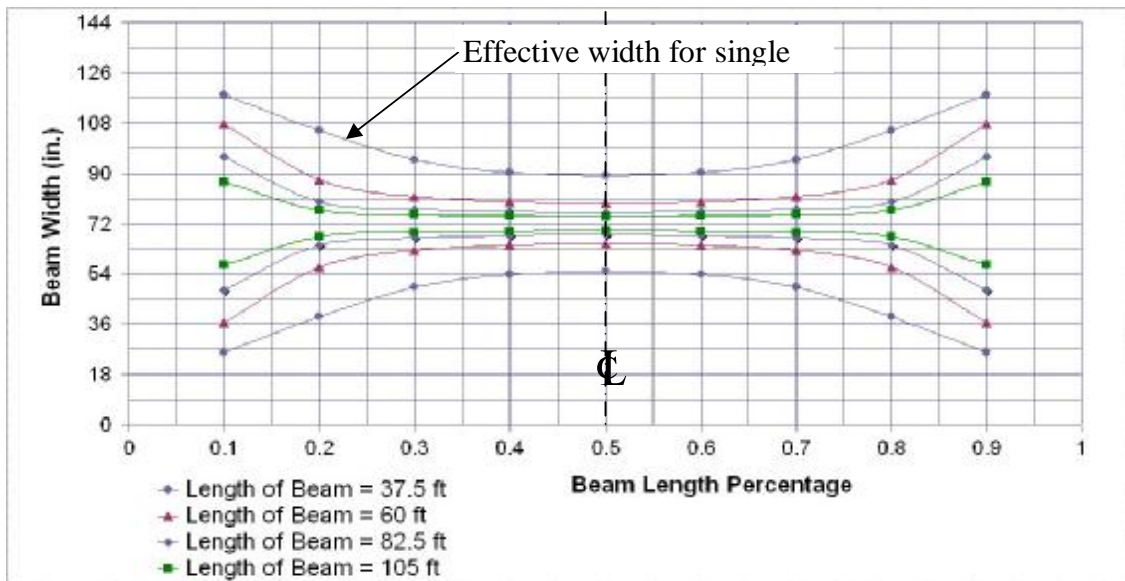

Fig. 16. Effect of Length of Girder on the Distribution of the Effective Flange Widths.

5. Conclusions

1. Using the longitudinal stiffeners in the flanges of steel box girder did not affect the shear lag in the top flange, although it reduced the magnitude of the top flange longitudinal stresses to about 40%, and decreases slightly the effective width (5%-13%) because portion of these stresses go to the stiffeners.
2. Increasing the stiffener ratio make the top flange longitudinal stresses decrease.
3. Changing the number (4, 8, and 15) of the stiffeners with keeping the same area of the stiffeners has no effects on the magnitude of the top flange longitudinal stresses due to using the same area of the stiffeners.

Notations

b	One-Side Slab Width
$\overline{b}$	One-Side Effective Slab Width
E_s	Modulus of Elasticity of Steel
L	Span Length of the Beam
ν	Poisson's Ratio
σ_x	Normal Stress in the Longitudinal Direction
$(\sigma_x)_{max.}$	Maximum Normal Stress in the Longitudinal Direction

6. References

[1] Chang, S. T., and Zheng, F. Z. (1987) "Negative Shear Lag in Cantilever Box Girder with Constant Depth." Journal of the Structural Engineering, Vol. 113, No. 1, January, pp. 20-35.

[2] Dezi, L., and Mentrasti, L. (1985) "Non-uniform Bending-Stress Distribution (Shear Lag)," Journal of the Structural Engineering, Vol. 111, No. 12, pp. 2675-2690.

[3] Fafitis, A. and Rong, A. Y. (1995), "Analysis of thin-walled box girders by parallel processing", Thin-walled Struct., 21, 233-240.

[4] Foutch, D. A., and Chang, P. C. (1982) "A Shear Lag Anomaly," Journal of the Structural Engineering, Vol. 108, No. 7, pp. 1653-1658.

[5] Hamply, E. C., (1976) Bridge Deck Behavior, Chapman and Hall, London EC4P 4EE, pp. 272.

[6] Hwang, W. S., Kim, Y. P., and Park, Y. M. "Evaluation of shear lag parameters for beam-to-column connections in steel piers" Structural Engineering and Mechanics, Vol. 17, No. 5 (2004) 691-706.

[7] Kuzmanovi , B. O. and Graham, H. J. (1981), "Shear lag in box girder", J. Struct. Div., ASCE, 107(9), 1701-1742.

[8] Lee, C. K. and Wu, G. J. (2000), "Shear lag analysis by the adaptive finite element method-1. Analysis of simple plated structures", Thin-walled Struct., 38, 285-309.

[9] Luo, Q. Z., Tang, J., and Li, Q. Z. (2001) "Negative Shear Lag Effect in Box Girders with Varying Depth," Journal of Structural Engineering, ASCE, , Vol. 127, No. 10, pp. 1236-1239.

[10] Luo, Q. Z., Tang, J. and Li, Q. S. (2002), "Experimental studies on shear lag of box girder", Eng. Struct., 24, 464-477.

[11] Malcolm, D. J. and Redwood, R. G. (1970), "Shear lag in stiffened box girders", J. Struct. Div., ASCE, 96 (ST7), 1403-1449.

[12] Moffatt, K. R., and Dowling, P. J. (1975) "Shear Lag in Steel Box Girder Bridges," The Structural Engineer, Vol. 53, No. 10, October, pp. 439-448.

[13] Reissner, E. (1946), "Analysis of shear lag in box beams by the principle minimum potential energy", Quarterly App. Math., 3 (3), 268-278.

[14] Timoshenko, S. P., and Goodier, J. N. (1970) "Theory of Elasticity." third edition, Mc Graw-Hill, New York, pp. 567.

[15] Wang, Q. F. (1997), "Lateral buckling of thin-walled members with openings considering shear lag", Structural Engineering and Mechanics, 5 (4), 369-383.

[16] Zhibin Lin, A. M. and Jian Zhao, A. M. "A Revisit of AASHTO Effective Flange Width Provisions for Box Girders" Journal of Bridge Engineering / Accepted Manuscripts in 2010.

تأثير المقويات على تخلف القص في الأعتاب الصندوقية الحديدية

مهند حسين محسن الشراوي   غيدق أحمد فاضل

قسم الهندسة المدنية / كلية الهندسة / جامعة بغداد

البريد الالكتروني: mhnd7@yahoo.com

الخلاصة

هذا البحث يوثق دراسة تأثير المقويات على تخلف القص في الأعتاب الصندوقية الحديدية ذات الشفاه المقواة. أعتمد التحليل بإستعمال طريقة العناصر المحددة الخطية ثلاثية الأبعاد وباستخدام برنامج ستاد برو في التحليل وحساب التوزيع الحقيقي للإجهادات في الشفة العليا والعرض الفعال في الأعتاب الصندوقية الحديدية. تم تمثيل الصفائح الحديدية للشفتين والوترتين بإستعمال عناصر قشرية رباعية العقد ، بينما تم تمثيل المقويات بعناصر أحادية البعد ذات عقدتين. أعداد مختلفة للمقويات (٤ ، ٨ ، ١٥) تم إستخدامها في هذه الدراسة لمعرفة تأثيرها على تخلف القص والإجهادات بالإتجاه الطولي في الشفة. إن إستخدام المقويات يقلل من قيمة الإجهادات بالإتجاه الطولي في الشفة العليا بمقدار يصل إلى ٤٠ % ، لكنه لا يؤثر على تخلف القص فيها.

Experimental and Numerical Study of Crack Effect on Frequency of Simple Supported Beam

Luay S. Al-Ansari   Muhannad Al-Waily   Ali M. H.Yusif Al-Hajjar

Department of Mechanical Engineering/College of Engineering/ University of Kufa

Abstract

In this research the natural frequency of a cracked simple supported beam (the crack is in many places and in different depths) is investigated analytically, experimentally and numerically by ANSYS program, and the results are compared. The beam is made of iron with dimensions of L*W*H= (0.84*0.02* 0.02m), and density = 7680kg/m^3, E=200Gpa. A comparison made between analytical results from ANSYS with experimental results, where the biggest error percentage is about (7.2 %) in crack position (42 cm) and (6 mm) depth. Between Rayleigh method with experimental results the biggest error percentage is about (6.4 %) for the same crack position and depth. From the error percentages it could be concluded that the Rayleigh method gives close results to experimental than ANSYS. Also it is found that the frequency of beam when the crack is in the middle position is less than the frequency with crack near the end position.

1. Introduction

The importance of the beam and its engineering applications is obvious, and it undergoes many different of loading. Many types of loading may cause cracks in the beam. These cracks and their locations effect on the shapes and values of the beam frequency. Recently these topics are so prevailing in the industry of spacecraft, airplanes, wind turbines, turbines, robot arm and many other applications.

Many studies were performed to examine the vibration and dynamic of cracked beams; one of them was Shen and Pierre[1],who present a finite element approach which make it possible to predict in the first few eigen frequencies due to cracks (pairs or single open cracks).The change in the first natural frequency with crack depth is matched closely by the present finite element approach and also with the experimental results.

Also, Shen and Pierre [2] derived the equation of motion with associated boundary conditions for uniform Bernoulli-Euler beam. The resulting equation is solved for simple supported and cantilevered beams with single edge cracks by Galerkin and Ritz procedure; they matched the theoretical results with the experimental and finite element results and they match closely.

Chati et . al. [3] modeled the non-linearity as a piecewise-linear system. In an attempt to define effective natural frequencies for this piecewise linear system, the idea of a 'bilinear frequency' is utilized. The finite element method is used to obtain the natural frequencies in each linear region.

Choondros et. al [4]studied the dynamics of a cracked fixed-free bar with a breathing crack in longitudinal vibration. They showed in results the eigenfrequency changes due to a single open-edge breathing crack in order to depend on the bilinear character of the system. They tested their method fordifferent bar configurations corresponding to crack location, crack depths, cross-section dimensions, andPoisson's ratio. The natural frequencies obtained from this model agree well with experimental results.

Choondros et. al [5]used a continuous cracked beam vibration theory for predication of changes in transverse vibration of simply supported beam

with a breathing crack. They found that the changes in vibration frequencies for fatigue breathing crack are smaller than the ones caused by open cracks. Utilizing aluminum beams with fatigue cracks for experimental setup they compared the results with the analytical.

Chondros[6]used a continuous cracked beam vibration theory for predication of changes in dynamic characteristic due to loading conditions and vibration amplitude. He used the numerical results to correlate the analytical results for lumped crack beam vibration analysis for aluminum and steel beams with open cracks. He supported the theoretical result by experimental results for the same cases.

Cam and et. al. [7] studied ,experimentally and theoretically, the effect of the crack on vibration of cracked beam. They used echo method for predication the size and location of the crack in cracked beam. They found that the theoretical results (ANSYS) agreed with experimental results.

In this paper, three approaches are employed, an analytical approach is compared with experimental result and with that gained numerically by ANSYS program to verify the results.

The objective of this paper is to study the effect of crack depth and position on the natural frequency of the simple supported beam and to find the best method that gives good results to be compared with experimental results.

2. Theoretical Approach

2.1. Analytical Approach (Rayleigh method)

Rayleigh method is a good method and simpler than the other analytical methods for finding the natural frequencies. It includes calculating the kinetic energy and potential energy of the system. where the kinetic energy can be calculated by integration the mass through length of the beam and the potential energy by integration the stiffness through the length of the beam. So one can get from the above, S. S. Rao [12]:

$$w^2 = \frac{\int_0^l EI\left(\frac{d^2 y(x)}{dx^2}\right)^2 dx}{\int_0^l rA(y(x))^2 dx} = \frac{g\sum_{i=1}^{n+1} m_i y_i}{\sum_{i=1}^{n+1} m_i y_i^2} \quad \dots (1)$$

Where,

ω is the natural frequency of beam.

E is the modulus of elasticity of beam (N/m2).

I is the second moment area od cross section area of beam (m4).

ρ is the mass density of beam (kg/m3).

A is the cross section area of beam (m2).

g is the gravity acceleration (9.81 m/s2).

m_i is the mass in each Rayleigh divided point of beam.

y_i is the deflection in each Rayleigh divided point of beam.

By calculating the deflection of the beam(y(x)) using the following steps:

1. Dividing the beam into (n) parts (i.e. (n+1) nodes).
2. Calculating the delta matrix $[\delta]_{((n+1)*(n+1))}$.
3. Calculating the mass matrix $[m]_{((n+1))}$.
4. Calculating the deflection at each node by multiplying delta matrix and mass matrix ($[y]_{(n+1)} = [\delta]_{((n+1)*(n+1))} [m]_{((n+1))}$) after applying the boundary conditions.

The analytical results are solved using MATLAB. Where a MATLAB program that simulated the Rayleigh method is written in order to calculate the first natural frequency of any beam (Different materials, different dimensions and different shape).

2.2. Numerical Approach (Finite Elements Method)

In this method, the finite elements method was applied by using the ANSYS program(ver.13). The three dimensional model were built and the element (Solid Tet 10 node 187) were used.

Generally the number of nodes was approximately (1250-1300) and the number of elements was (550-600). A sample of meshed beam is shown in Fig. 1.

a) Meshed Beam without Crack.

b) Meshed Beam with Crack at 12 cm from Left End.

c) Meshed Beam with Crack at 22 cm from Left End.

d) Meshed Beam with Crack at 32 cm from Left End.

e) Meshed Beam with Crack at 32 cm from left End.

**Fig. 1. A sample of a Meshed Beam.**

3. Experimental Approach

The (TM16 universal vibration apparatus) from TQ company is employed in this study and is shown in Fig. 3. The dimensions of the specimen used are (L*W*H=0.84*0.02 *0.02 m) as shown in Fig. 2. The material of the specimen was stainless steel (Code No.: 314, Robert L. Norton [16]) with density of (7680 kg/m^3), calculate by divided the weight of beam per volume of beam, Young modulus (200 GPa) and Poisson's Ratio (0.3).

The crack was created in the specimens with certain dimensions of crack ;(see Table (1)).

Table 1,
Dimensions of the Cracks that Used Experimentally.

Specimen No.	Crack Location (m)	Crack Length (m)	Crack Width (m)	Crack Depth (mm)					
1	0.12	0.2	0.0015	0	2	4	6	8	10
2	0.22	0.2	0.0015	0	2	4	6	8	10
3	0.32	0.2	0.0015	0	2	4	6	8	10
4	0.42	0.2	0.0015	0	2	4	6	8	10
5	0.54	0.2	0.0015	0	2	4	6	8	10
6	0.64	0.2	0.0015	0	2	4	6	8	10
7	0.74	0.2	0.0015	0	2	4	6	8	10

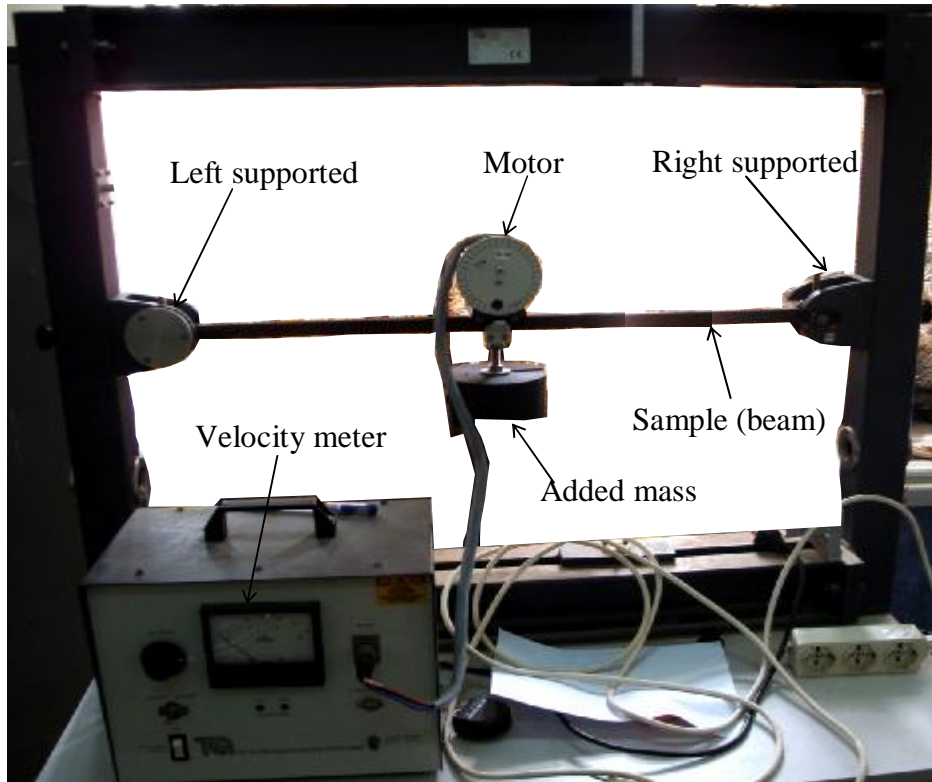**(a) Dimensions of sample**
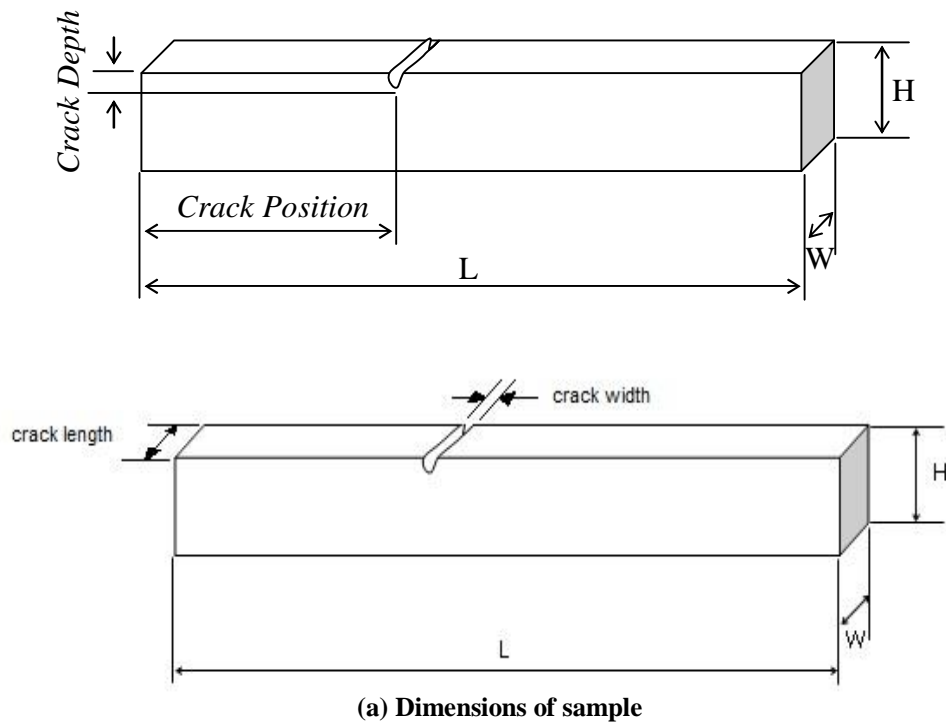
(b) Sample of beam

(c) Different Crack Position

Fig. 2. Dimension and Crack Depth and Crack Position of Samples Test.

(a) The Universal Vibration Apparatus.

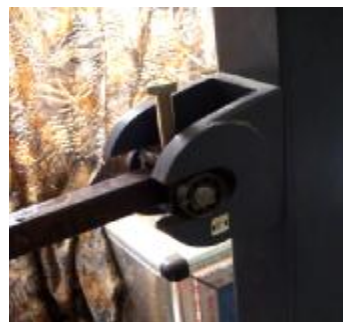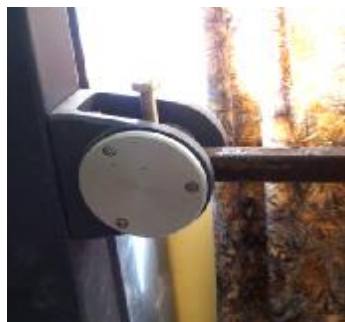

(b) Motor.   **(c) Added Mass.**   **(d) Velocity Meter.**

(e) Left and Right Supported.

Fig. 3. The Universal Vibration Apparatus.

Table 2,
Natural Frequency with Different Crack Position and Crack Depth.

| Crack Position (cm)	Crack Depth (mm)	Frequency (Hz)			Error Exp. and ANSYS (%)	Error Exp. and Rayleigh (%)
		Experimental	**ANSYS**	**Rayleigh Method**		
12	0	143.74	148.81	145.2758759	3.5	1.06
	2	141.42	148.7	145.2784708	5.15	2.73
	4	146.805	148.46	145.2810655	1.13	1.04
	6	141.99	148.01	145.2836602	4.2	2.3
	8	142.5665	147.39	145.2862548	3.4	1.9
	10	139.75	146.5	145.2888493	4.8	3.96
22	0	143.74	148.81	145.2758759	3.5	1.07
	2	153.57	148.8	145.2784708	3.1	5.4
	4	149.4	148.77	145.2873931	0.42	2.75
	6	152.85	148.69	145.2931524	2.7	4.9
	8	149.4	148.61	145.2989122	0.53	2.7
	10	141.42	148.43	145.3046725	4.95	2.7
32	0	143.74	148.81	145.2758759	3.5	1.07
	2	150	148.65	145.2784708	0.9	3.15
	4	139.2	148.17	145.2873931	6.4	4.4
	6	139.75	147.35	145.2931524	5.4	3.96
	8	142.56	146.03	145.2989122	2.4	1.9
	10	138.144	144.03	145.3046725	4.26	5.18
42	0	143.74	148.81	145.2758759	3.5	1.06
	2	140.3	148.54	145.2886394	5.87	3.6
	4	141.3	147.77	145.3014064	4.6	2.8
	6	136.59	146.44	145.3141768	7.2	6.4
	8	140.3	144.43	145.3269508	2.9	3.6
	10	141.99	141.44	145.3397282	0.39	2.4
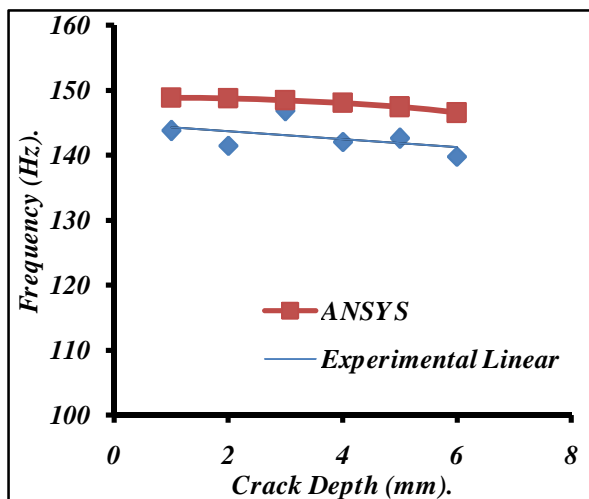
Fig. 4. The Comparison between the Experimental and ANSYS Results at Different Crack Depths When the Crack lies at (12 cm) .
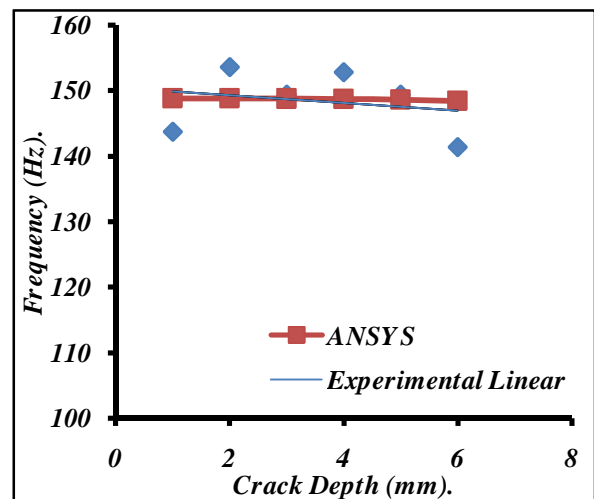

Fig. 5. The Comparison between the Experimental and ANSYS Results at Different Crack Depths When the Crack lies at (22 cm) .
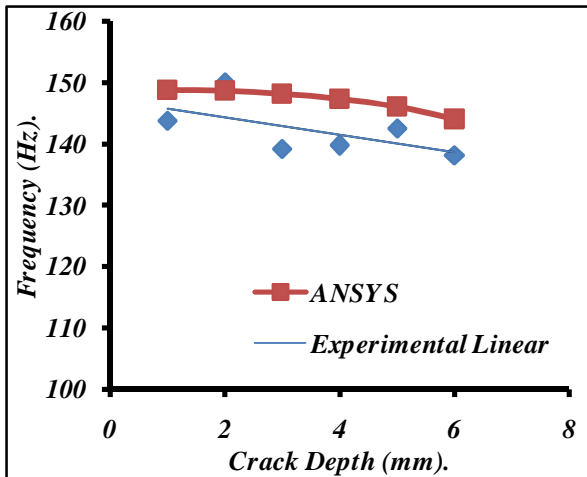
Fig. 6. The Comparison between the Experimental and ANSYS Results at Different Crack Depths When the Crack lies at (32 cm) .
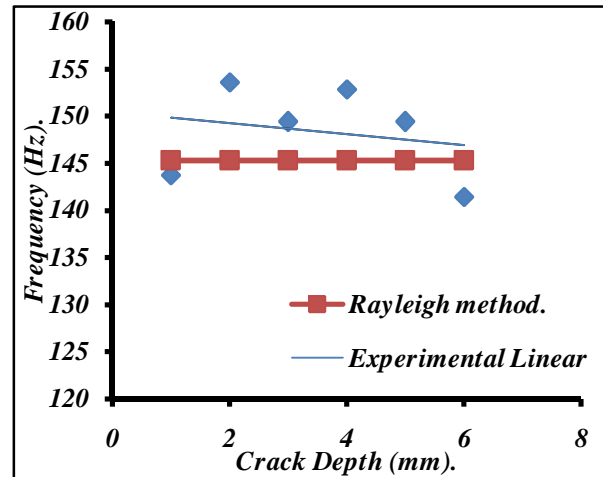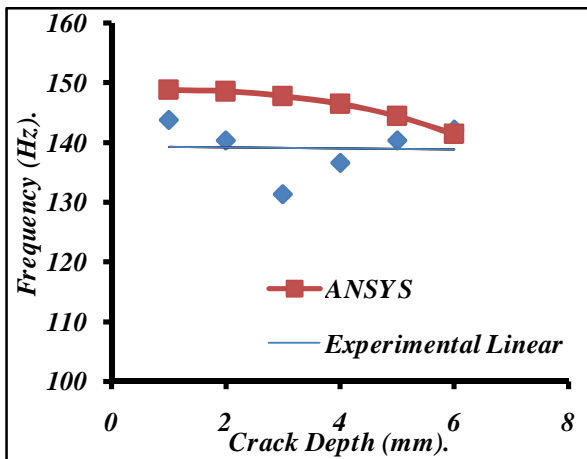

Fig. 7. The Comparison between the Experimental and ANSYS Results at Different Crack Depths When the Crack lies at (42 cm) .
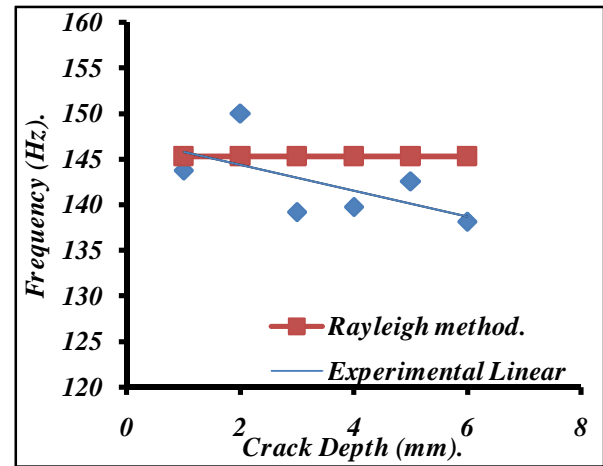

Fig. 8. The Comparison between the Experimental and Rayleigh Method Results at Different Crack Depths When the Crack lies at (12 cm) .

Fig. 9. The Comparison between the Experimental and Rayleigh Method Results at Different Crack Depths When the Crack lies at (22 cm) .

Fig. 10. The Comparison between the Experimental and Rayleigh Method Results at Different Crack Depths When the Crack lies at (32 cm) .
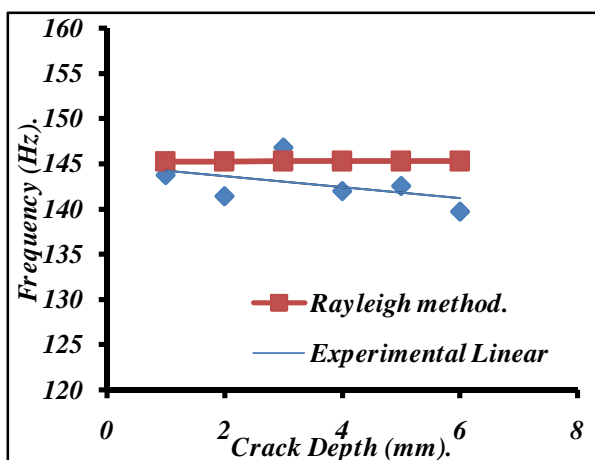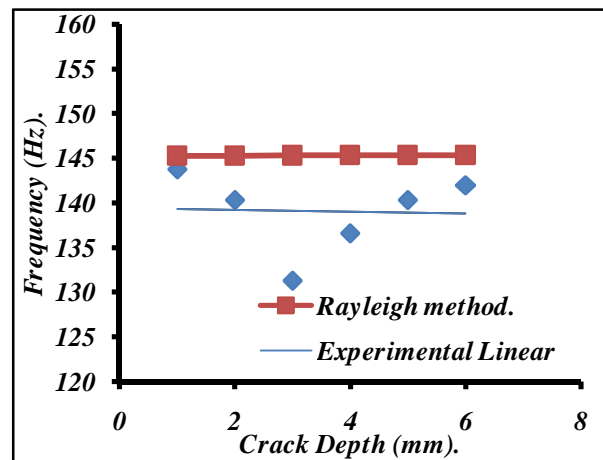

Fig. 11. The Comparison between the Experimental and Rayleigh Method Results at Different Crack Depths When the Crack lies at (42 cm) .
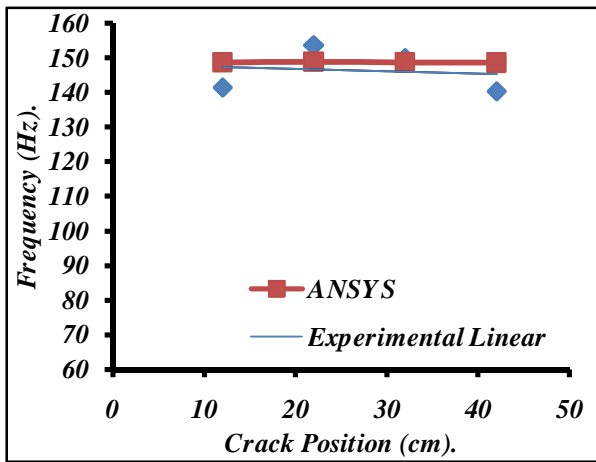
Fig. 12. The Comparison between the Experimental and ANSYS Results at Different Crack Position When the Crack Depth is (2mm).

Fig. 15. The Comparison between the Experimental and ANSYS Results at Different Crack Position When the Crack Depth is (8mm).

Fig. 13. The Comparison between the Experimental and ANSYS Results at Different Crack Position When the Crack Depth is (4mm) .

Fig. 16. The Comparison between the Experimental and ANSYS Results Different at Crack Position When the Crack Depth is (10mm) .
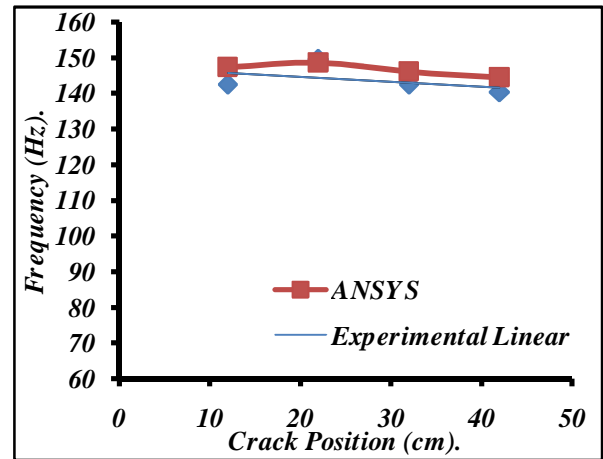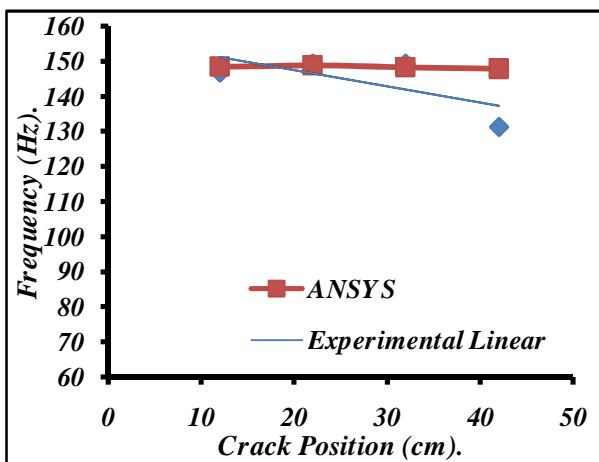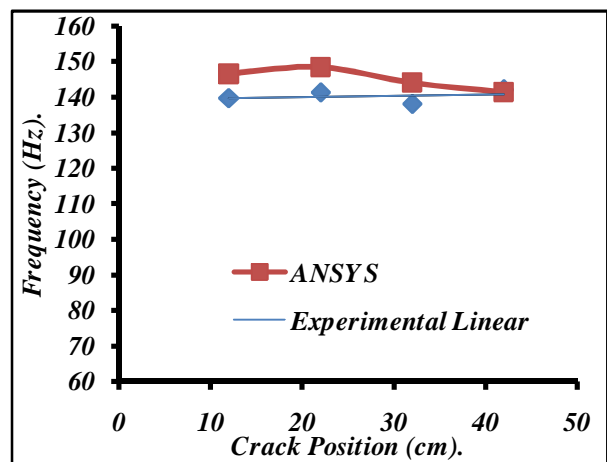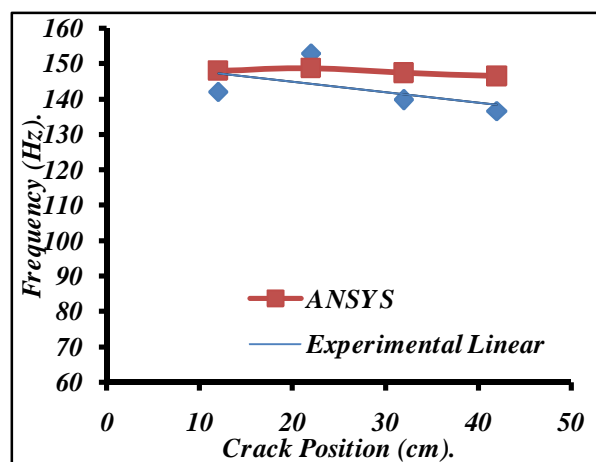

Fig. 14. The Comparison between the Experimental and ANSYS Results Different at Crack Position When the Crack Depth is (6mm) .

Fig. 17. The Comparison between the Experimental and Rayleigh Method Results at Different Crack Position When the Crack Depth is (2mm) .

Fig. 18. The Comparison between the Experimental and Rayleigh Method Results at Different Crack Position When the Crack Depth is (4mm).

Fig. 19. The Comparison between the Experimental and Rayleigh Method Results at Different Crack Position When the Crack Depth is (6mm).

Fig. 20. The Comparison between the Experimental and Rayleigh Method Results at Different Crack Position When the Crack Depth is (8mm).

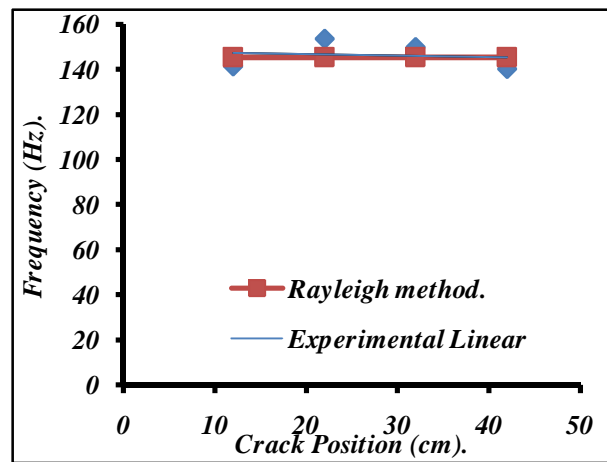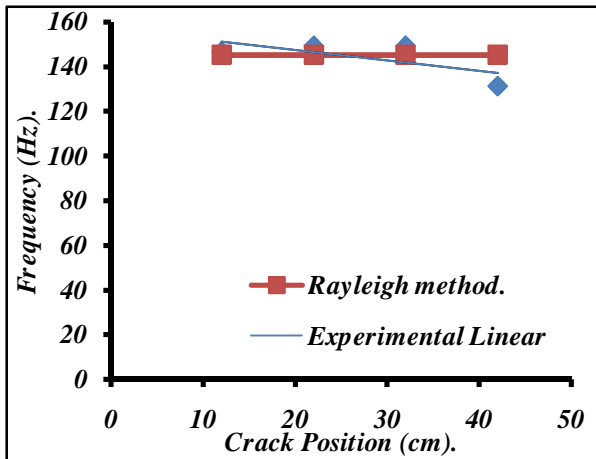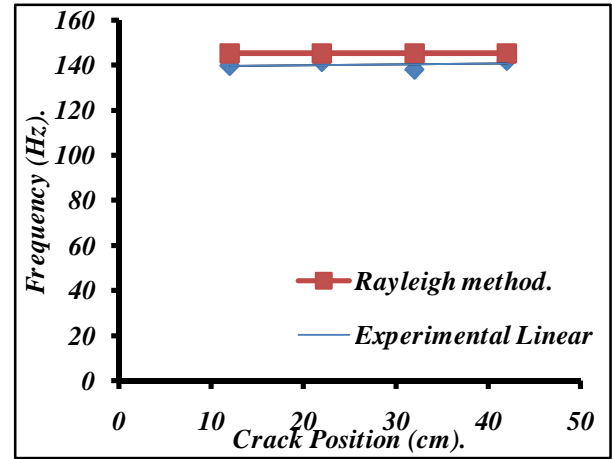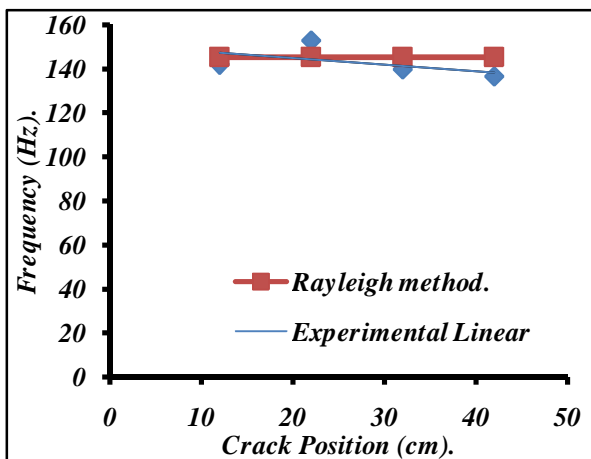**Fig. 21. The Comparison between the Experimental and Rayleigh Method Results at Different Crack Position When the Crack Depth is (10mm).**
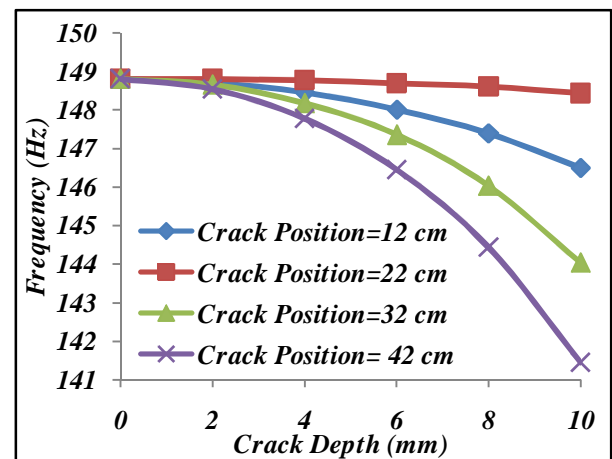

Fig. 22. Relationship between Natural Frequencies and Crack Depths for Different Crack position (12, 22, 32, 42 cm). ANSYS Results.
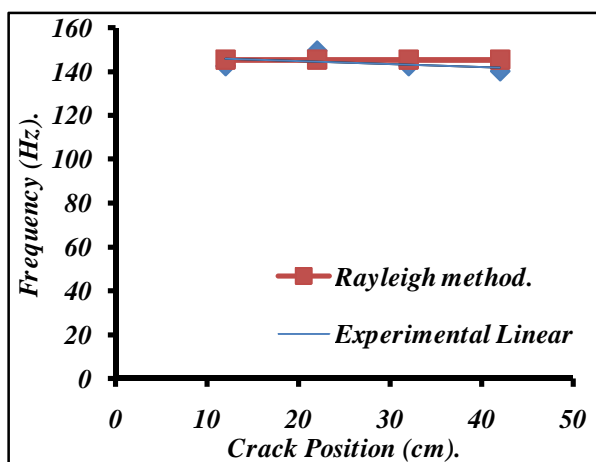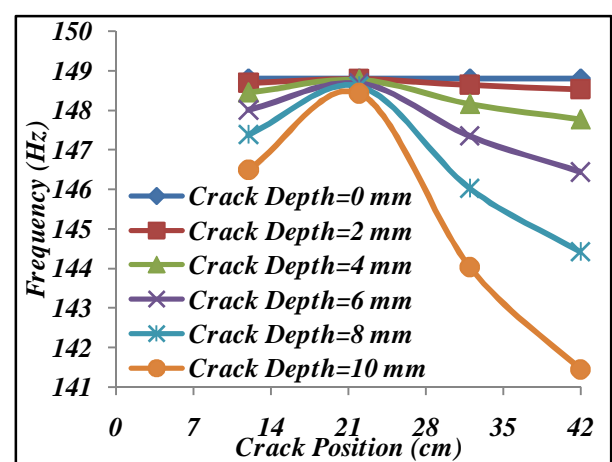

Fig. 23. Relationship between Natural Frequencies and Crack position for Different Crack Depths (0, 2, 4, 6, 8, 10 mm). ANSYS Results.

4. Results and Discussion

A comparison made between analytical results from ANSYS with experimental results shows a good approximation where the biggest error percentage is about (7.2 %) in crack position (42 cm) and (6 mm) depth, as illustrated in Fig. 7. and the comparison between Rayleigh method with experimental results shows a good approximation where the biggest error percentage is about (6.4 %) in crack position (42 cm) and (6 mm) depth, as illustrated in Fig. 11.

Figs. 4, 5, 6, and 7. explain the comparison between theoretical results (ANSYS) and experimental results for natural frequency and how it changes with crack depth for different crack position (12, 22, 32, and 42 cm) where the natural frequency decreased with increasing crack depth for the same crack position because of the decreasing of stiffness of the beam.

Figs. 8, 9, 10, and 11. show the comparison between Rayleigh method and experimental results for natural frequency and how it changes with crack depth for different crack position (12, 22, 32, and 42 cm) where the natural frequency decreased with increasing crack depth for the same crack position because of decreasing of stiffness of the beam.

Figs. 12, 13, 14, 15, and 16. The explain the comparison between theoretical results (ANSYS) and experimental results for natural frequency and how it changes with crack position for different crack depth (2, 4, 6, 8, and 10 mm) where the natural frequency decreased with increasing crack position for the same crack depth because of the decreasing of stiffness of the beam.

Figs. 17, 18, 19, 20, and 21. explain the comparison between Rayleigh method and experimental results for natural frequency and how it changes with crack position for different crack depth (2, 4, 6, 8, and 10 mm) where the natural frequency decreased with increasing crack position for the same crack depth because of the decreasing of stiffness of the beam.

Generally from all the figures one can see that the natural frequency decreases with increasing crack depth for different crack positions because of the changing in stiffness of the beam. And the rate of decreasing for experimental is close for different crack positions. For ANSYS the rate of decreasing of natural frequency is the biggest in crack position (42 cm). And, for Rayleigh method the rate of decreasing is close for different crack positions, as shown in Figs. 22. and 23. and Table (2).

5. Conclusion

From the results shown in the Figs. 4 to 23, the following concluding marks are observed:

1- A comparison made between analytical results from ANSYS with experimental results shows a good approximation where the biggest error percentage is about (7.2 %) in crack position (42 cm) and (6 mm) depth, as shown in Fig. 7.

2- The comparison between Rayleigh method with experimental results shows a good approximation where the biggest error percentage is about (6.4 %) in crack position (42 cm) and (6 mm) depth, as shown in Fig. 11.

3- From the error percentages in Table 2, the Rayleigh method gives close results to experimental than ANSYS.

4- The crack in the beam has an effect on the stiffness of the beam; this will affect the frequency of the beam. So, with the increasing of the crack depth, the stiffness of beam will decrease and this will cause a decreasing in the natural frequency of the beam.

5- The position of crack in the beam near the middle of the beam has more effect on the stiffness and natural frequency of beam from the other positions (near to the ends of the beam), i.e. frequency of the beam when the crack is in the middle position has a lower frequency of the beam with respect the cracks near to the end position.

6. References

[1] Shen, M. -H. H and Pierre C. . "Modes of free vibrations of cracked beams", paper (of 46 pages) presented to UM-MEAM, (1986).

[2] Shen, M. -H. H and Pierre C. . "Free Vibrations of Beams With a Single Edge Crack", Journal of sound and vibration, 170(2), pp. 237-259. (1994).

[3] Chati, M., Rand, R. and Mukherjee, S. "Modal analysis of a cracked beam", Journal of sound and vibration, 207(2), pp. 249-270. (1997).

[4] Chondros T. G., Dimarogonas A. D. and Yao J " Longitudinal vibration of a bar with a breathing crack", Engineering fracture mechanics, pp.503-518, 1998.

[5] Chondros T. G., Dimarogonas A. D. and Yao J. "Vibration of a beam with a breathing crack" journal of sound and vibration, 239(1), pp. 57-67. (2001).

[6]   Chondros T. G. "The continuous crack flexibility model for crack identification" Blackwell Science Ltd., fatigue fact matter 24, pp. 643-650, 2001.

[7]   Cam Ertugrul, SadettinOrhan and Murat Luy "An analysis of cracked structure using impact echo method", Elsevier journal, NDT&E International 38 (2005) 368–373.

[8]   Alexander Tessler, Marco Di Sciuva and Marco Gherlone, "Refinement of Timoshenko Beam Theory for Composite and Sandwich Beams Using Zigzag Kinematics" paper of NASA, NASA/TP-2007-215086.

[9]   Lin-Tai Tang, "Cracked Beam and Related Singularity problems", master thesis, National Sun Yat-sen University, Taiwan, July 1, 2001.

[10] H. R. Oz and M. T. Das, "In-Plane Vibrationsof Circular Curved Beamswitha Transverse Open Crack" Department of Mechanical Engineering, University of Gaziantep, 27310, Gaziantep,Turkey, Mathematical and Computational Applications, Vol. 11, No. 1, pp. 1-10, 2006.

[11] D.S rinivasarao, K.MallikarjunaRao and G.V.Raju, "Crack identification on a beam by vibration measurements and wavelet analysis ", International Journal of Engineering Science and Technology, Vol. 2(5), 2010, 907-912.

[12] S. S. Rao 'Mechanical Vibrations' Addison-Wesley Publishing Company, (1995).

[13] Krawczuk, M., Zak, A., and Ostachowicz, W. "Dynamics of Cracked Composite Material Structures," Comput. Mech., 20, pp. 79–83, 1997.

[14] Birman, V., and Simitses, G. J. "Vibration of Sandwich Panels and Beams With Matrix Cracks in the Facings," Compos. Sci. Technol., 61, pp. 1605–1613, 2001.

[15] Kisa, M. "Free Vibration Analysis of a Cantilever Composite Beam with Multiple Cracks", Composites Science and Technology, Vol. 64, 1391–1402, 2004.

[16] Robert L. Norton "Machine Design" Pearson Education, Inc., 2006.

دراسة تحليلية وعددية لتأثير الشق على التردد الطبيعي للعتبات ذات التثبيط البسيط

لؤي صادق محمد   مهند لفتة الوائلي   علي محمد حسين

قسم الهندسة الميكانيكية/ كلية الهندسة/ جامعة الكوفة

الخلاصة

تم في هذا البحث دراسة تأثير الشقوق على التردد الطبيعي للعتبات الجاسئة بحرية حيث تم دراسة تأثير موقع وعمق الشق عل التردد الطبيعي للعتبة وذلك بطريقة عملية ،وتحليلية ،وعددية باستخدام برنامج (ANSYS). وتم مقارنة النتائج مع بعضها البعض لعتبة مصنوعة من الفولاذ بابعاد(طول*عرض *سمك =0.02*0.02*0.84) وخواص (E=200Gpa) وكثافة (ρ=7680kg/m^3).تم مقارنة النتائج المستحصلة من برنامج ANSYS حيث وجد اكبر نسبة خطا هي ٧.٢ % لموقع شق (٤٢سم) وعمق (٦مم)، وتمت كذلك مقارنة النتائج المستحصلة من طريقة رايلي والعملي. و وجد اكبر نسبة خطا هي ٦.٢ % لموقع شق (٤٢سم) وعمق (٦مم). من قيم نسب الخطأ يمكن الاستنتاج ان طريقة رايلي تعطي نتائج اقرب للعملي من طريقة ANSYS. وكذلك وجد أن تردد العتبة عندما يكون الشق في منتصفها اقل من تردد العتبة عندما يكون الشق بالقرب من أطرافها.

Extraction of Penicillin V from Simulated Fermentation Broth by Liquid-Liquid Membrane Technique

Khalid W. Hameed

Department of Biochemical Engineering/Al-Khwarizmi College of Engineering/University of Baghdad
Email:Kwhameed74@yahoo.com

Abstract

Liquid-liquid membrane extraction technique, pertraction, using three types of solvents (methyl isobutyl ketone, n-butyl acetate, and n-amyl acetate) was used for recovery of penicillin V from simulated fermentation broth under various operating conditions of pH value (4-6) for feed and (6-8) for receiver phase, time (0-40 min), and agitation speed (300-500 rpm) in a batch laboratory unit system. The optimum conditions for extraction were at pH of 4 for feed, and 8 for receiver phase, rotation speed of 500 rpm, time of 40 min, and solvent of MIBK as membrane, where more than 98% of penicillin was extracted.

Keywords: Liquid-liquid membrane, Penicillin V, pertraction, extraction.

1. Introduction

Liquid-liquid membranes extraction technique combines extraction and stripping into one step, rather than the two separate steps required in conventional processes such as solvent extractions. A one-step liquid membrane process provides the maximum driving force for the separation of a targeted species, leading to the best clean-up and recovery of the species[1]. Liquid membrane process, called also pertraction process, have gained increased attention due to its ambient temperature operation, relatively low capital cost, high separation efficiencies and modular construction. The process is inherently low-energy, continuous, and can be made highly-automated. The amount of organic solvent required are generally very small, and thus the technology is environmentally benign[2, 3]. Two aqueous solutions, feed solution F, and receiver solution R, are separated by a third, organic liquid M, representing the "liquid membrane" which is insoluble in the other two liquids. The solute is transferred from the feed to the acceptor solution under the effect of appropriately chosen equilibrium conditions at the two interface F/M and M/R. In liquid membranes, facilitated transport is the mass transfer mechanism for the target species to go from the feed solution to the receiver solution.[4, 5]. Extraction using liquid membranes has been studied since the 1980s and is one of the most advantageous techniques of separation at the present. This separation method consists in the transfer of a solute between two aqueous phases of different pH which are separated by a solvent and carrier layer. The claimed advantages are as follows: the quantity of solvent used is small because of its continuous regeneration, the loss of solvent is small during extraction process provided the pH gradient between the two aqueous phases is maintained, there is a possibility of solute transport through liquid membranes that have been used for the separation of some biosynthetic products, namely carboxylic acids, amino acids and antibiotics[6, 7].The membrane interposed between two miscible aqueous solution, at one side (feed phase) in which the solute to be transport is extracted, while at the other side (strip phase), re-extraction occurs. Since in each of the aqueous phase some specific, and different for each of them, thermodynamic conditions exist, the extraction and re-extraction occur simultaneously[8, 9].

The steps of transport of solute in the pertraction system are described as: diffusion through the boundary layer in the feed solution, sorption on the feed solution/liquid membrane interface, diffusion through boundary layer on the feed side, transport in the membrane, diffusion through boundary layer on the receiving side, desorption on the membrane/receiving solution interface and diffusion through the boundary layer in the receiving solution [10].

The incessant stripping of solute of the liquid membrane keeps low concentration of solute in this phase and therefore provides its complete recovery from the feed solution. One of the principal advantages of pertraction process is the practically complete removal of the valuable component from the source material using, in most cases, not sophisticated, friendly solvents, in particular-water. As far as the membrane liquid is considered, it is noteworthy to mention that the requirements to the liquid membrane are not the same as to the conventional solvents used in a solvent extraction process, because in pertraction, priority is given to the membrane selectivity, rather than to the capacity and the solute distribution coefficient [11].

Penicillin V is a secondary metabolite produced at low growth rates and its syntheses have been described extensively in the literature. Penicillin formation starts from three activated amino acids, and involves several enzymes and isopenicillin N as a major intermediate. Penicillin V (phenoxymethylpenicillin) is the commercially most important penicillin. It is mainly converted to 6-aminopenicillanic acid (6-APA), which in turn is used to make amoxicillin and ampicillin. Penicillin V is a weak acid and it is extracted with n-butyl acetate at pH 2-3. In this pH range penicillin V is unstable and decomposes, therefore the aqueous medium in fermentation broth is cooled to $0^{o}C$ and extracted in centrifugal extractor to keep contact time as short as possible [12].

In the present work the fermentation broth was simulated by dissolving penicillin V sodium salt in distilled water. Liquid-liquid pertraction technique was conducted for the recovery of penicillin V in a batch pertraction laboratory unit. Methyl isobutyl ketone (MIBK), n-amyl acetate, and n-butyl acetate were proposed as membranes for penicillin V pertaction at $25^{o}C$. The effect of speed of agitation, time, and pH were studied.

2. Experimental Work

2.1. Material

Feed Phase (Donor Phase):

The feed phase was prepared by dissolving 1 g of penicillin V sodium salt in 1 L of distilled water, the pH of solution is adjusted by [4% H_2SO_4 (BDH)] and [5% Na_2CO_3 (BDH)] [6].

Receiver Phase (Stripping Phase):

A sodium carbonate solution was used as a receiver phase.
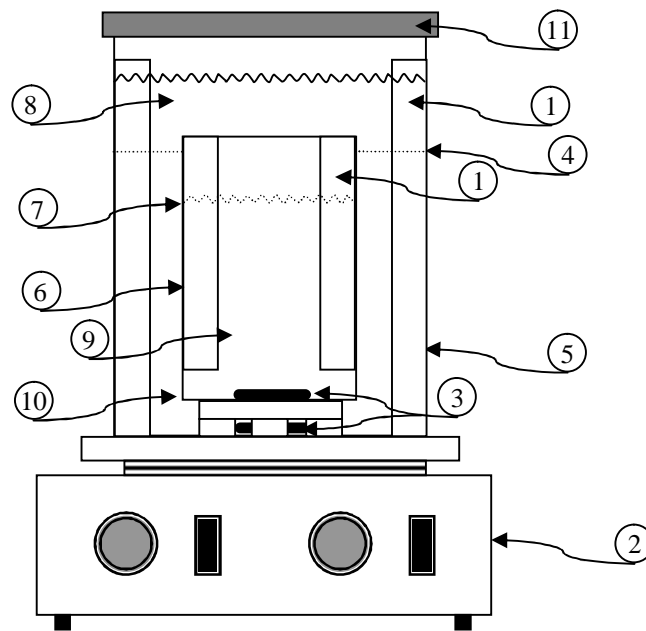
Membrane Phase:

In the present study, methyl isobutyl ketone (BDH), n-amyl acetate (BDH), and n-butyl acetate (BDH) were used as liquid membrane.

2.2. Pertraction Lab Unit

Pertraction experiments were carried out in 1 liter laboratory pertractor as shown in Fig. 1. The pertractor consists of two coaxial Pyrex beakers and baffles where placed in each beaker as shown in Fig. 1. The outer beaker is 1 liter and the inner is 250 ml. The two beakers were arranged as shown in Fig. 1 and placed on a magnetic stirrer with heater in order to control the temperature and the speed. The membrane, feed, and receiver phases were stirred by using two Teflon-coated magnetic bars.

2.3. Experimental Setup

500 ml of feed phase was placed in the annular space between the two beakers, and 200 ml of receiver phase was placed in the inner beaker. After that 300 ml of membrane phase was added to cover the other two phases as shown in Fig.1. The outer beaker was covered with a thin plastic layer to prevent evaporation of membrane phase. In the present study the effect of speed of agitation using the three proposed membranes was studied in the range of 300-500 rpm. The speed of agitation and temperature were adjusted and controlled by using hotplate and magnetic stirrer. The pertraction time was continuing up to 40 min and during this period of time samples were taken at a specified time interval from the feed and receiver phases for penicillin V analysis by HPLC. HPLC type Shimadzu model LC20AD was used in this analysis using column 100 RP-18 (5 μm). The penicillin V in the membrane organic phase was evaluated by material balance.

1	Baffles	7	Membrane-Receiver interface
2	Magnetic Stirrer	8	Membrane phase
3	Magnetic bars	9	Receiver phase
4	Membrane-Feed interface	10	Feed Phase
5	Feed-baker	11	Plastic cover
6	Receiver Baker		

Fig. 1.Schematic Diagram of Pertraction Laboratory Unit.

3. Results and Discussion

In the present work, the batch pertraction of penicillin V using the three proposed liquid membranes was studied, the agitation speed, and liquid membrane type was conducted in this work. The efficiency of penicillin V extracted, *E*, was calculated as follows:

$$E = \frac{C_r V_r}{C_{fo} V_f} \times 100\% \qquad \ldots(1)$$

Where C_r is the penicillin V concentration in the receiver phase, C_{fo} is the initial concentration in the feed phase, V_r is the volume of receiver phase, and V_f is the volume of feed phase.

3.1. Effect of pH

Figures 2 and 3 show the relationship between the penicillin transport from feed and to the receiver phases respectively with pH at different liquids membrane and at agitation speed of 400 rpm and time of extraction of 40 min. The range of pH for feed phase is taken between (4-6) and for receiver phase between (6-8) because the penicillin V is unstable and decomposes for pH < 4 and pH > 8[13]. From Figure 2, it can be seen that the extraction of penicillin V from feed is increasing with the decrease of pH value and also from Figure 3 the extraction of penicillin V by the receiver is increasing by increasing of pH value because the over all mass transfer coefficient increases when the difference in the pH value between two phases is high as possible[14]. In the Figure 2, it seems that the best value of pH for extraction of penicillin V from feed is 4 where about 98% of penicillin V is extracted by MIBK, while from Figure 3, the best value of pH for extraction of penicillin V by the receiver phase is 8 although the pH value of 7.5 has little effect on the extraction.
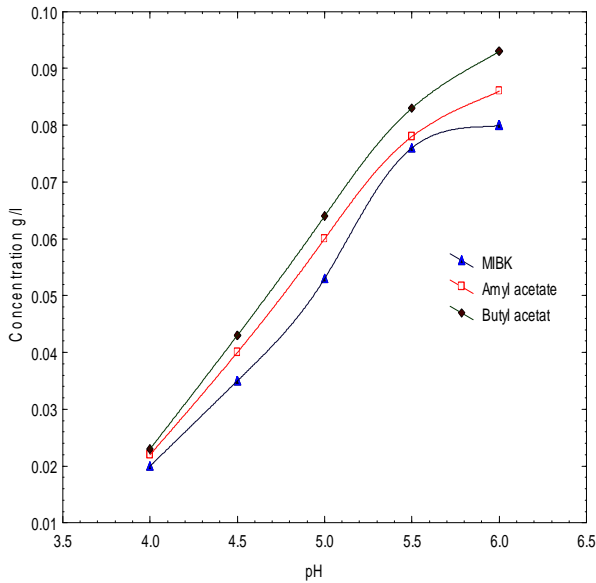
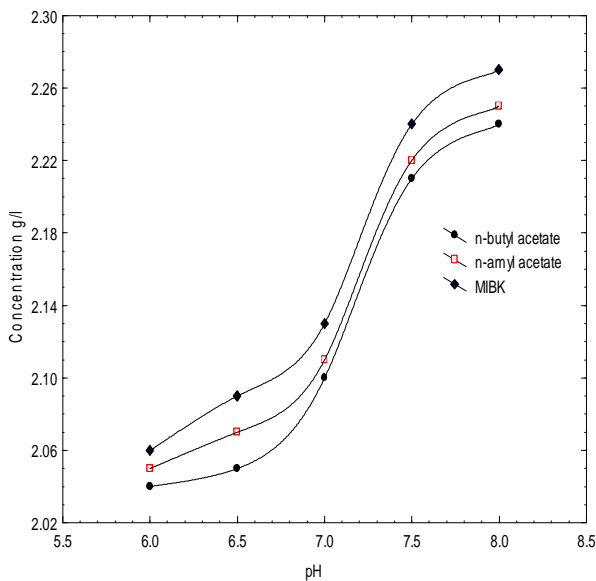**Fig. 2. pH Effect on Penicillin Extraction from Feed Phase after 40 min and Agitation Speed of 400 rpm.**

Fig. 3. pH Effect on Penicillin Extraction by Stripping Phase after 40 min and Agitation Speed of 400 rpm.

3.2. Effect of Membrane type

From figures 2 and 3, it can be seen that is a better solvent as a membrane and it can give better extraction efficiency methyl isobutyl ketone (MIBK) with respect to other solvents (n-amyl acetate and n-butyl acetate). The extraction efficiency of penicillin V is evaluated by using equation 1 for three types of membranes at

temperature of 25°C, rotation speed of 400 rpm and pH for feed 4 and for receiver phase 8 as shown in Table 1, where the difference in extraction efficiency for three types of membrane are very little; i.e., the effect of membrane type on extraction is little.

Table 1,
Extraction Efficiency, *E*, of Penicillin V for 3 Types of Membrane at 25°C, 400 rpm and pH of Feed 4 and of Receiver 8.

Membrane type	*E*
MIBK	90.8
n-amyl acetate	90
n-butyl acetate	89.6

Figure 4 shows the penicillin V content in the feed ($R_f = \dfrac{C_f}{C_{fo}}$), membrane, MIBK, ($R_m = \dfrac{C_m}{C_{fo}}$) and receiver phases ($R_r = \dfrac{C_r}{C_{fo}}$) during the extraction at temperature of 25°C, agitation speed of 400 rpm and pH of 4 for feed and 8 for receiver phases. It seems that about 80% of penicillin V is extracted during 15 min; i.e., the extraction process during this time is fast, while after 30 min the extraction is stable and there is no effect of time on extraction.
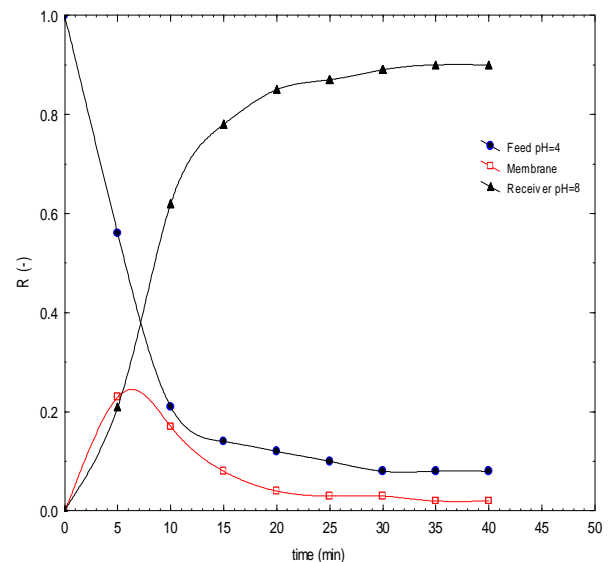

Fig. 4. Penicillin V Content in Feed, Membrane (MIBK), and Receiver Phases with Time at 25°C and 400 rpm .

3.2. Effect of Agitation Speed

Figure 5 shows the effect of speed of agitation on the extraction efficiency, *E*. In order to explore the effects of stirring rate, the extraction experiment were carried out at three different stirring rates, 300, 400, and 500 rpm. *E* value increases with increasing speed of agitation, which means that the extraction efficiency of penicillin V from feed phase to the receiver phase through liquid membrane improved with increasing the speed of agitation; this is because the higher stirring rate leads to much severer mixing between the aqueous solution and organic phase, which could accelerate the transport of penicillin V and enhance the mass transfer area between the aqueous solution and liquid membrane solution and reduce the mass transfer resistances of penicillin V from feed to liquid membrane in the extraction process, and from liquid membrane to the receiver phase in the stripping process. This variation in the efficiency indicates a diffusion control of the extraction process. According to previously published literature, although the mass transfer improved with higher speed of agitation, it was not applied because of increased risk of droplet formation which causes phase intermixing and deterioration of the process [10].
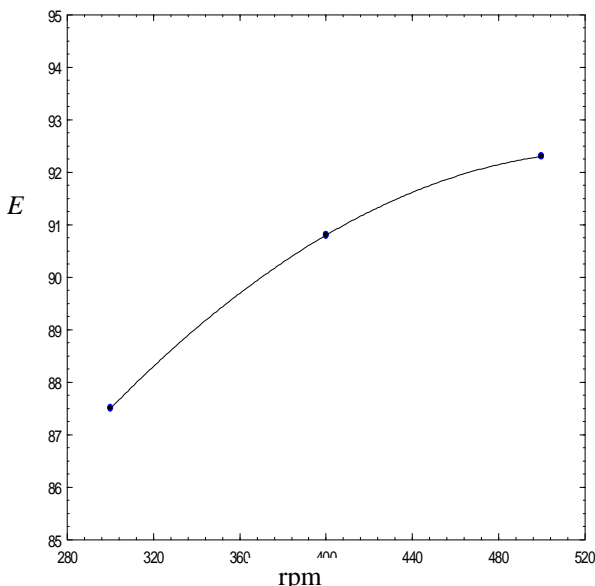

Fig. 5. Effect of Rotation Speed on the Extraction Efficiency Using MIBK as Membrane, at 25°C, and pH of 4 for Feed and 8 for Receiver Phases.

4. Conclusion

The liquid-liquid membrane extraction, pertraction, of biosynthetic products constitutes advantageous alternatives to conventional separation methods because it reduces the number of stages required for an efficient separation and, therefore, for the corresponding energy and material consumption. It can be concluded that the separation of Penicillin V from simulated broth could be enhanced by decreasing the pH value for feed up to 4 and increasing pH value up to 8 for receiver phase and increasing rotation speed up to 500 rpm. The type of solvent as a membrane has little effect on the extraction efficiency.

5. Reference

[1] James N. Parker, M.D. and Philip M. Parker, Penicillin, 2004, "A medical Dictionary, Bibliography", and Annotation Research Guide to internet References, copyright by Icon group international, Inc.

[2] Bradley D. Smith et al, 1998, "Facilitated of transport of carbohydrates, catecholamines, and amino acids though liquid and plasticized organic membranes", Journal of inclusion phenomena and molecular recognition in chemistry 32: 121-131.

[3] Mona M. Naima, Abir A. Monir, 2002, "Desalination using supported liquid membranes", Desalination 153, 361–369.

[4] Norman N. Li, Anthony G. Fane, W. S. Winston Ho, and T. Matsuura, 2008, "Advance membrane Technology and Application", John Wiley & Sons.

[5] Anil K. Pabby, Syed S. H. Rizvi, Ana Maria Sastre, 2009, "Handbook of membrane separation", Taylor & Francis Group.

[6] Cascavala D., Oniscua C., Cascavalb C., 2000, "Selective separation of penicillin V from phenoxyacetic acid using liquid membranes" , Biochemical Engineering Journal 5, 45-50.

[7] Zainuddin Abdul Manan, Mohamed Mahmoud Nasef, and Siti Hamidah Mohd, 2007, "Advances in separation process", First edition.

[8] Richard W. Baker, 2004, "Membrane Technology and applications", John Willy and Sons. 2nd Ed.

[9] Kamniski W., 2000, "Applicability of liquid membrane in the environmental protection",

Polish Journal of environmental studies Vol. 9, No. 1, 37-43.

[10] Boyadzhiev L., K. Dimitrov, D. Metcheva, 2006, "Integration of solvent extraction and liquid membrane separation: An efficient tool for recovery of bio-active substances from botantial", Elsevier 20 March.

[11] Nabil N. Ahmed Al-Hadithi, 2007, "Determination of drug and metabolites in the water by use of liquid membrane systems and HPLC-Method development and application" M.Sc. in Chemistry, Al-Anbar-Iraq.

[12] Elmar Heinzle, Arno P. Biwer, and Charles L. Coony, 2006, "Development of Sustainable Bioprocesses Modeling and Assessment", Copyright John Wiley & Sons Ltd.

[13] Benedict, RG., Schmidt, WH., Coghill, RD., Oleson, AP.(1945) "The stability of penicillin in aqueous solution", J. Bact. 49: 85-95.

[14] Kheirolomoon A., Sayfkordi A. A., Kazemi-Vaysari A., Ardjmand M., and Baradar-Khoshfetrat A. July 2001, "Mass transfer analysis of penicillin extraction", Scientia Iranica vol. 8, No. 3 PP 179-184.

استخلاص البنسلين V من ناتج التخمير المصطنع بأستخدام تقنية الغشاء السائل

خالد وليد حميد

قسم الهندسة الكيميائية الإحيائية/ كلية الهندسة الخوارزمي/ جامعة بغداد

البريد الالكتروني:Kwhameed74@yahoo.com

الخلاصة

تم استخدام تقنية الأستخلاص بطريقة الغشاء السائل لثلاث انواع من المذيبات العضوية (ايزوبيوتايل مثل كيتون، اسيتات البيوتايل الأعتيادي، اسيتات الأمايل الأعتيادي) والتي أستخدمت لغرض استخلاص البنسيلين V من ناتج التخمير المصطنع تحت ظروف تشغيل متباينة من اس هيدروجيني بمدى (٤-٦) للقيم و (٦-٨) للطور المستلم، زمن استخلاص بمدى (٠-٤٠ دقيقة)، وسرعة خلط بمدى (٣٠٠-٥٠٠ دورة/دقيقة) في منظومة مختبرية ذات النظام الدفعي. الظروف المثلى للأستخلاص كانت عند اس هيدروجيني ٤ للقيم و ٨ للطور المستلم، سرعة خلط ٥٠٠ دورة/دقيقة، زمن استخلاص ٤٠ دقيقة وللمذيب العضوي ايزوبيوتايل مثل كيتون، حيث اكثر من ٩٨% من البنسلين تم استخلاصه ضمن هذه الظروف.

Restrained Edges Effect on the Dynamics of Thermoelastic Plates under Different End Conditions

Wael R. Abdul-Majeed*   Muhsin J. Jweeg**   Adnan N. Jameel***

Department of Mechatronics Engineering/Al-Khawarizmi College of Engineering/ University of Baghdad
** College of Engineering/University of Al-Nahrain*
*** Department of Mechanical Engineering/College of Engineering/University of Baghdad*

Abstract

Frequency equations for rectangular plate model with and without the thermoelastic effect for the cases are: all edges are simply supported, all edges are clamped and two opposite edges are clamped others are simply supported. These were obtained through direct method for simply supported ends using Hamilton's principle with minimizing Ritz method to total energy (strain and kinetic) for the rest of the boundary conditions. The effect of restraining edges on the frequency and mode shape has been considered. Distributions temperatures have been considered as a uniform temperature the effect of developed thermal stresses due to restrictions of ends conditions on vibration characteristics of a plate with different will be investigated. it is noticed that the thermal stress will increase with increasing the heatnig temperature and that will cause the natural frequency to be decreased for all types of end conditions and for all modes of frequency.

Keywords: Thermoelasticity, thin plate, ends condition, mode shape, natural frequency.

1. Introduction

Thermoelasticity is concerned with questions of equilibrium of bodies treated as thermodynamic systems whose interaction with the environment is confined to mechanical work, external forces, and heat exchange. Because of constraints, a non -uniform temperature distribution in a component having a complex shape usually gives rise to thermal stresses. It is essential to know the magnitude and effect of these thermal stresses when carrying out on rigorous design of such components. The thermal stresses alone and in combination with the mechanical stresses produced by the external forces will be effect on dynamics properties of apart such as natural frequency and mode shape . Naji, et al. [1] studied the thermal stresses generated within a rapidly heated thin metal plate when a parabolic two-step heat conduction equation is used.

The effect of different design parameters on the thermal and stress behavior of the plate is investigated. Al-Huniti, et al. [2] investigated the thermally induced vibration in a thin plate under a thermal excitation .The excitation is in the form of a suddenly applied laser pulse (thermal shock). The resulting transient variations of temperature are predicted using the wave heat conduction model (hyperbolic model), which accounts for the phase lag between the heat flux and the temperature gradient. The resulting heat conduction equation is solved semi analytically using the Laplace transformation and the Riemann sum approximation to calculate the temperature distribution within the plate. The equation of motion of the plate is solved numerically using the finite difference technique to calculate the transient variations in deflections. Norris and Photiadis [3] enabled direct calculation of thermoelastic damping in vibrating elastic solids.

The mechanism for energy loss is thermal diffusion caused by inhomogeneous deformation, flexure in thin plates. The general result is combined with the Kirchhoff assumption to obtain a new equation for the flexural vibration of thin

plates incorporating thermoelastic loss as a damping term. The thermal relaxation loss is inhomogeneous and depends upon the local state of vibrating flexure, specifically, the principal curvatures at a given point on the plate. The influence of modal curvature on the thermoelastic damping is described through a modal participation factor. The effect of transverse thermal diffusion on plane wave propagation is also examined. It is shown that transverse diffusion effects are always small provided the plate thickness. Tran a,   et al. [4] studied the thermally induced vibration and its control for thin isotropic and laminated composite plates. The structural intensity (SI) pattern of the plates which have different material orientations and boundary conditions was analyzed. The thermoelasticity simulation is performed using the finite element method. It shows that the structural energy flows are dependent on the material structures as well as the boundary conditions for a prescribed thermal source. The position to attach a damper for controlling the thermally induced vibration is investigated based on the virtual sources and sinks of the SI patterns.

2. Analytical Study

The plate analyzed has usually been assumed to be composed of a single homogeneous and isotropic material with shape and dimensions as in Fig. (1) [5].
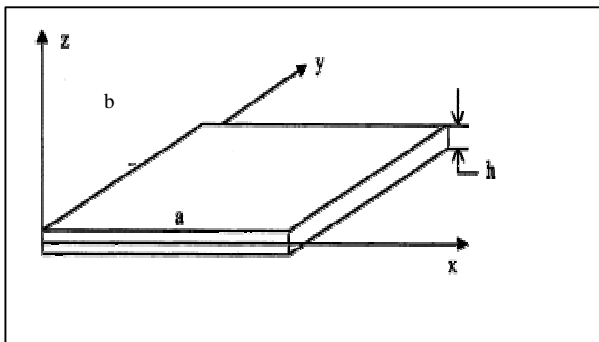

Fig. 1.Schematic Diagram of Thin Plate.

3. Boundary Conditions

General closed – form solutions are given   of a thermoelastic rectangular   plate with various elementary boundary conditions on each of the four edges. Appendix A collect some important combinations of end boundary conditions. [Let the plate be placed in a coordinate system with the origin at it center and the edge width (a) be parallel to x – axis and and the edge width (b) be parallel to y as in Fig. (1)

4. Natural Frequency and Mode Shape of dynamic Thermoelastic plates

Free,   transverse   vibrations   of   the thermoelastic structural with neglecting the effect of in plane vibrations are studied with different end   boundary   conditions   under   uniform temperature distribuation.

4.1. All Edges are Simply Supported

The general governing differential equation of free vibration of thermoelastic plate is represented by [6]:

$$D\nabla^4 w = rh\ddot{w} - \frac{\nabla^2 M_t}{1-u} + N_x \frac{\partial^2 w}{\partial x^2} + N_y \frac{\partial^2 w}{\partial y^2} + 2N_{xy} \frac{\partial^2 w}{\partial x \partial y}$$
$$\ldots(1)$$

Where $D = \dfrac{Eh^3}{12(1-u^2)}$,   and the quantities

$$N_t = aE \int_{-h/2}^{h/2} (\Delta T) dz$$

$$M_t = aE \int_{-h/2}^{h/2} (\Delta T) z dz \qquad \ldots(2)$$

Which represents the thermal stress resultants .

Then the boundary conditions for the deflection w are represented in   Appendix C

$$w_{x=0} = w_{x=a} = 0 \qquad , \qquad w_{y=0} = w_{y=b} = 0$$

$$\frac{\partial^2 w_{x=0}}{\partial x^2} = \frac{\partial^2 w_{x=a}}{\partial x^2} = 0 \qquad , \qquad \frac{\partial^2 w_{y=0}}{\partial y^2} = \frac{\partial^2 w_{y=b}}{\partial y^2} = 0$$

The initial conditions assuming the plate initially at rest in the refrence position ,are given by

$$w(x, y, 0) = \frac{\partial w}{\partial t}(x, y, 0) = 0 \qquad 0 \le x \le a ,$$
$$0 \le y \le b \qquad \ldots(3)$$

The   displacement   function $w(x, y, t)$ is approximated by means of the expansion [7].

$$w(x, y, t) \approx w(x, y) \sin w_{mn} t =$$

$$\sin wt \sum_{m=1}^{\infty} \sum_{n=1}^{\infty} w_{mn} \sin \frac{mpx}{a} \sin \frac{npy}{b} \qquad \ldots(4)$$

And the displacement function $w(x, y)$ is assumed from functions, that satisfies identically the boundary conditions; these functions are different due to the types of end conditions at x and y axis and this will be studied .

The plate will have uniform temperature

$$\Delta T = T_c \qquad \ldots(5)$$

substitution of Eq.(5) in Eq. (2) we have

$$N_t = aEhT_c \qquad M_t = 0 \qquad \ldots(6)$$

So that for all edges are restrained

$$N_x = N_y = -\frac{N_t}{1-u} \qquad N_{xy} = 0 \qquad \ldots(7)$$

with all edges are ***restrained*** ,substituting the thermal forces in Eq. (7) and the deflection from Eq. (4) into the governing differential equation of free vibration of thermoelastic plate in Eq.(1) noting that $Mt = 0$, one obtains the following frequency equation.

$$Dp^4 \left[\left(\frac{m}{a}\right)^2 + \left(\frac{n}{b}\right)^2 \right]^2 - \frac{N_t p^2}{1-v} \left[\left(\frac{m}{a}\right)^2 + \left(\frac{n}{b}\right)^2 \right] = rhw_{mn}^2$$
$$\ldots(8)$$

for natuaral frequancy of plate without thermal load $N_t = 0$

$$w_{mnf}^2 = \frac{Dp^4}{rha^4} \left[m^2 + r^2 n^2 \right]^2 \qquad \ldots(9)$$

Then

$$w_{mn}^2 = w_{mnf}^2 - \frac{N_t p^2}{rh(1-v)a^2}(m^2 + r^2 n^2) \qquad \ldots(10)$$

Substituting Eq. (7) into Eq. (10) , the natuaral frequancy as a function of uniform temperature T_c can be presented as

$$w_{mn}^2 = w_{mnf}^2 - \frac{aET_c p^2}{rh(1-v)a^2}(m^2 + r^2 n^2) \qquad \ldots(11)$$

And for *restrained* edges at x=0,a and *unrestrained* at y=0,b thermal forces will be

$$N_x = -\frac{N_t}{1-u} \qquad N_{xy} = N_Y = 0 \qquad \ldots(12)$$

and the natuaral frequancy will be

$$w_{mn}^2 = w_{mnf}^2 - \frac{N_t m^2}{rh(1-v)a^2} \qquad \ldots(13)$$

and the function of the uniform temperature T_c will be

$$w_{mn}^2 = w_{mnf}^2 - \frac{aET_c p^2 m^2}{r(1-v)a^2} \qquad \ldots(14)$$

4.2. All Edges are Clamped

To derive the differential equation for lateral vibration of rectangular thermoelastic plate a kinetic energy of the plate in edition to the total strain energy of the plate and apply the Hamilton's principle to derive the equation of motion. The kinetic energy due to the velocity $\dot{w}$ only is represented as

$$T = \frac{1}{2} \iint_A rh\dot{w}^2 dxdy \qquad \ldots(15)$$

the Hamilton's principle for the plate undergoing small deflection can be set as [8]:

$$d \int_{t1}^{t2} (T - \Pi_{strain}) dt = 0 \qquad \ldots(16)$$

Then the lagrangian of the plate from the above equation can be written as

$$L = \frac{1}{2} \iint_A D\left(\frac{\partial^2 w}{\partial x^2} + \frac{\partial^2 w}{\partial y^2}\right)^2 dxdy - \frac{1}{2} \iint_A \left\{ N_x \left(\frac{\partial w}{\partial x}\right)^2 \right.$$
$$+ N_y \left(\frac{\partial w}{\partial y}\right)^2 + 2N_{xy}\left(\frac{\partial w}{\partial x}\right)\left(\frac{\partial w}{\partial y}\right) \right\} dxdy$$
$$+ \iint_A \frac{M_t}{1-v}\left(\frac{\partial^2 w}{\partial x^2} + \frac{\partial^2 w}{\partial y^2}\right) dxdy - \frac{1}{2} \iint_R rh\dot{w}^2 dxdy$$
$$\ldots(17)$$

For free vibration the solution is assumed

$$w(x, y, t) = \sum_{i=1}^{m} \sum_{j=1}^{n} A_{ij} X_i(x) Y_j(y) \sin wt \qquad \ldots(18)$$

Substituting Eq. (18) by Eq. (19) and minimizing the resulting lagrangian with respect to A_{ij} ,we get

$$\sum_{k=1}^{m}\sum_{j=1}^{n}\left[\begin{array}{l}D\int_{0}^{a}\int_{0}^{b}\left((X'')^2Y^2+2X''XY''Y+X^2(Y'')^2\right)dxdy\\-\int_{0}^{a}\int_{0}^{b}\left(N_x(X')^2Y^2+N_yX^2(Y')^2+2N_{xy}XX'YY'\right)dxdy\end{array}\right]A_{ij}+\sum_{i=1}^{m}\sum_{j=1}^{n}\frac{M_t}{(1-v)}\int_{0}^{a}\int_{0}^{b}(X''Y+XY'')dxdy=\sum\sum\left[rhw^2\int_{0}^{a}\int_{0}^{b}X^2Y^2dxdy\right]A_{ij}\quad\ldots(20)$$

This is the general frequency equation**.**

   With uniform temperature T_c and all edges are *restrained* with the aid of Eq. (2) for thermal

forces and thermal moments into general frequency equation we have:

$$w^2=\frac{D\int_{0}^{a}\int_{0}^{b}\left((X'')^2Y^2+2X''XY''Y+X^2(Y'')^2\right)dxdy+\frac{N_t}{(1-v)}\int_{0}^{a}\int_{0}^{b}\left((X')^2Y^2+X^2(Y')^2\right)dxdy}{rh\int_{0}^{a}\int_{0}^{b}X^2Y^2dxdy}\quad\ldots(21)$$

 The frequency of plate without thermal effect has the form

$$w_{iif}^2=\frac{D\int_{0}^{a}\int_{0}^{b}\left((X'')^2Y^2+2X''XY''Y+X^2(Y'')^2\right)dxdy}{rh\int_{0}^{a}\int_{0}^{b}X^2Y^2dxdy}$$
$$\ldots(22)$$

Then with substituting the mode shape of clamped ends X_i and Y_j from Appendix C

$$w_{ij}^2=w_{iif}^2-\frac{N_t\left(a_1^2+r^2a_3^2\right)}{rha^2(1-v)}\qquad\ldots(23)$$

With w_{iif} for free vibration of clamped plate

$$w_{iif}^2=\frac{D\left(a_1^4+2r^2a_2+r^4a_3^4\right)}{rha^4}\qquad\ldots(24)$$

Then w_{ij} terms of uniform temperature will be as:

$$w_{ij}^2=w_{iif}^2-\frac{aET_c\left(a_1^2+r^2a_3^2\right)}{ra^2(1-v)}\qquad\ldots(25)$$

Where a_1,a_2 and a_3 are calculated from Appendix C
For clamped edges *restraind* at x=0,a and *unrestrained* at y=0,b

$$w_{ij}^2=w_{iif}^2-\frac{N_ta_1^2}{rha^2(1-v)}\qquad\ldots(26)$$

In terms of temperature

$$w_{ij}^2=w_{iif}^2-\frac{aET_ca_1^2}{ra^2(1-v)}\qquad\ldots(27)$$

4.3. Edges are Clamped at x=0,a and Simply Supported at y=0,b

   The general frequency equation of clamped edges Eq. (20) are suitable for edges clamped at x=0,a and simply supported at y=0,b. With uniform temperature T_c and all edges *restrained* with the aid of Eq. (2) for thermal forces and thermal moments into general frequency equation and arranged with substituting the mode shape of two clamped ends and two simply supported ends X_i and Y_j from Appendix C into above equations the result will be

$$w_{ij}^2=w_{iif}^2-\frac{N_t\left(b_1^2+r^2b_3^2\right)}{rha^2(1-v)}\qquad\ldots(28)$$

With w_{iif} for free vibration suitable for edges clamped at x=0,a and simply supported at y=0,b .

$$w_{iif}^2=\frac{D\left(b_1^4+2r^2b_2+r^4b_3^4\right)}{rha^4}\qquad\ldots(29)$$

Then w_{ij} in terms of uniform temperature will be:

$$w_{ij}^2=w_{iif}^2-\frac{aET_c\left(b_1^2+r^2b_3^2\right)}{ra^2(1-v)}\qquad\ldots(30)$$

Where b_1,b_2 and b_3 calculated from Appendix C
For clamped edges *restraind* at x=0,a and simply supported *unrestrained* at y=0,b

$$w_{ij}^2=w_{iif}^2-\frac{N_tb_1^2}{rha^2(1-v)}\qquad\ldots(31)$$

In terms of temperature

$$w_{ij}^{2} = w_{iif}^{2} - \frac{aET_c b_1^2}{ra^2(1-v)} \qquad \ldots(32)$$

5. Results and Discussions

The sample of calculations was made on Aluminum 1060-H18 rectangular plate which has the mechanical and thermal properties given in appendix A respectively. Rectangular plate with three aspect ratio a/b (r = 1.2). and a/h (j =120) and owing constant magnitude of a=0.12 m has been considered. The effects of the uniform increase of temperature of plates (thermoelastic behavior) on the natural frequency and mode shapes with different three types of ends conditions have been studied.

Figures (2), (3) and (4) show the effect of temperature rising on natural frequencies analytical magnitudes till it reaches the thermal buckling temperature for plates with all edges restrained. The types are SSSS, CCCC and CSCS respectively

It is observed that the lowest natural frequencies of all types reach zero when the

temperatures get to the thermal buckling temperature; also the first five natural frequencies of plates decreas with increasing the temperature. Second and third natural frequencies of CSCS plate have the same magnitudes almost.

Figures (5), (6) and (7) show the effect of temperature rising on natural frequencies analytical magnitudes till it reaches the thermal buckling temperature for plates with edges at x=0,a restrained the types are SSSS, CCCC and CSCS respectively

The lowest natural frequencies of all types reach zero when the temperatures has the thermal buckling temperature. The first five natural frequencies of plates decrease with increasing the temperature.

The fifth natural frequency of SSSS plate will become the fourth natural frequency and vice versa when the temperature has magnitude close to 6 C^0. Also CCCC natural frequencies have the same behavior of SSSS type but they are switching at magnitude close to 3 C^0.

CSCS natural frequencies have the switching behavior between second and third natural frequencies at magnitude close to 1 C^0.
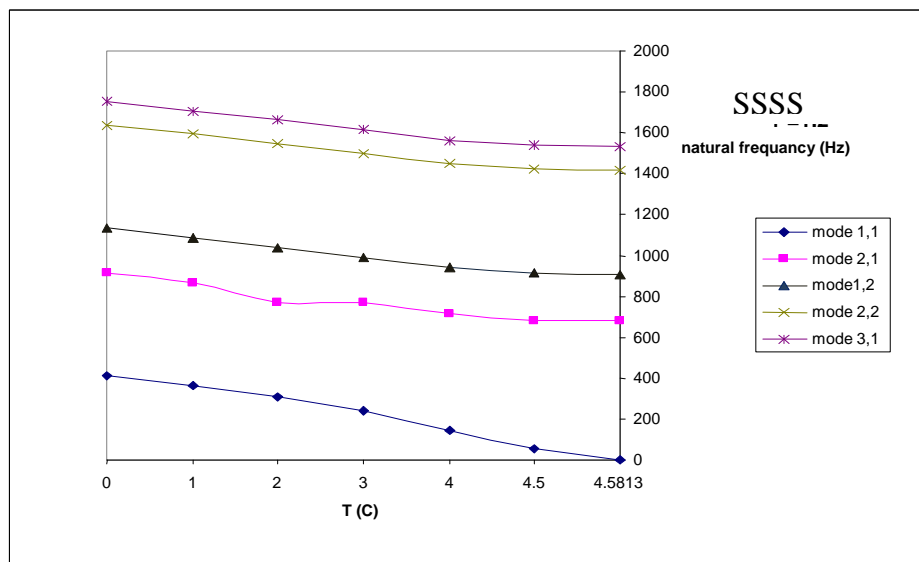

Fig. 2. Effect of Temperature on First Five Natural Frequencies Magnitude on SSSS Plate, All Edges are Restrained.
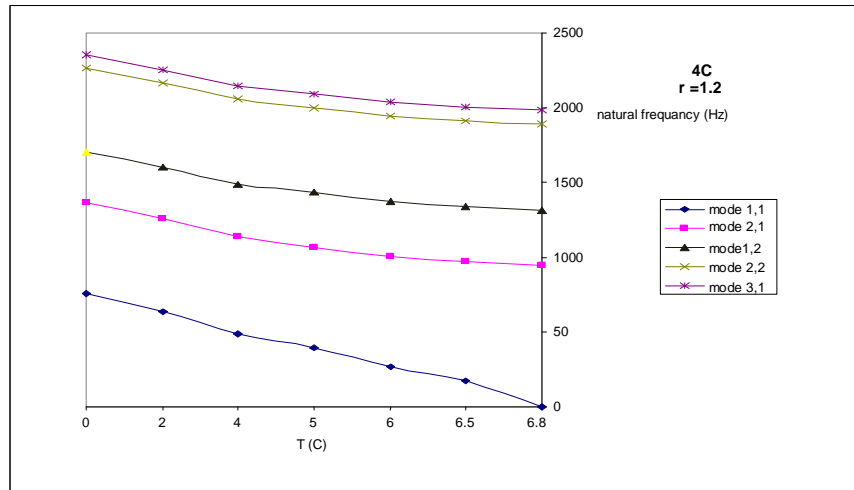
Fig. 3. Effect of Temperature on First Five Natural Frequencies Magnitude on CCCC Plate with All Edges are Restrained.
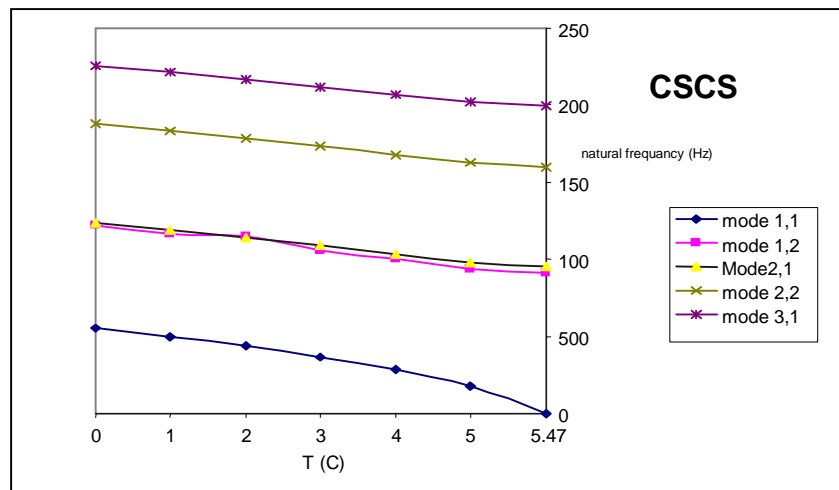

Fig. 4.Effect of Temperature on First Five Natural Frequencies Magnitude on CSCS Plate, All Edges is Restrained.
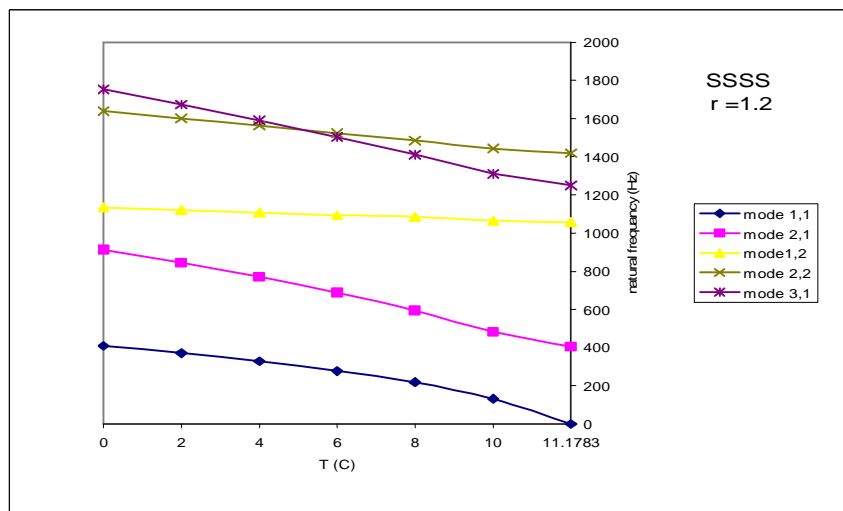

Fig. 5.Effect of Temperature on First Five Natural Frequencies Magnitude on SSSS Plate, Edges at y=0, b are Unrestrained.
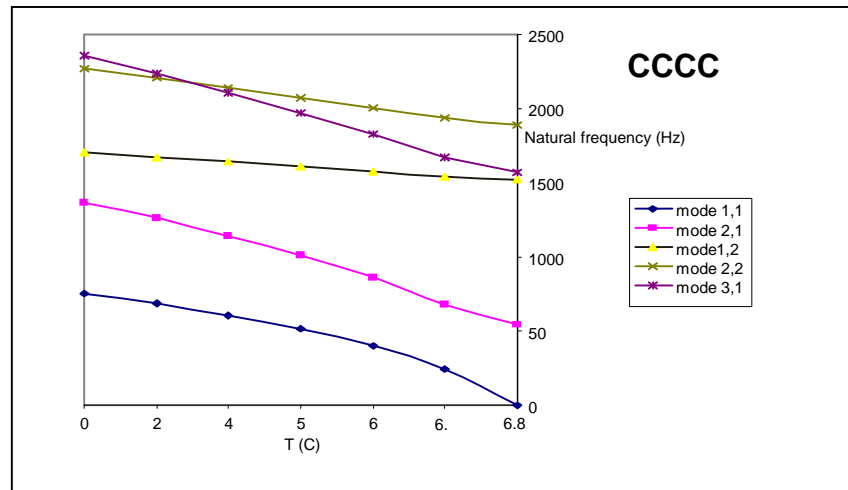
Fig. 6.Effect of temperature on First Five Natural Frequencies Magnitude on CCCC Plate, Edges at y=0, b are Unrestrained.
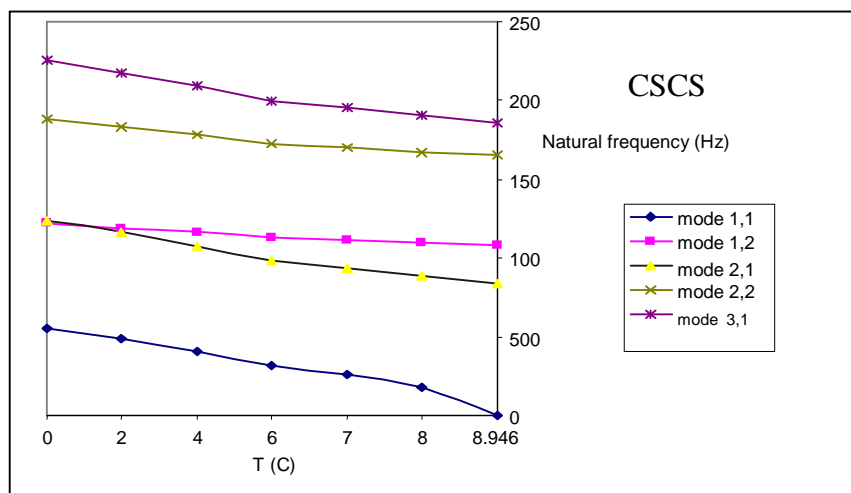

Fig. 7. Effect of Temperature on First Five Natural Frequencies Magnitude on CSCS Plate, Edges at y=0, b are Unrestrained.

6. Conclusions

The following are the main summarized conclusions of this paper:
1. Thermal stresses have a significant influence on the natural frequency for the free boundary conditions compared with clamped boundaries, so that the boundary condition is one of the important factors that influence the vibration and mode shapes.
2. The lowest natural frequencies of all types reach zero when the temperatures has the thermal buckling temperature
3. The first five natural frequencies of plates decreasing with increasing of the uniform temperature of the plates for all types of ends conditions

4. In the case of the two opposite edges which are unrestrained, there is a switching between the modes of natural frequency when the temperature increases for each type of ends conditions.

Nomenclature

Latin Symbols

A	Area (mm^2)
a, b	Plate side length (mm)
D	Flexural rigidity of an isotropic plate (N.mm*)*
E	Modulus of elasticity of isotropic material (N/mm^2)

h	Plate thickness (mm)
i ,j	Integer
Mt	Thermal bending moment (N.m)
m,n	Integer
Nx, Ny	Edge forces per unit length (N/m)
Nxy	Shearing forces per unit length (N/m)
Nt	Thermal forces per unit length (N/m)
r	Dimensional aspect ratio a/b (m/m)
T	Temperature (C^0), Kinetic energy of the element (J)
t	Time (sec)
x, y, z	Cartesian coordinates

Greek Symbols

a_m, b_n	Coefficients
n	Poisson's ratio
r	Mass density (Kg/mm^3)
Π_{strain}	Strain energy stored in complete plate (J)
w_{iif}, w_{ij}	Angular frequency without and with thermal effect (rad/s)
j	Dimensional aspect ratio side / thickness (m/m)
a	Coefficient of thermal expansion ($1/C^0$)
w	Deflection (mm)

Abbreviations Symbols

CCCC	Clamped-Clamped-Clamped-Clamped
CSCS	Clamped-Simply-Clamped-Simply
SSSS	Simply-Simply-Simply-Simply
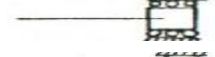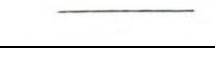
7. Refrences

[1] Malak Naji ,M. Al-Nimr and Naser S. Al-Huniti "THERMAL STRESSES IN A RAPIDLY HEATED PLATE USING THE PARABOLIC TWO-STEP HEAT CONDUCTION EQUATION " Journal of Thermal Stresses, 24:399-410, 2001 Taylor & Francis

[2] Naser S. Al-Huniti, M. A. Al-Nimr AND M. M. Meqdad "THERMALLY INDUCED VIBRATION IN A THIN PLATE UNDER THE WAVE HEAT CONDUCTION MODEL" Journal of Thermal Stresses, 26: 943–962, 2003 Taylor & Francis Inc

[3] A. N. Norris and D. M. Photiadis "Thermoelastic Relaxation in Elastic Structures, WITH Applications to Thin Plates" arXiv: cond-mat/0405323 v2 20 Nov 2004

[4] T.Q.N. Tran a, H.P. Lee a,b, and, S.P. Lim a "Structural intensity analysis of thin laminated composite plates subjected to thermally induced vibration" Composite Structures. Article in press.

[5] William L. Ko "Predictions of Thermal Buckling Strengths of Hypersonic Aircraft Sandwich Panels Using Minimum Potential Energy and Finite Element Methods ", NASA Technical Memorandum 4643, May 1995

[6] V. I. Kozolv "thermoelastic vibrations of arectangular plate" Pirk. Mekh. ,vol. 8, pp. 445-448, April 1972

[7] J. S. Rao, "DYNAMICS OF PLATES", Narosa Publishing House, 1999.

[8] A. W. Leissa, "recent research in plate VIBRATIONS", Complicating Effects ,Shock & Vib. Digest Vol. 19, No. 3, 1987 .

Appendices

Appendix A

Some Combinations of End Boundary Conditions

deflection	Mid-plane deformation	symbol
clamped	Restrained	
	unrestrained	
supported	restrained	
	unrestrained	
free	restrained	
	unrestrained	

Appendix B

Mechanical Properties of Aluminum 1060-H18

Density	2705 kg/m³
Hardness, Brinell	35
Ultimate Tensile Strength	27 MPa
Tensile Yield Strength	20 MPa
Elongation at Break	6 %
Modulus of Elasticity	69 GPa
Poisson's Ratio	0.3
Fatigue Strength	44.8 MPa
Machinability	30 %
Shear Modulus	26 GPa
Shear Strength	75.8 MPa

Thermal Properties of Aluminum 1060-H18

Heat Capacity	0.9 J/g °C
Thermal Conductivity	233 W/m °C
Coefficient of Thermal expansion	2.34e-5/°C
Convection Coefficient	2.5 W/m² °C

Appendix C

For SSSS ends condition

$$X_i = \sin m_i x \quad , \quad Y_j = \sin m_j y$$

$$w_{x=0} = w_{x=a} = 0 \quad , \quad w_{y=0} = w_{y=b} = 0 \quad , \quad \frac{\partial^2 w_{x=0}}{\partial x^2} = \frac{\partial^2 w_{x=a}}{\partial x^2} = 0 , \quad \frac{\partial^2 w_{y=0}}{\partial y^2} = \frac{\partial^2 w_{y=b}}{\partial y^2} = 0$$

For CCCC ends condition

$$X_i = \sin m_i x - \sinh m_i x - h_i(\cos m_i x - \cosh m_i x)$$
$$h_i = (\sin m_i a - \sinh m_i a)/(\cos m_i a - \cosh m_i a)$$
$$Y_j = \sin m_j y - \sinh m_j y - h_j(\cos m_j y - \cosh m_j y)$$
$$h_j = (\sin m_j b - \sinh m_j b)/(\cos m_j b - \cosh m_j b)$$
$$w_{x=0} = w_{x=a} = 0, \quad w_{y=0} = w_{y=b} = 0 \quad , \quad \frac{\partial w_{x=0}}{\partial x} = \frac{\partial w_{x=a}}{\partial x} = 0, \quad \frac{\partial w_{y=0}}{\partial y} = \frac{\partial w_{y=b}}{\partial y} = 0$$

For SCSC ends condition

$$X_i = \sin m_i x - \sinh m_i x - h_i(\cos m_i x - \cosh m_i x)$$
$$h_i = (\sin m_i a - \sinh m_i a)/(\cos m_i a - \cosh m_i a) \quad , \quad Y_j = \sin m_j y$$
$$w_{x=0} = w_{x=a} = 0 \quad , \quad w_{y=0} = w_{y=b} = 0 \quad , \quad \frac{\partial w_{x=0}}{\partial x} = \frac{\partial w_{x=a}}{\partial x} = 0, \quad \frac{\partial^2 w_{y=0}}{\partial y^2} = \frac{\partial^2 w_{y=b}}{\partial y^2} = 0$$

Where $m_i a$ and $m_j b$ are the roots of the above equations

The roots of SSSS ends condition are

$$m_i = \frac{mp}{a} \quad , \quad m_i = \frac{np}{b}$$

The roots of CCCC ends condition are

$$a_1 = a_3 = 4.73$$
$$a_2 = 151.3$$
For i=1 , j=1
$$a_1 = 4.73$$
$$a_3 = (j+0.5)p$$
$$a_2 = 123a_3(a_3-2)$$
For i=1 , j=2,3,4,….

$$a_1 = (i+0.5)p$$
$$a_3 = 4.37$$
$$a_2 = 12.3a_1(a_1-2)$$
For i=2,3,4,… j=1
$$a_1 = (i+0.5)p$$
$$a_3 = (j+0.5)p$$
$$a_2 = a_1(a_1-2)a_3(a_3-2)$$
For i=2,3,4,. j=2,3,4,….\

$$a_1 = (i+0.5)p$$
$$a_3 = (j+0.5)p$$
$$a_2 = a_1(a_1-2)a_3(a_3-2)$$
For i=2,3,4,. j=2,3,4,….

The roots of CSCS ends condition are

$$b_1 = 4.73$$
$$b_3 = jp$$
$$b_2 = 12.3 j^2 p^2$$
For i=1 , j=1, 2, 3,..
$$b_1 = (i+0.5)p$$
$$b_3 = jp$$
$$b_2 = a_1(a_1-2)j^2 p^2$$
For i=2,3,4,… j=1,2,3….

تاثير الحافات المحددة من الحركة على ديناميكية الصفائح المرنة حراريا تحت ظروف نهايات مختلفة

وائل رشيد عبد المجيد*   **محسن جبر جويج****   **عدنان ناجي جميل*****

*قسم هندسة الميكاترونكس/ كلية الهندسة الخوارزمي/ جامعة بغداد

**كلية الهندسة / جامعة النهرين

***قسم الهندسة الميكانيكية/ كلية الهندسة/ جامعة بغداد

الخلاصة

صيغ معادلة التردد الطبيعي لصفائح مستطيلة الشكل مع وبدون تاثير المرونة الحرارية لحالات النهايات التالية: كل النهايات ذات اسناد بسيط ، كل النهايات مثبتة ، و نهايتين متقابلتين باسناد بسيط ونهايتين مثبتتين تم ايجادها من خلال الحل بالطريقة المباشرة للنهايات باسناد بسيط ، وباستخدام مباديء هاملتون والتخفيض بطريقة رتز للطاقة الكلية لباقي انواع النهايات . تاثير تثبيت النهايات افقيا بوجود درجة حرارة منظمة التوزيع على الترددات الطبيعية وشكل التردد تم دراستها كما تم التعرف على تاثير تولد الاجهادات الحرارية الناتجة من تثبيت النهايات افقيا على خواص الاهتزازات وتم ملاحظة ان الاجهادات الحرارية المتولدة تزداد مع ازدياد درجة حرارة التسخين وهذا يودي الى نقصان في الترددات الطبيعية لكل انواع النهايات ولكل اشكال الترددات الطبيعية.

The Stability Conditions of the Pump Structure Vibration

Nassir Hassan Abdul Hussain Al Hariri

Department of Machines and Equipment/Instate of Technology-Baghdad

Abstract

The general approach of this research is to assume that the small nonlinearity can be separated from the linear part of the equation of motion. The effect of the dynamic fluid force on the pump structure system is considered vibrates at its natural frequency but the amplitude is determined by the initial conditions. If the motion of the system tends to increase the energy of the pump structure system, the vibration amplitude will increase and the pump structure system is considered to be unstable. A suitable MATLAB program was used to predict the stability conditions of the pump structure vibration. The present research focuses on fluid pump problems, namely, the role played by damping coefficient C, damping factor D and angular speed ω (termed the ratio $(\frac{W}{W_n})$) and the determining stability of a centrifugal pump structure. The data demonstrate substantial rotor dynamic effects, a destabilizing chart appears to be inversely proportional to the D, C, and ω, and resonance changes significantly with flow rate.

Keyword: Stability, Amplitude, Vibration, Resonance, Pump.

1. Introduction

Because of the complex spectra behavior of pump structure system it is not easy to interpret the results of pressure or velocity measurements of such systems [1]. The pump vibration comes from several sources that include mechanical causes of vibration, i.e. unbalanced rotating components, damaged impellers and non concentric shaft sleeves are common, non-laminar flow and operating the pump at a critical speed [2]. Frequencies below running speed can be caused by acoustical resonance. Generally these effects are due to the impeller passing and discharge diffuser [3]. Able to originate internally or externally, an excitation force is the only cause of vibration. Repeating forces create the vibration problems most commonly associated with centrifugal pump. These forces are often caused by the rotation of imbalanced, misaligned, or worn pump components [4]. However, in real structures the energy input by the flow has a finite limit, because the fluid forces on the structure are limited. Thus the amplitude of unstable region can only grow until it is limited by nonlinearities in the structure itself [5]. Resonance can be avoided by changing a systems' frequency, which is determined by the mass, stiffness and damping properties of all of the components involved, including the pump, base, motor, piping-coupling, guard, foundation, etc. If the resonance vibration is just below the natural frequency, the stiffness of the system should be increased so the vibration frequency shifts above the natural frequency. If the resonance vibration is just above the natural frequency, the systems' mass should be increased, shifting the vibration frequency below the natural frequency [6]. Many vibration problems are results of interactions among a system pump, motor, fluid, piping and structure. This requires systems approach to vibration analysis, rather than the investigation of individual components [7]. A nonlinear system could have more than one equilibrium, some of which may be stable and others unstable as it is clearly noticed in the stability charts of the pump structure vibration[8].

2. Theory

The investigated equation of motion of the model pump structure in y-axis [9] is:

$$m\ddot{y} + (C - 3K_v) \dot{y} + Ky = F_f \qquad \dots(1)$$

Let $\quad a = \dfrac{C}{m} = \dfrac{2mwD}{m} \quad$ and $\quad b = K/m$

$$\ddot{y} + a \dot{y} + b\, y - \frac{F_f}{m} = 0 \qquad \dots(2)$$

To solve Eq. (2) ,a particular solution is assumed as:

$$y = Y \sin (\omega t)$$

Substituting Eq. (2) as:

$$- \omega^2 Y \sin (\omega t) + a \omega Y \cos (\omega t) + b Y \sin (\omega t) - \frac{F_f}{m} = 0 \qquad \dots(3)$$

The stable and unstable regions of equation (3) depends on the parameters **a** and **b** and are shown in the charts of stability condition of the pump structure system.

Substituting and rearranging Eq. (3), the parameter **b** becomes**:**

$$b = \frac{F_f}{Y.m.\sin(wt)} + \omega^2 - a\,\omega \cot (\omega t) \qquad \dots(4)$$

Substituting the values and after modifying and neglecting the small values of Eq.(1) the amplitude of the oscillating motion of the pump is obtained [9]:

$$Y = \frac{F_f}{K\sqrt{[1-(\frac{w}{w_n})^2]^2 + [2D(\frac{w}{w_n})^2]^2}} \qquad \dots(5)$$

By substituting values Y and $K = m. \omega^2$ and substituting Eq. (5) in Eq. (4) as:

$$b = \frac{\sqrt{[1-(\frac{w}{w_n})^2]^2 + [2D(\frac{w}{w_n})^2]^2}}{\sin(wt)} + 1 - \frac{a}{w}\cot(wt) \qquad \dots(6)$$

The conditions of stability of the pump structure are given by the roots **a** and **b** as:

b > 0 stability is increased
b < 0 instability is increased
a > 0 always and pump structure system is stable

Equation (6) is known as the Mathieus equation [10].

The stable and unstable regions of Eq.(6) depends on the parameters **a** and **b** and are shown in the stability charts obtained. There are no known closed form solutions to the nonlinear differential equations describing the response of the pump structure used in an oscillating flow. It is possible to numerically integrate these nonlinear equations to obtain a solution.

At resonance ω = ω_n

If the frequency of the oscillating flow is much greater than the natural angular frequency of the structure, then the pump structure; becomes intensive to high frequency forces that energy in to the pump structure and cannot be transfer the response approaches zero [11].
Therefore the parameter **b** in Eq.(6) becomes:

$$b = \frac{\sqrt{2.D}}{\sin w_n} + 1 - \frac{a}{m.w_n} \cot (\omega_n t) \qquad \dots(7)$$

The parameter **b** will be positive or negative depending actually upon the time of oscillating **t** and on the damping factor **D**.

The MATLAB program is used to solve the equation of motion (6) to get the stability charts. And reach the following assumptions:

$$r = (\frac{w}{w_n})^2$$

$$M = [\, 1 - (\frac{w}{w_n})^2 \,]^2$$

$$M = [\, 1 - r \,]^2$$

$$S = [\, 2. D. (\frac{w}{w_n})^2 \,]^2$$

$$S = [\, 2. D. r \,]^2$$

$$N = \sqrt{[1-(\frac{w}{w_n})^2]^2 + [2D(\frac{w}{w_n})^2]^2}$$

$$N = \sqrt{M + S}$$

Substituting these values in Eq.(6) as:

$$b = \frac{N}{\sin(wt)} + 1 - (\frac{a}{w}) \cot (\omega t)$$

MATLAB Program

>> % We will now get Stability Condition at ω= 112

>> t= 0.001;0.002;0.003;0.004;0.005;0.006;0.007;0.008;0.009;0.012;0.016;0.020;

>> r = 0.221;0.307;0.469;0.623;0.854;1;112;1.44;1.74;1.94;2.175; 2.509;

>> D = 0.01;0.06;0.10;0.15;0.25;0.35;0.40;0.55;0.65;0.75;0.85;0.95;

>> a = 2 * ω * D;

>> a

>> M = (1-r)^2

>> M

>> S = (2*D*r)^2

>> S

>> N = sqrt (M+S)

>> N

>> b= N/sin(ω *t)+1-(a/ ω)*cot(ω *t)

>> b

To draw the stability charts of the pump structure at different values of times, ratios of angular speeds with natural speed and damping factors, the MATLAB program was used:

>> % We will give variables for plot at ω= 112
>> a=[2.24; 13.4; 22; 33; 56; 78; 89; 123; 145; 168; 190; 212];
>> b=[7.79; 3.98; 2.79; 2.18; 1.68; 1.39; 1.32; 1.16; 1.161; 1.52; 2.26; 3.63];
>> % We will plot
>> plot (a,b,'-ob','LineWidth',2,'MarkerSize',1)
>> xlabel('a')
>> ylabel('b')
>> title('\bf Stability Condition')

The MATLAB program of the stability condition at resonance state where

ω= ωn= 238 is:
r= 1
M= 0
>> % We will now get Stability Condition at resonance state ω=ωn=238
>> t = 0.001;0.002;0.003;0.004;0.005;0.006;0.007;0.008;0.009;0.012;0.016;0.020;
>> D = 0.01; 0.06; 0.1; 0.15; 0.25; 0.35; 0.40; 0.55; 0.65; 0.75; 0.85; 0.95;
>> a= 2* ωn * D;
>> S= (2*D)^2;
>> S
>> N= 2*D;

>> b= N/sin(238 *t)+1-(a/ 238)*cot(238*t);
>> b

The MATLAB program to plot the stability condition at ω= 132is:

%%WE will now give the variable for plot1 of stability chart at 0mega=132
a=[2.64;15;26;39;66;92;105;145;171;198;224;250];
b=[6.11;3.21;2.32;1.87;1.51;1.32;1.31;1.26;1.33;1.85;3.03;6.34];
%Now we will plot the plot1 of stability at omega=132
plot(a,b,'-ob','LineWidth',2,'MarkerSize',2)
% WE will give values for plot2 of experimental
a=[2.64;15;26;39;66;92;105;145;171;198;224;250];
b=[0;3;4.3;3.9;3.6;2.5;6.3;5.8;4.5;6.9;7.8;9.1];
% We will plot plot2 of experimental
% but we must use hold command to be able to show the the plot2 at the same window
hold on
plot(a,b,'--*r','LineWidth',2,'MarkerSize',2)
% We will give values for plot3 at resonance
a=[4.76;28;47;71;119;166;190;261;309;357;404;452];
b=[1;1.02;1.07;1.15;1.33;1.60;1.88;2.54;3.38;11;-3.9;-0.81];
%% We will plot for plot3 at resonance
plot(a,b,'-.+k','LineWidth',2,'MarkerSize',2)
xlabel('a')
ylabel('b')
legend('132','exp','res',0)

Displacement amplitudes are used at low vibration frequencies typically between (17-62) Hz. High displacement amplitudes at low frequencies can cause a considerable amount of stress damage to a pump structure. Using MATLAB program determined the stability conditions at angular speeds ω= [112, 132, 163, 188, 220, 238, 251, 286, 314, 332, 351, 377]. And MATLAB program was used also to plot the stability conditions of the pump structure at these angular speeds.

Fig.2.indicates the particular stability condition at angular speed ω=112. It has two small regions of stability and large area of instability. It is nearly similar to stability in Fig.3. in which it is at angular speed ω= 132 at the ratios of angular speeds (ω/ ωn)=(1/2.1 and 1/1.8).

3. Experimental method

The measurements method was tested on laboratory test instrument "Pumps Training System lab-volt". The photographic picture of the research experiment is shown in Fig.1. In the laboratory test, water is circulated from the water tank. The speed is measured by using an electro-magnetic flow meter. The static pressure is measured, relative to atmospheric pressure at the suction and discharge flanges of the pump. When operating the pump will act as an active element in the test loop . In this experiment pump induced pulsations are suppressed by coherence analysis with the external source signal as a reference. Measurements should be taken at operating speed for constant speed motor and at varying speeds for pump operating on variable speed drives [12].

Fig. 1. The Photographic Picture of the Research Experiment [9].

This research is carried out by using the type of centrifugal non-positive displacement, which has two kinds of openings; one opening is for flow- drag and the other opening is for flow-pushing. The drag opening is connected with fluid tank, and the pushing opening is joined with flow-meter to measure the fluid flow discharge. Then there is a valve for hindering the fluid flow which is coupled with its valve adjustment in parallel. The motor is linked with the pump, and the regulation is lying on the motor speeds by varying the frequencies. It takes the readings of the fluid flow discharge, and the pressure readings are

taken by the manometer. The readings of the vibration amplitudes of the pump structure are taken by the vibrometer, and the rpm of the propeller of the pump are also taking. The readings are shown in the Appendix of Table.1. and Table.2.

The value of the natural angular speed ω_n=238 is determined by using the Analyzer.

Table1,
The Measured Parameters of the Fluid Flow in the Pump [9].

Frequency F [Hz]	Angular speed ω [rad/s]	Vibration Amplitude RMS	Speed of Pump [rpm]
0	0	0	0
17.9	112	3	1029
21	132	4.3	1207
26	163	3.9	1495
30	188	3.6	1725
35	220	2.5	2012
38	238	6.3	2185
40	251	5.8	2300
45	283	4.5	2587
50	314	6.9	2875
55	345	7.8	3162
60	377	9.1	3450

Table2,
Shows the Measured and Calculated Parameters of the Pump Structure [9].

Total mass m [kg]	Measured mass m_o[kg]	Entrained mass m_f [kg]	Cross-sec. of pump A [m²]
7.2	1.2	6	0.00567

Stiffness of pump K [N.s/m]	Measured angular speed of pump ω_n [rad/s]	Width of pump B [m]	Diameter of pump d [m]
47203	238	0.0265	0.085

4. Results and Discussion

Figure (4) Shows the stability chart taking another form with small increasing in the zone of stability at angular speed ratio (1/1.26). Fig.5 the area of stability decreases to some values, then the curve increases sharply to some extent. In Fig.6. and Fig.7. show the stability charts reduce at angular speed ratios more than one, i.e. (ω/ω_n) = (1/0.94 and 1/0.75), they are very close to each others. It is concluded from the figures that the stability charts depend on the effect of the time of occurring of the vibration of the pump structure, in which parameter **b** plays the main role than the other parameters. It means that at the time occurring the amplitude of vibration at natural angular speed ω_n = 238 was higher than that of the lower angular speeds. However, it was predicted that the time of vibration amplitudes at lower frequencies were near zero values, which gave almost straight line at zero line of **b** parameter. The parameter **b** is playing a more important role than the values of **a** parameter at all values of the angular speeds, because the values of **a** parameter are always positive, while the values of **b** parameter are positive or negative values; they depend on the values of the times of vibration amplitudes.

The stability charts are obtained in the figures, by keeping natural angular speed ω_n and some other parameters are constants and then varying angular speed ω to vary the ratio ω/ω_n. It will be noticed actually, if the horizontal shaft is run at angular speed lower than natural angular speed ω_n = 238, then it will be instabilized at angular speeds 112, 132, and 163 which are nearly equal to half value of natural angular speed as shown in Figures 2, 3, and 4. In Figures 5, 6, and 8, the behavior of the stability charts are different at angular speeds 188, 220 and 251 because the stable areas were noticed evidently at negative **b** parameter, if the variable damping factor is assumed with constant value of the stiffness.

It is concluded also from the figures of stability charts, that the region between curves of theoretical stability charts at ω=(112 and 132) and of resonance chart at ω_n = 238 is called critical zone, which here it represented in small area. But at ω = (163, 188, 220, 251 and 286) critical zone coincides at the same line of each curve for certain extent of values of parameter **a** which is always positive. However, this means the system of the pump structure has the same critical limit. Then with th increasing the values of ω = (314, 332, 351 and 377) the possibility of the critical

zone begins to increase gradually for small area also at positive values of parameter **b**.

The ratio of error between the theoretical and experimental is between (0.2590 and 0.1403) for ω=(112 - 377).
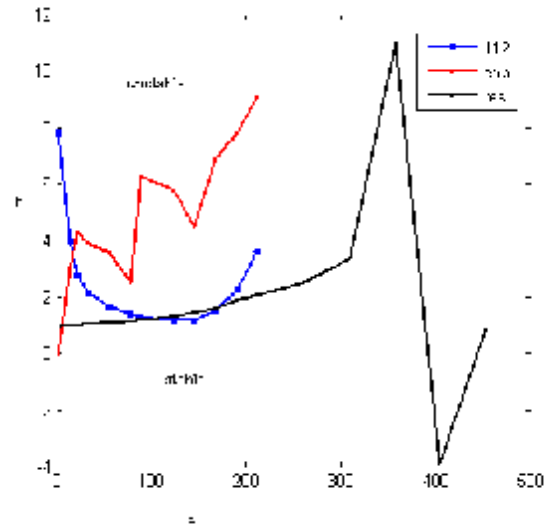

Fig. 2. Stability chart at ω= 112.

When blue line represents ω= 112 ,red line exp. represents experimental ,black line res. represents resonance.
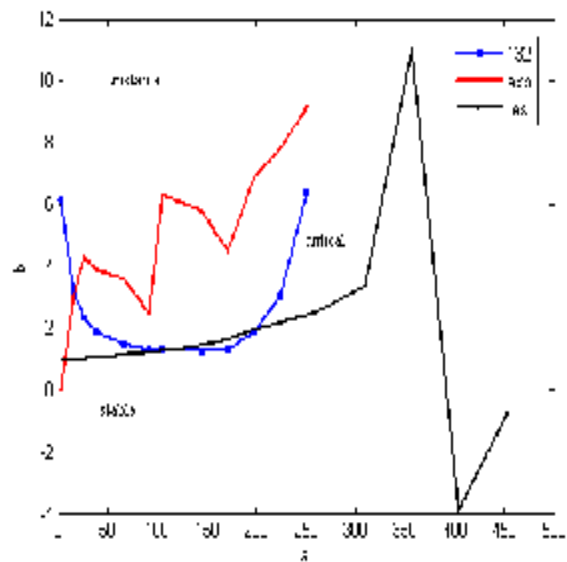

Fig. 3. Stability chart at ω= 132.

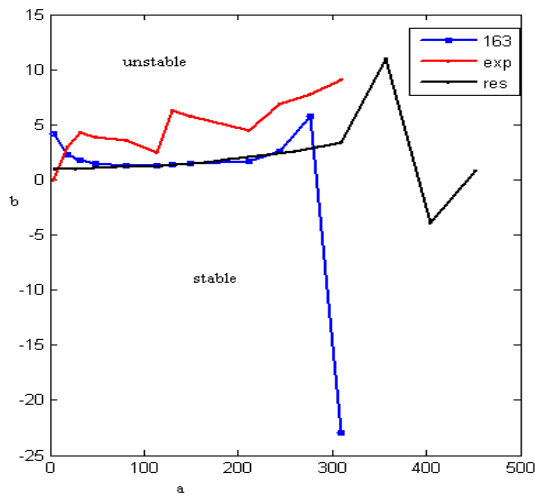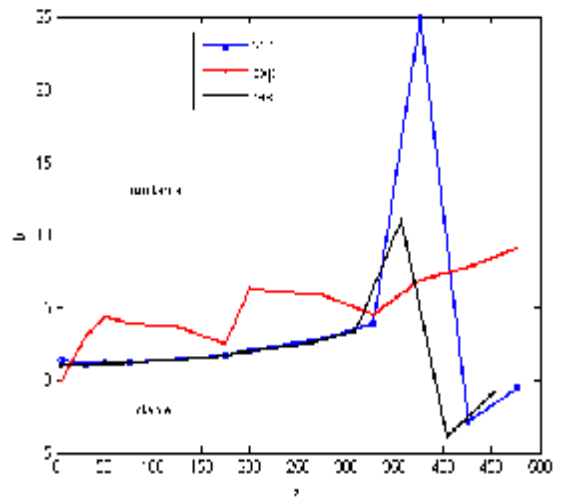**Fig. 4. Stability chart at ω= 163.**

Fig. 7. Stability chart at ω= 251.
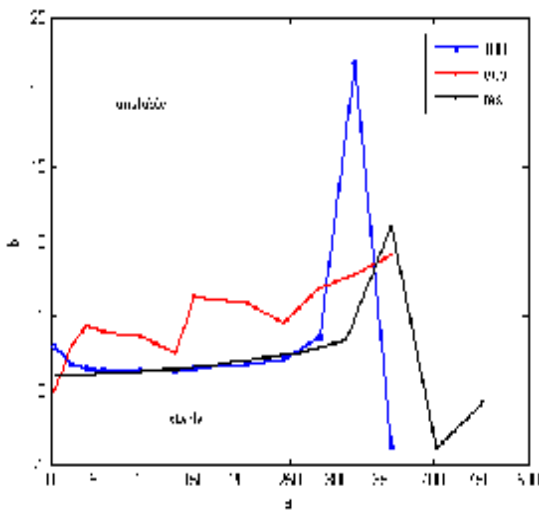
Fig. 5. Stability chart at ω= 188.
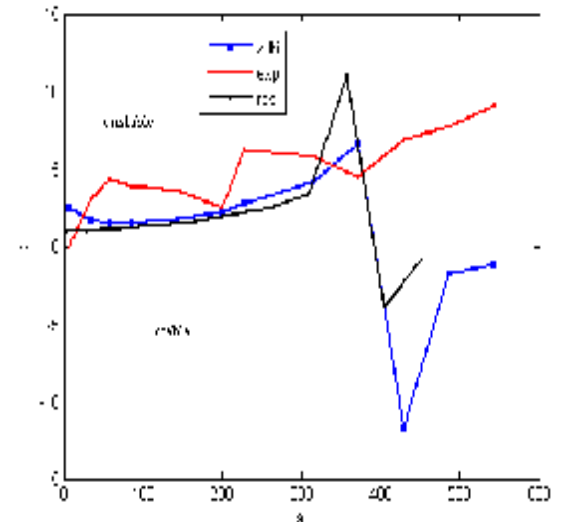
Fig. 8. Stability chart at ω= 286.
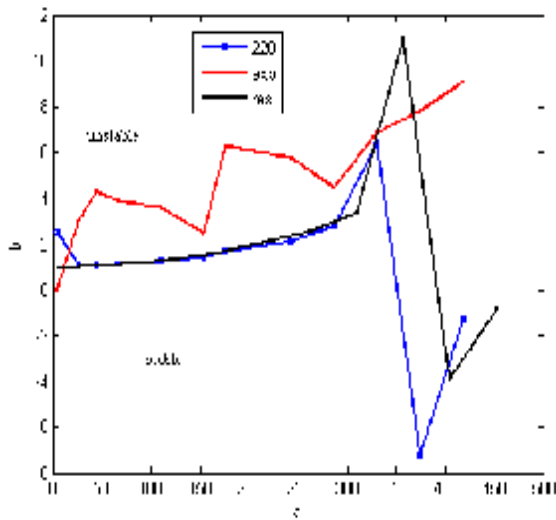
Fig. 6. Stability chart at ω= 220.
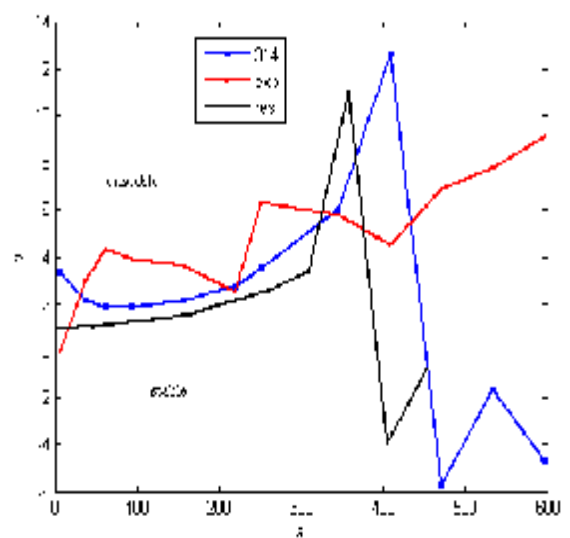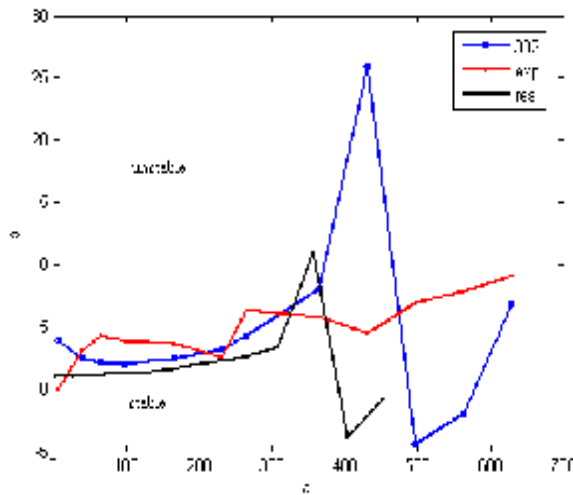

Fig. 9. Stability chart at ω= 314.
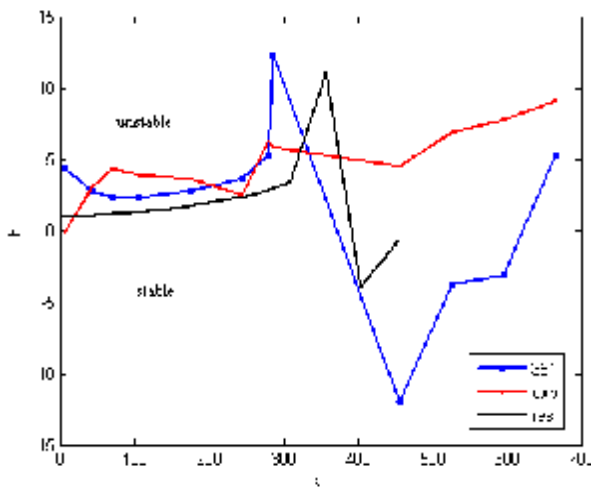
Fig. 10. Stability chart at ω= 332.
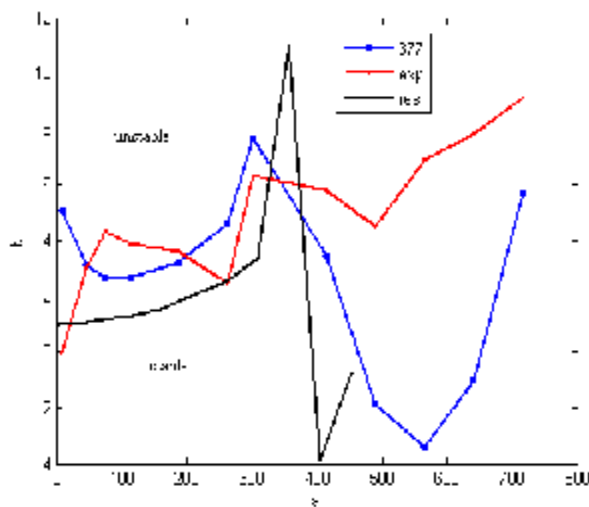

Fig.11. Stability chart at ω= 351.

Fig. 12. Stability chart at ω= 377.

5. Conclusions

From the results obtained the following conclusions can be withdrawn:

1- The stable and unstable regions of the equation of motion Eq.(6) depend on the parameters **a** and **b** which are shown in the stability charts figures.
2- Very small values for time of vibration amplitudes are required to get accepted results. If time **t** was not sufficiently small, the results would be very inaccurate.
3- The accuracy of the procedure increases as the value of the dynamic fluid force and damping forces decrease relative to the inertial and spring forces in the equation of motion.
4- Parameter **b** played a more important role than parameter **a** at values of angular speeds, naturally, because the parameter **b** depends on angular speeds, dynamic fluid force, damping factors and different values of time of vibration amplitudes.
5- It is noticed that the effect of pump structure damping is important near the ratio ω/ ω$_n$ which is between 0.45 and 1.58.
6- It is pointed out that a typical swirl velocity ratio at inlet (pump discharge) would be about 0.65 and may not be therefore large enough for the resonance to be manifest.

Nomenclature

m	total mass of the model pump structure [kg]
C	damping coefficient of the pump structure [N.s/m]
K$_v$	fluid force velocity coefficient [N.s/m]
K	stiffness of the pump structure [N/m]
F$_f$	total fluid force [N]
ω	measured angular speed of the pump [rad/s]
ω$_n$	natural angular speed of the blades of the model pump structure immersed in the fluid [rad/s]
f	frequency of the pump structure [Hz]
D	damping factor of the pump

6. References

[1] JONG CHRISTIAAN ARNOLDUS FRACISCUS DE, "Analysis of Pulsations and Vibrations in Fluid – Filled Pipe System", Eindhoven University of Technology, Thesis Eindhoven – ref. ISBN 90 – 386 – 0074 – 7, 1994.

[2] www.mcnallyinstitute.com.

[3] www.scribd.com.

[4] HPAC ENGINEERING, " Applications & Resources Pumping and Piping, Examining Causes of Pump Vibration", April 2009.

[5] FRANCES, TSE, IVAN MORSE & ROLLAND T. HINPLE, " Mechanical Vibrations Theory and Applications", Pub. ALLYN and Bacon, Sc. 1998.

[6] BILL WATTS and JOE VAN DYKE, " An Automated Vibration-Based Expert Diagnostic System", Sound & Vibration, Sept. 1993.

[7] http://en-wikipedia.org/wiki/pump.

[8] BILL WATTS, " Triaxial Vibration Spectral Data, An Important Ingredient for Proper Diagnosis", DLI Engineering, 253 Winslow Way West, Bainbridge Island, WA, 1998.

[9] NASSIR HASSAN ABDUL HUSSAIN, "The Effect of Fluid Force on The Pump Structure Vibrations", Second Scientific Conference of the College of Engineering-University of Al – Qadisiya, pp. 420-435, 19-20 Oct. 2009.

[10] WILLIAM F. THOMSON, " Vibration Theory and Application, George Alien and Anwin LTD, London, 1995.

[11] YOSHIDA, Y. , MURAKAMI, Y. , TSURUSAKI, T. AND TSUJIMOTO, Y. " Rotating Stalls in Centrifugal Impeller / Vaned Diffuser System", Proc. First ASME / JSME Joint Fluids Eng. Conf. , FED-107, 125-130, 1991.

[12] PUMP TRAINING SYSTEM LAB-VOLT, No. 4606, Work Orders-Instruc. 37894-20, USA, 2004.

حالة الإتزان لإهتزاز هياكل الضاغط

ناصر حسن عبد الحسين الحريري

قسم المكائن والمعدات/ معهد التكنولوجيا - بغداد

الخلاصة

لفهم الطريقة العامة للبحث فقد فرض قليل من الجزء الغير خطي بأن يفصل من الجزء الخطي لمعادلة الحركة. ولقد أخذت بنظر الإعتبار تأثيرات قوة السائل الديناميكية على نظام هيكل الضاغط، حيث أنه يهتز عند الذبذبات الطبيعية ولكن يحسب المدى من الشروط الأولية. إذا كان نظام الحركة يميل لزيادة الطاقة لنظام هيكل الضاغط، فسوف يزداد مدى الإهتزاز ويعتبر نظام هيكل الضاغط غير متزن. لقد أستخدم نظام MATLAB المناسب لتخمين حالة الإتزان لإهتزاز هيكل الضاغط. البحث الحالي يركز على مشاكل السائل للضاغط، إسميا للدور الحادث بواسطة معامل التخميد C، عامل التخميد D ،

والسرعة الزاوية (التي عبرت بالنسبة ($\dfrac{W}{W_n}$)) وكذلك في حساب الثباتية والصفة المميزة لهيكل الضاغط ذو الطرد المركزي. البيانات تظهر بوضوح التأثيرات الحقيقية للمحور الدوار الديناميكي، ومنحنيات عدم الإتزان تظهر العلاقة العكسية مع D, C, ω وكذلك الرنين يتغير بشكل كبير مع معدل الجريان.

Extraction of Penicillin V from Simulated Fermentation Broth by Liquid-Liquid Membrane Technique

Khalid W. Hameed

Department of Biochemical Engineering/Al-Khwarizmi College of Engineering/University of Baghdad
Email:Kwhameed74@yahoo.com

Abstract

Liquid-liquid membrane extraction technique, pertraction, using three types of solvents (methyl isobutyl ketone, n-butyl acetate, and n-amyl acetate) was used for recovery of penicillin V from simulated fermentation broth under various operating conditions of pH value (4-6) for feed and (6-8) for receiver phase, time (0-40 min), and agitation speed (300-500 rpm) in a batch laboratory unit system. The optimum conditions for extraction were at pH of 4 for feed, and 8 for receiver phase, rotation speed of 500 rpm, time of 40 min, and solvent of MIBK as membrane, where more than 98% of penicillin was extracted.

Keywords: *Liquid-liquid membrane, Penicillin V, pertraction, extraction.*

1. Introduction

Liquid-liquid membranes extraction technique combines extraction and stripping into one step, rather than the two separate steps required in conventional processes such as solvent extractions. A one-step liquid membrane process provides the maximum driving force for the separation of a targeted species, leading to the best clean-up and recovery of the species[1]. Liquid membrane process, called also pertraction process, have gained increased attention due to its ambient temperature operation, relatively low capital cost, high separation efficiencies and modular construction. The process is inherently low-energy, continuous, and can be made highly-automated. The amount of organic solvent required are generally very small, and thus the technology is environmentally benign[2, 3]. Two aqueous solutions, feed solution F, and receiver solution R, are separated by a third, organic liquid M, representing the "liquid membrane" which is insoluble in the other two liquids. The solute is transferred from the feed to the acceptor solution under the effect of appropriately chosen equilibrium conditions at the two interface F/M and M/R. In liquid membranes, facilitated transport is the mass transfer mechanism for the target species to go from the feed solution to the receiver solution.[4, 5]. Extraction using liquid membranes has been studied since the 1980s and is one of the most advantageous techniques of separation at the present. This separation method consists in the transfer of a solute between two aqueous phases of different pH which are separated by a solvent and carrier layer. The claimed advantages are as follows: the quantity of solvent used is small because of its continuous regeneration, the loss of solvent is small during extraction process provided the pH gradient between the two aqueous phases is maintained, there is a possibility of solute transport through liquid membranes that have been used for the separation of some biosynthetic products, namely carboxylic acids, amino acids and antibiotics[6, 7].The membrane interposed between two miscible aqueous solution, at one side (feed phase) in which the solute to be transport is extracted, while at the other side (strip phase), re-extraction occurs. Since in each of the aqueous phase some specific, and different for each of them, thermodynamic conditions exist, the extraction and re-extraction occur simultaneously[8, 9].

The steps of transport of solute in the pertraction system are described as: diffusion through the boundary layer in the feed solution, sorption on the feed solution/liquid membrane interface, diffusion through boundary layer on the feed side, transport in the membrane, diffusion through boundary layer on the receiving side, desorption on the membrane/receiving solution interface and diffusion through the boundary layer in the receiving solution [10].

The incessant stripping of solute of the liquid membrane keeps low concentration of solute in this phase and therefore provides its complete recovery from the feed solution. One of the principal advantages of pertraction process is the practically complete removal of the valuable component from the source material using, in most cases, not sophisticated, friendly solvents, in particular-water. As far as the membrane liquid is considered, it is noteworthy to mention that the requirements to the liquid membrane are not the same as to the conventional solvents used in a solvent extraction process, because in pertraction, priority is given to the membrane selectivity, rather than to the capacity and the solute distribution coefficient [11].

Penicillin V is a secondary metabolite produced at low growth rates and its syntheses have been described extensively in the literature. Penicillin formation starts from three activated amino acids, and involves several enzymes and isopenicillin N as a major intermediate. Penicillin V (phenoxymethylpenicillin) is the commercially most important penicillin. It is mainly converted to 6-aminopenicillanic acid (6-APA), which in turn is used to make amoxicillin and ampicillin. Penicillin V is a weak acid and it is extracted with n-butyl acetate at pH 2-3. In this pH range penicillin V is unstable and decomposes, therefore the aqueous medium in fermentation broth is cooled to $0^{o}C$ and extracted in centrifugal extractor to keep contact time as short as possible[12].

In the present work the fermentation broth was simulated by dissolving penicillin V sodium salt in distilled water. Liquid-liquid pertraction technique was conducted for the recovery of penicillin V in a batch pertraction laboratory unit. Methyl isobutyl ketone (MIBK), n-amyl acetate, and n-butyl acetate were proposed as membranes for penicillin V pertaction at $25^{o}C$. The effect of speed of agitation, time, and pH were studied.

2. Experimental Work

2.1. Material

Feed Phase (Donor Phase):

The feed phase was prepared by dissolving 1 g of penicillin V sodium salt in 1 L of distilled water, the pH of solution is adjusted by [4% H_2SO_4 (BDH)] and [5% Na_2CO_3 (BDH)][6].

Receiver Phase (Stripping Phase):

A sodium carbonate solution was used as a receiver phase.
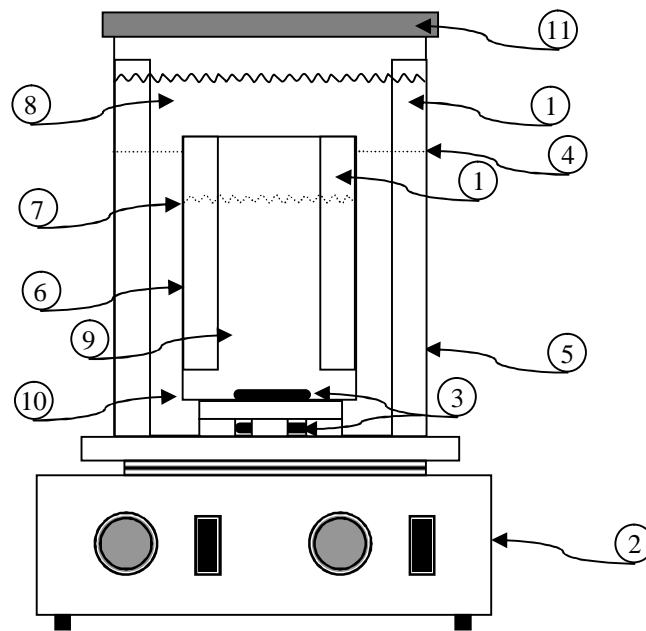
Membrane Phase:

In the present study, methyl isobutyl ketone (BDH), n-amyl acetate (BDH), and n-butyl acetate (BDH) were used as liquid membrane.

2.2. Pertraction Lab Unit

Pertraction experiments were carried out in 1 liter laboratory pertractor as shown in Fig. 1. The pertractor consists of two coaxial Pyrex beakers and baffles where placed in each beaker as shown in Fig. 1. The outer beaker is 1 liter and the inner is 250 ml. The two beakers were arranged as shown in Fig. 1 and placed on a magnetic stirrer with heater in order to control the temperature and the speed. The membrane, feed, and receiver phases were stirred by using two Teflon-coated magnetic bars.

2.3. Experimental Setup

500 ml of feed phase was placed in the annular space between the two beakers, and 200 ml of receiver phase was placed in the inner beaker. After that 300 ml of membrane phase was added to cover the other two phases as shown in Fig.1. The outer beaker was covered with a thin plastic layer to prevent evaporation of membrane phase. In the present study the effect of speed of agitation using the three proposed membranes was studied in the range of 300-500 rpm. The speed of agitation and temperature were adjusted and controlled by using hotplate and magnetic stirrer. The pertraction time was continuing up to 40 min and during this period of time samples were taken at a specified time interval from the feed and receiver phases for penicillin V analysis by HPLC. HPLC type Shimadzu model LC20AD was used in this analysis using column 100 RP-18 (5 μm). The penicillin V in the membrane organic phase was evaluated by material balance.

1	Baffles	7	Membrane-Receiver interface
2	Magnetic Stirrer	8	Membrane phase
3	Magnetic bars	9	Receiver phase
4	Membrane-Feed interface	10	Feed Phase
5	Feed-baker	11	Plastic cover
6	Receiver Baker		

Fig. 1.Schematic Diagram of Pertraction Laboratory Unit.

3. Results and Discussion

In the present work, the batch pertraction of penicillin V using the three proposed liquid membranes was studied, the agitation speed, and liquid membrane type was conducted in this work. The efficiency of penicillin V extracted, *E*, was calculated as follows:

$$E = \frac{C_r V_r}{C_{fo} V_f} \times 100\% \qquad \ldots(1)$$

Where C_r is the penicillin V concentration in the receiver phase, C_{fo} is the initial concentration in the feed phase, V_r is the volume of receiver phase, and V_f is the volume of feed phase.

3.1. Effect of pH

Figures 2 and 3 show the relationship between the penicillin transport from feed and to the receiver phases respectively with pH at different liquids membrane and at agitation speed of 400 rpm and time of extraction of 40 min. The range of pH for feed phase is taken between (4-6) and for receiver phase between (6-8) because the penicillin V is unstable and decomposes for pH < 4 and pH > 8[13]. From Figure 2, it can be seen that the extraction of penicillin V from feed is increasing with the decrease of pH value and also from Figure 3 the extraction of penicillin V by the receiver is increasing by increasing of pH value because the over all mass transfer coefficient increases when the difference in the pH value between two phases is high as possible[14]. In the Figure 2, it seems that the best value of pH for extraction of penicillin V from feed is 4 where about 98% of penicillin V is extracted by MIBK, while from Figure 3, the best value of pH for extraction of penicillin V by the receiver phase is 8 although the pH value of 7.5 has little effect on the extraction.
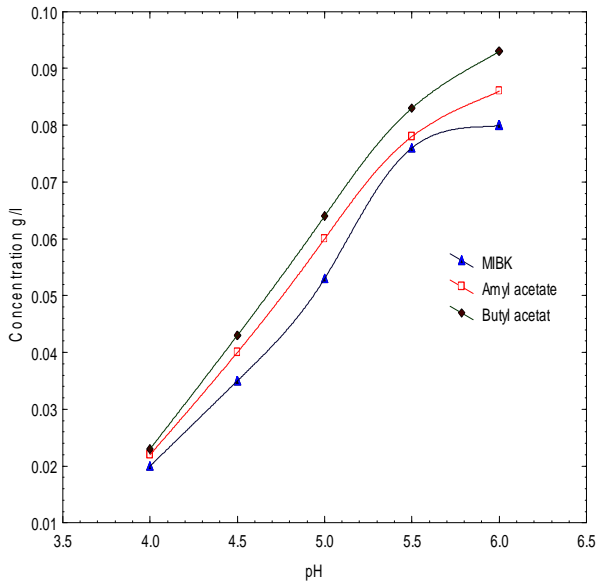
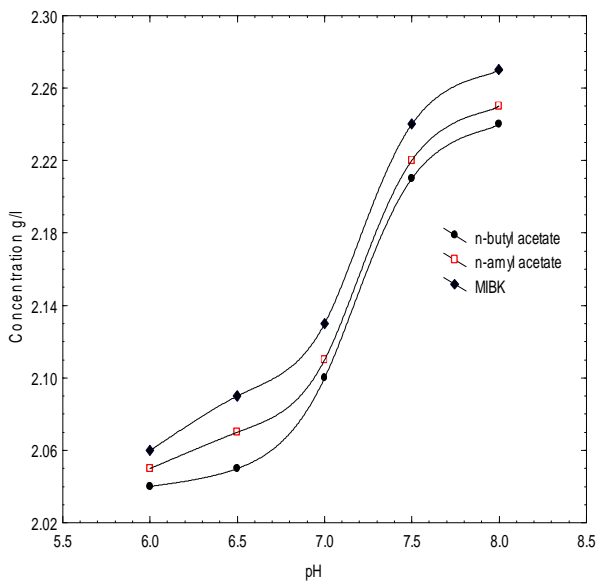**Fig. 2. pH Effect on Penicillin Extraction from Feed Phase after 40 min and Agitation Speed of 400 rpm.**

Fig. 3. pH Effect on Penicillin Extraction by Stripping Phase after 40 min and Agitation Speed of 400 rpm.

3.2. Effect of Membrane type

From figures 2 and 3, it can be seen that is a better solvent as a membrane and it can give better extraction efficiency methyl isobutyl ketone (MIBK) with respect to other solvents (n-amyl acetate and n-butyl acetate). The extraction efficiency of penicillin V is evaluated by using equation 1 for three types of membranes at

temperature of 25°C, rotation speed of 400 rpm and pH for feed 4 and for receiver phase 8 as shown in Table 1, where the difference in extraction efficiency for three types of membrane are very little; i.e., the effect of membrane type on extraction is little.

Table 1,
Extraction Efficiency, *E*, of Penicillin V for 3 Types of Membrane at 25°C, 400 rpm and pH of Feed 4 and of Receiver 8.

Membrane type	*E*
MIBK	90.8
n-amyl acetate	90
n-butyl acetate	89.6

Figure 4 shows the penicillin V content in the feed ($R_f = \dfrac{C_f}{C_{fo}}$), membrane, MIBK, ($R_m = \dfrac{C_m}{C_{fo}}$) and receiver phases ($R_r = \dfrac{C_r}{C_{fo}}$) during the extraction at temperature of 25°C, agitation speed of 400 rpm and pH of 4 for feed and 8 for receiver phases. It seems that about 80% of penicillin V is extracted during 15 min; i.e., the extraction process during this time is fast, while after 30 min the extraction is stable and there is no effect of time on extraction.
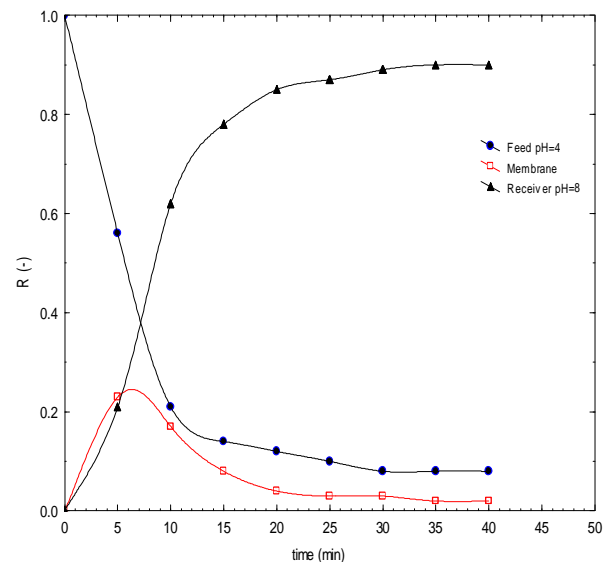

Fig. 4. Penicillin V Content in Feed, Membrane (MIBK), and Receiver Phases with Time at 25°C and 400 rpm .

3.2. Effect of Agitation Speed

Figure 5 shows the effect of speed of agitation on the extraction efficiency, *E*. In order to explore the effects of stirring rate, the extraction experiment were carried out at three different stirring rates, 300, 400, and 500 rpm. *E* value increases with increasing speed of agitation, which means that the extraction efficiency of penicillin V from feed phase to the receiver phase through liquid membrane improved with increasing the speed of agitation; this is because the higher stirring rate leads to much severer mixing between the aqueous solution and organic phase, which could accelerate the transport of penicillin V and enhance the mass transfer area between the aqueous solution and liquid membrane solution and reduce the mass transfer resistances of penicillin V from feed to liquid membrane in the extraction process, and from liquid membrane to the receiver phase in the stripping process. This variation in the efficiency indicates a diffusion control of the extraction process. According to previously published literature, although the mass transfer improved with higher speed of agitation, it was not applied because of increased risk of droplet formation which causes phase intermixing and deterioration of the process [10].
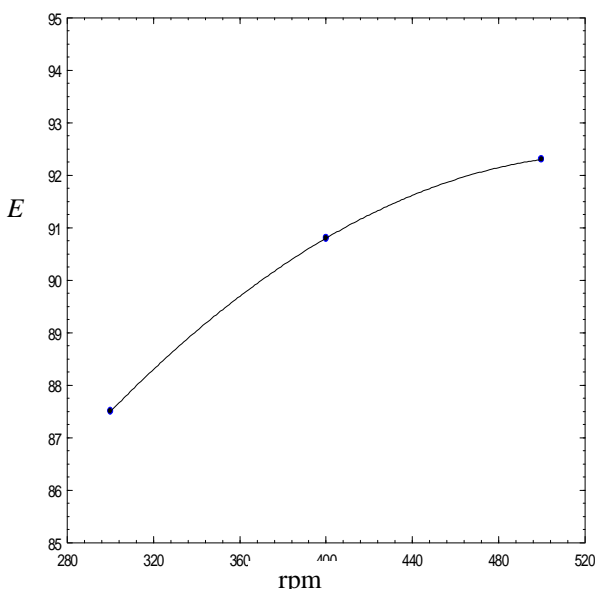

Fig. 5. Effect of Rotation Speed on the Extraction Efficiency Using MIBK as Membrane, at 25°C, and pH of 4 for Feed and 8 for Receiver Phases.

4. Conclusion

The liquid-liquid membrane extraction, pertraction, of biosynthetic products constitutes advantageous alternatives to conventional separation methods because it reduces the number of stages required for an efficient separation and, therefore, for the corresponding energy and material consumption. It can be concluded that the separation of Penicillin V from simulated broth could be enhanced by decreasing the pH value for feed up to 4 and increasing pH value up to 8 for receiver phase and increasing rotation speed up to 500 rpm. The type of solvent as a membrane has little effect on the extraction efficiency.

5. Reference

[1] James N. Parker, M.D. and Philip M. Parker, Penicillin, 2004, "A medical Dictionary, Bibliography", and Annotation Research Guide to internet References, copyright by Icon group international, Inc.

[2] Bradley D. Smith et al, 1998, "Facilitated of transport of carbohydrates, catecholamines, and amino acids though liquid and plasticized organic membranes", Journal of inclusion phenomena and molecular recognition in chemistry 32: 121-131.

[3] Mona M. Naima, Abir A. Monir, 2002, "Desalination using supported liquid membranes", Desalination 153, 361–369.

[4] Norman N. Li, Anthony G. Fane,W. S. Winston Ho, and T. Matsuura, 2008, "Advance membrane Technology and Application", John Wiley & Sons.

[5] Anil K. Pabby, Syed S. H. Rizvi, Ana Maria Sastre, 2009, "Handbook of membrane separation", Taylor & Francis Group.

[6] Cascavala D., Oniscua C., Cascavalb C., 2000, "Selective separation of penicillin V from phenoxyacetic acid using liquid membranes" , Biochemical Engineering Journal 5, 45-50.

[7] Zainuddin Abdul Manan, Mohamed Mahmoud Nasef, and Siti Hamidah Mohd, 2007, "Advances in separation process", First edition.

[8] Richard W. Baker, 2004, "Membrane Technology and applications", John Willy and Sons. 2nd Ed.

[9] Kamniski W., 2000, "Applicability of liquid membrane in the environmental protection",

Polish Journal of environmental studies Vol. 9, No. 1, 37-43.

[10] Boyadzhiev L., K. Dimitrov, D. Metcheva, 2006, "Integration of solvent extraction and liquid membrane separation: An efficient tool for recovery of bio-active substances from botantial", Elsevier 20 March.

[11] Nabil N. Ahmed Al-Hadithi, 2007, "Determination of drug and metabolites in the water by use of liquid membrane systems and HPLC-Method development and application" M.Sc. in Chemistry, Al-Anbar-Iraq.

[12] Elmar Heinzle, Arno P. Biwer, and Charles L. Coony, 2006, "Development of Sustainable Bioprocesses Modeling and Assessment", Copyright John Wiley & Sons Ltd.

[13] Benedict, RG., Schmidt, WH., Coghill, RD., Oleson, AP.(1945) "The stability of penicillin in aqueous solution", J. Bact. 49: 85-95.

[14] Kheirolomoon A., Sayfkordi A. A., Kazemi-Vaysari A., Ardjmand M., and Baradar-Khoshfetrat A. July 2001, "Mass transfer analysis of penicillin extraction", Scientia Iranica vol. 8, No. 3 PP 179-184.

استخلاص البنسلين V من ناتج التخمير المصطنع بأستخدام تقنية الغشاء السائل

خالد وليد حميد

قسم الهندسة الكيميائية الإحيائية/ كلية الهندسة الخوارزمي/ جامعة بغداد

البريد الالكتروني:Kwhameed74@yahoo.com

الخلاصة

تم استخدام تقنية الأستخلاص بطريقة الغشاء السائل لثلاث انواع من المذيبات العضوية (ايزوبيوتايل مثل كيتون، اسيتات البيوتايل الأعتيادي، اسيتات الأمايل الأعتيادي) والتي أستخدمت لغرض استخلاص البنسيلين V من ناتج التخمير المصطنع تحت ظروف تشغيل متباينة من اس هيدروجيني بمدى (٤-٦) للقيم و (٦-٨) للطور المستلم، زمن استخلاص بمدى (٠-٤٠ دقيقة)، وسرعة خلط بمدى (٣٠٠-٥٠٠ دورة/دقيقة) في منظومة مختبرية ذات النظام الدفعي. الظروف المثلى للأستخلاص كانت عند اس هيدروجيني ٤ للقيم و ٨ للطور المستلم، سرعة خلط ٥٠٠ دورة/دقيقة، زمن استخلاص ٤٠ دقيقة وللمذيب العضوي ايزوبيوتايل مثل كيتون، حيث اكثر من ٩٨% من البنسلين تم استخلاصه ضمن هذه الظروف.

دراسة تأثير نسبة طاقة وقود الديزل في وقود ثنائي على أداء محرك اشتعال بالانضغاط

معن جنان بشير

قسم هندسة المكائن والمعدات/ الجامعة التكنولوجية

الخلاصة

يهدف البحث لدراسة تأثير نسبة وقود الديزل المحقون في محرك اشتعال بالانضغاط، أحادى الاسطوانة يعمل بوقود ثنائي على أداء ذلك المحرك، وذلك بإضافة الغاز النفطي المسال إلى وقود الديزل بنسب حجمية مختلفة.

تزداد الكفاءة الحرارية المكبحية بزيادة نسبة وقود الديزل عند الأحمال المنخفضة، وتقل بزيادة الحمل، وللحصول على تشغيل مستقر لمحرك يعمل بوقود ثنائي يجب الحفاظ على كمية مناسبة من وقود الديزل، إذ عند العمل بأقل منها يعمل المحرك بتشغيل غير نظامي ويحصل إخفاق بالاشتغال.

يكون الاستهلاك النوعي للوقود لمحركات ثنائية الوقود أكبر من قيمتها عند العمل بوقود ديزل فقط عند أحمال جزئية، أما عند حمل قريب من (٨٠-١٠٠ %) من الحمل الكلي ، فان الاستهلاك النوعي للوقود في محرك ثنائي يقترب من قيمته عند العمل بوقود ديزل فقط.

الكلمات المفتاحية: وقود ثنائي، غاز نفطي مسال، محرك اشتعال بالأنضغاط، نسبة مكافئة، قدرة مكبحية، استهلاك نوعي مكبحي، كفاءة حجمية، كفاءة حرارية مكبحية.

١. المقدمة

تعرف محركات الوقود الثنائي بأنها المحركات التي يمكن أن تعمل على نوعين مختلفين من الوقود، أحدهما الوقود الغازي والآخر وقود سائل، أو بأي من الوقودين بصورة منفصلة.

وهناك عدة عوامل ساهمت في استخدام هذا النوع من المحركات [1,2,3] وهي:

١. توفر الوقود الغازي بأسعار ارخص من الوقود السائل، بالمقارنة مع القيمة الحرارية الناتجة من كليهما.

٢. قرب نضوب الوقود السائل التقليدي في المستقبل القريب.

٣. قلة التلوث الحاصل للبيئة نتيجة نظافة الاحتراق الناتج من محركات الوقود الغازي مقارنة مع المحركات التي تستخدم الوقود السائل.

٤. طول العمر التشغيلي للمحرك نتيجة قلة تخفيف سائل التزييت، وقلة التآكل الحاصل بين الأسطح المتماسة للمحرك.

٥. سهولة نقل الغاز المسال بصورة اقتصادية بسبب التطورات الكبيرة الحاصلة في بناء الخزانات.

٦. بساطة المعدات اللازمة لتحويل محرك اشتعال بالانضغاط أو بالشرارة إلى محرك يعمل بوقود ثنائي، وامكانية تغيير عمل المحرك من نوع إلى آخر بصورة تلقائية في الظروف الاضطرارية.

ويمكن العمل بأنواع عديدة من الوقود الغازي في محركات الوقود الثنائي، ومن الغازات المستخدمة الغاز الطبيعي، الغاز النفطي المسال، الهيدروجين وغاز الفضلات [4,5].

ولكن للوقود الغازي مساوئ تحد من استخدامه وتتطلب دراسات أكبر للتقليل من اثرها، فالوقود الغازي يحتاج الى نسب انضغاط عالية لانجاز عملية الاحتراق بصورة كفوءة، وذلك

لارتفاع درجة حرارة اتقاده الذاتي، ونسبة الانضغاط العالية هذة غير متوفرة في محركات الاشتعال بالشرارة [11].

كما لأن فترة تأخر الأشعال للوقود الغازي أطول مقارنة بالديزل بسبب رقمه السيتاني الأقل، كما أن الكفاءة الحجمية لحالة وقود غازي أقل مقارنة بوقود ديزل . ويجب أن لا تقل القيمة الحرارية للوقود الغازي المستخدم في محرك وقود ثنائي عن ٢٤٣٠ كيلوجول للمتر المكعب [1] . وتؤثر عوامل عديدة في طبيعة الاحتراق لمحركات الوقود الثنائي، منها:

● كمية وقود الديزل: يستخدم وقود الديزل ليساعد في بدء الاشتعال، ويحقن عادة قبل النقطة الميتة العليا بعدة درجات قبل انتهاء شوط الانضغاط، فإذا كانت كمية الوقود المضخة كبيرة فان كمية الحرارة المتحررة والمنتقلة إلى الخليط ستكون كبيرة أيضا، وينتج عن ذلك حصول احتراق سريع يصاحبه ارتفاع حاد بالضغط الأقصى للأسطوانة، مما يجعل المحرك في ظروف قريبة من ظروف حالة الطرق [2]، أما إذا كانت كمية وقود الديزل قليلة فسوف تنخفض القدرة الخارجة من المحرك نتيجة عدم اشتعال الخليط بصورة تامة، وخروج كمية من الوقود غير المحترق مع الغاز العادم [6,7].

لقد أكدت اغلب الدراسات أن افضل قدرة يمكن الحصول عليها من محرك وقود ثنائي عندما تكون نسبة وقود الديزل بحدود ٧ الى١٥ بالمائة من الطاقة الحرارية الكلية الداخلة إلى المحرك عند حمل كلي [11].

● تأثير توقيت الحقن [1,2]: يسبب التوقيت المبكر للحقن زيادة فترة تأخير الاشتعال، مسببا ارتفاع قيمة الضغط الأقصى، مما يزيد احتمال حصول حالة الطرق، أما التوقيت المتأخر للحقن فيقلل فترة تأخير الاشتعال، مما يؤدي إلى حصول الاحتراق بعد النقطة الميتة العليا بدرجات عديدة، مما يقلل من

الضغط الأقصى للأسطوانة، وبالتالي انخفاض القدرة الخارجة من المحرك.

- تأثير العدد السيتاني[3,8]: يسبب انخفاض العدد السيتاني عن قيمته الطبيعية ضعف في أداء عمل المحرك الوقود الثنائي، وان كان تأثير العدد السيتاني قليلا في طبيعة ونوعية الاحتراق لمحركات الوقود الثنائي بالمقارنة مع العدد الأوكتاني للوقود الغازي.

- تأثير درجة حرارة الخليط الداخل إلى المحرك[1,3]: تسبب زيادة درجة حرارة الخليط الداخل للاسطوانة عند الأحمال العالية انخفاض القدرة الخارجة من المحرك، وزيادتها عند الأحمال المنخفضة تستوجب العمل بالجانب الضعيف (Ø<1)، إن انخفاض درجة حرارة الخليط عند الأحمال الجزئية للمحرك العامل بخليط غني (Ø>1) يؤدي إلى تحسين الكفاءة الحرارية ولكن يؤثر على مقدار الأستهلاك النوعي للوقود، بينما تنخفض الكفاءة في حالة خليط ضعيف لعدم حصول الاحتراق التام، وخروج كمية من الوقود مع غاز العادم.

- تأثير نوع الوقود الغازي المستخدم[1,9]: يعتمد تأثير نوع الوقود الغازي المستخدم في محركات وقود ثنائي بشكل أساسي على حدود اشتعاله ومقاومته للطرق، وتختلف هاتان الخاصيتان باختلاف مكونات الغاز.

تعطي كل أنواع الوقود الغازي قدرة عالية عند العمل في الجانب الغني (Ø>1) من الخليط، اكثر من عملها في الجانب الضعيف (Ø>1)، وأغلبها لها مقاومة عالية للطرق، وتعتمد النسبة المكافئة الداخلة إلى محرك الوقود الثنائي بدرجة رئيسية على كمية وقود الديزل اللازمة لإشعال الخليط في غرفة الاحتراق، لذا يمكن الحصول على قدرة عالية من المحرك عند العمل بخليط ضعيف، لأنه يمتاز بفترة تأخير طويلة نسبيا، وبمعدل احتراق بطيء، يؤدي إلى اقتراب موضع الضغط الأقصى للأسطوانة من النقطة الميته العليا، مما يزيد من كفاءة الاحتراق، أما العمل بالجانب الغني من الخليط، فسوف يحدث احتراق سريع ومفاجئ، يصاحبه ارتفاع حاد في ضغط الاسطوانة الأقصى مسببا حالة الطرق[10].

تهدف الدراسة لتوضيح تأثير نسب طاقة وقود الديزل الداخلة الى المحرك مقارنة بالطاقة الكلية على أداء محرك أحادي الأسطوانة يعمل بالانضغاط.

2. الأجهزة المستخدمة

1- تمت التجارب باستخدام محرك أحتراق داخلي يعمل بالانضغاط أحادي الاسطوانة رباعي الأشواط ذو نسب انضغاط متغيرة، نوع (Prodit, GR0306/000/037A, Italy) ويوضح جدول رقم 1 مواصفات المحرك المستخدم في العمل.

2- يقاس الهواء المجهز الى المحرك بواسطة مقياس فوهة، ويتكون نظام تجهيز الهواء من: انبوب سحب الهواء، غرفة تخميد، ومحول القدرة للضغط التفاضلي.

3- يستخدم الديناموميتر الهيدروليكي لقياس عزم المحرك الخارج.

4- تقاس درجة حرارة الغاز العادم باستخدام مزدوجات حرارية نوع K (Ni-Cr)/(Ni-AL) مثبتة عند بداية أنبوب العادم.

5- نظام تجهيز المحرك بالغاز النفطي المسال:
تتكون المنظومة المستخدمة في البحث لتجهيز المحرك بالغاز النفطي المسال من الأجزاء التالية : خزان الوقود، مرشح الوقود، صمام كهرومغناطيسي، مبخر الغاز النفطي المسال، مقياس تدفق الوقود الغازي مقياس فوهة مصمم حسب المواصفات البريطانية، ونسبة المساحة له (m=0.05353)، صندوق التخميد، مغذي الغاز ومانعة اللهب. وقد تم استخدام الغاز النفطي المسال المنتج من شركة غاز التاجي– العراق، والمكون من: 1% إيثان، 48.18 % بروبان، 18.17 % أيزوبيوتان، 32.65% ن. بيوتان.

6- نظام تجهيز المحرك بوقود الديزل: تتكون المنظومة المستخدمة في البحث من خزان وقود ديزل، مقياس حجم الوقود، مرشح الوقود والصمام. وقد استخدم في هذا البحث وقود ديزل منتج من مصفى الدورة-بغداد- العراق، وبرقم سيتاني 47.8 .

يبين الشكل 1 مخطط للجهاز المستخدم في التجارب مع كامل ملحقاته.
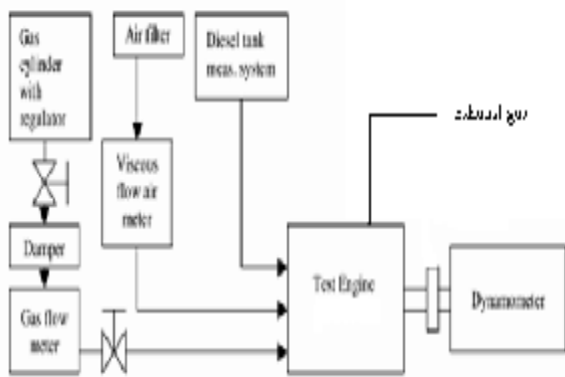
شكل ـ1ـ مخطط للأجهزة المستخدمة في التجارب.

استخدمت المعادلات التالية لحساب متغيرات المحرك المهمـة وكما يلي:

1. القدرة المكبحية

$$bp = W_b \times N / 348.067$$

حيث: W_b- الحمل المسلط بالنيوتن.
N - سرعة المحرك دورة/ ثانية.

2. النسبة المكافئة

$$Ø = (A/F)_{stoichiometric} / (A/F)_{actual}$$

3. الاستهلاك النوعي المكبحي للوقود

$$bsfc = m_f^\circ \times 3600 / bp$$

حيث: m_f^o – معدل استهلاك الوقود (الغاز النفطي المسـال + الديزل).

4. الكفاءة الحجمية

$$\eta_{vol} = (m_a)_{act} / (m_a)_{theo.} \times 100$$

حيث: $(m_a)_{act.}$ - كتلة الهواء المتدفقة داخل المحرك عمليا.
$(m_a)_{Theo.}$ - كتلة الهواء المتدفقة داخل المحرك نظريا.

عموما بارتفاع الاستهلاك النوعي للوقود عند الأحمال المنخفضة، نتيجة لانخفاض النسبة المكافئة وعدم احتراق وقود الديزل بصورة تامة.

عند الأحمال المتوسطة (315-521 kpa) فأن أعلى استهلاك نوعي للوقود يحدث أيضا عند اقل نسبة لوقود الديزل، ويستمر بالانخفاض مع ارتفاع هذة النسبة إلى أن يصل إلى اقل قيمة له عند عمل المحرك فقط بوقود الديزل، وذلك لأن زيادة الحمل وانخفاض تركيز الوقود الغازي في الخليط يؤدي إلى زيادة كمية الهواء الداخل للمحرك وتحسن الكفاءة الحجمية للمحرك، ومن ثم زيادة كفاءة الاحتراق.

أما عند الأحمال العالية (652 kpa)، فأن اقل استهلاك نوعي للوقود يحدث عند اقل نسبة لوقود الديزل، بسبب زيادة حرارة غرفة الأحتراق وانخفاض كمية الوقود غير المحترق، ويكون أعلى قيمه للأستهلاك النوعي المكبحي للوقود عند عمل المحرك بوقود الديزل بمفرده، وذلك لعدم توفر فترة زمنية كافية لحرق الوقود بصورة تامة، مما يؤدي إلى خروج كمية منه مع الغاز العادم، الأمر الذي يؤدي إلى زيادة الاستهلاك النوعي للوقود.

يوضح الشكل 3 العلاقة بين الكفاءة الحرارية المكبحية ومعدل طاقة الديزل الداخلة للمحرك لأحمال محددة، إذ تبدأ كل المنحنيات من نقطة حصول إخفاق الاشتعال نتيجة لعدم توفر وقود الديزل بكميات كافية لحصول عملية الاحتراق بصورة مستقرة.

يؤدي عمل المحرك بأحمال جزئية مع تقليل نسبة وقود الديزل وثبوت الحمل إلى انخفاض الكفاءة الحرارية المكبحية للمحرك، ويبرز التأثير اكثر وضوحا عند الأحمال المنخفضة، إذ أن زيادة نسبة وقود الديزل من 15.7 إلى 100% ومن 11.1 إلى 100% لأحمال (3.08 و 5.33) بار، تؤدي إلى زيادة الكفاءة بنسبة 17 و 10 % على التوالي.
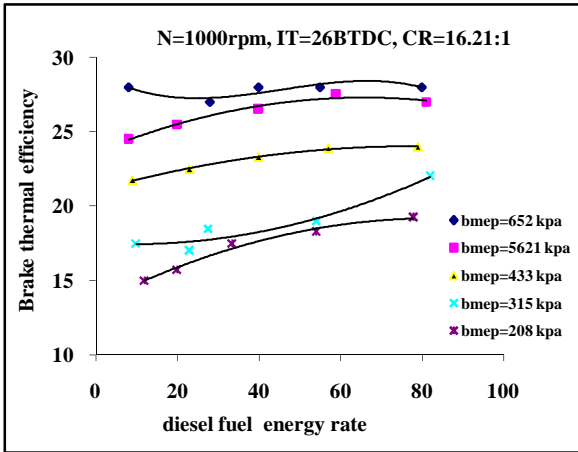
شكل-3- العلاقة بين الكفاءة الحرارية المكبحية ونسبة الطاقة الحرارية لوقود الديزل إلى الطاقة الكلية الداخلة إلى المحرك.

أما عند عمل المحرك بحمل قريب من الحمل لأقصى بحدود 7.52 بار، فقد لوحظ تساوي قيم الكفاءة الحرارية لمحرك وقود ثنائي لحالة العمل بوقود ديزل فقط، وذلك لان محرك ثنائي الوقود يمكن أن يحرق كمية اكبر من الوقود الغازي الذي يملأ غرفة الاحتراق، نتيجة لتكوين العديد من جبهات اللهب المنتشرة داخل غرفة الاحتراق والحصول على احتراق بصورة كفوءة، وبالتالي زيادة القدرة الناتجة من المحرك، أما عندما يكون الوقود سائلا فان قطرات الديزل لا يمكن أن تشغل حيز غرفة الاحتراق بأكمله،

٥. نسبة الطاقة الحرارية لوقود الديزل الى الطاقة الكلية لخليط الوقود الداخل للمحرك:

$$diesel\ fuel\ energy\ ratio$$
$$= \frac{m_{diesel}^{°} \times LHV_{diesel}}{m_{diesel}^{°} \times LHV_{diesel} + m_{LPG}^{°} \times LHV_{LPG}}$$

خطوات إجراء التجارب :

تمت التجارب بعد تشغيل المحرك لفترة من الزمن ووصوله لحالة الاستقرار ووصول درجة حرارة زيت المحرك لدرجة 60° مئوية ± 5°، ودرجة حرارة ماء التبريد لدرجة 70° ± 5 مئوية، بعد ذلك تم تغيير العوامل المذكورة وكما يلي:

١. نوع الوقود من وقود ديزل نقي (اعتبرت الحالة الأساسية باستخدام الديزل بمفرده لأغراض المقارنة)، الى وقود ثنائي مكون من ديزل وغاز نفطي مسال.

٢. تغيير حمل المحرك من بلا حمل ولغاية الحمل الكلي.

٣. تغييرتوقيت حقن وقود الديزل من 20 ولغاية 45 ° قبل النقطة الميته العليا وبخطوات كل منها عبارة عن 5°.

3. المناقشة

يوضح شكل 2 العلاقة بين الاستهلاك النوعي المكبحي للوقود ونسبة الطاقة الحرارية لوقود الديزل إلى الطاقة الكلية الداخلة للمحرك عند عمل المحرك بأحمال محددة.

يحدث اكبر استهلاك نوعي للوقود للأحمال المنخفضة 208) (kpa عند اقل نسبة لوقود ديزل، نتيجة ضعف قوة الخليط وانخفاض كفاءة الاحتراق، ومع ارتفاع نسبة وقود الديزل يبدأ الاستهلاك النوعي للوقود بالانخفاض، لأن زيادة كمية وقود الديزل تؤدي إلى ارتفاع الطاقة الحرارية المنتقلة منها إلى الوقود الغازي، وبالتالي انخفاض كمية الوقود غير المحترق الذي يخرج مع الغاز العادم.
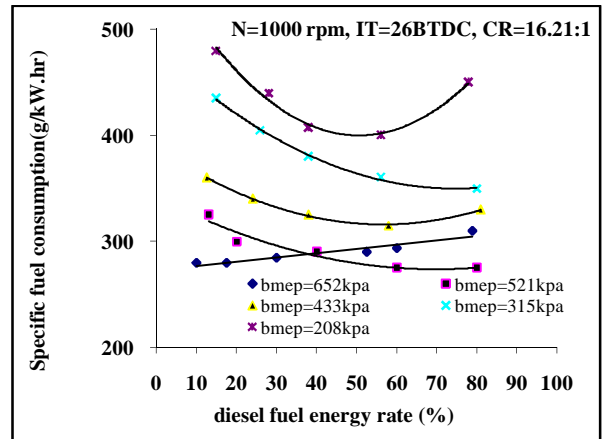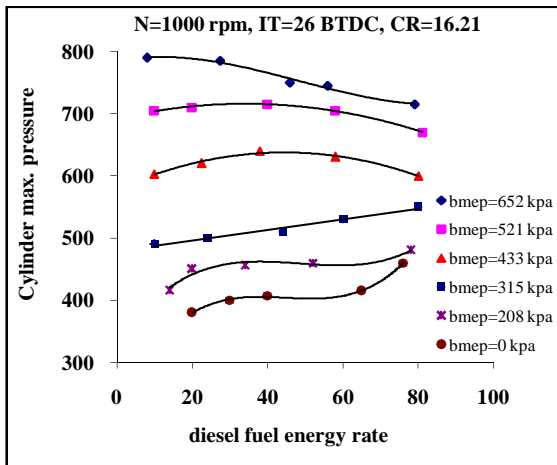

شكل-2- العلاقة بين الاستهلاك النوعي للوقود ونسبة الطاقة الحرارية لوقود الديزل إلى الطاقة الكلية الداخلة للمحرك عند عمل المحرك بأحمال متغيرة.

ويعود الاستهلاك النوعي للوقود للازدياد مرة أخرى عند عمل المحرك فقط بوقود الديزل، وذلك لأن محركات الديزل تمتاز

وينتج عن ذلك خروج كمية من الوقود غير المحترق مع الغاز العادم.

نلاحظ من المنحنيات أن زيادة الحمل تؤدي إلى زيادة الكفاءة الحرارية المكبحية لنفس الكتلة، وذلك لان زيادة الحمل تؤدي إلى تحسين كفاءة الاحتراق.

شكل-٤- العلاقة بين الكفاءة الحرارية المكبحية ومتوسط الضغط الفعال عند عمل المحرك بوقود ديزل فقط، وبأقل نسبة من الطاقة الحرارية لوقود ديزل إلى الطاقة الكلية الداخلة للمحرك.

يوضـح شـكل ٤ العلاقـة بـين الكفـاءة الحراريـة المكبحيـة ومتوسـط الضـغط الفعـال عنـد عمـل المحـرك بوقـود ديـزل (١٠٠%)، وبأقل نسـبة مـن الطاقـة الحراريـة لوقـود ديـزل إلـى الطاقة الكلية الداخلة للمحرك.

تتـراوح اقل نسـبة مـن وقـود الـديزل اللازمـة لعمـل المحـرك ثنـائي الوقـود بصـورة مسـتقرة وبثبـوت كـل مـن السـرعة وتوقيت الحقـن ونسـبة الانضـغاط ولأحمـال مختلفـة بحـدود مـن ١٨.٢ إلـى ١٩.٣% مـن الطاقـة الحراريـة الداخلـة إلـى المحـرك. أمـا عنـد الأحمـال القصـوى والقريبـة منهـا فيلتقي المنحنيان عند نقطة معينة، ممـا يعنـي أن أضـافة كميـات أكبـر مـن وقـود الديزل غير مبررة ولا تسـبب زيـادة تذكر فـي قيم الكفاءة الحرارية المكبحية للمحرك، كمـا يبين الشكل.

شكل ـ٥ـالعلاقة بين الطاقة الحرارية التي يستهلكها المحرك ونسبة الطاقة الحرارية لوقود الديزل إلى الطاقة الكلية.

أما عند عمل المحرك بدون حمل، كما يوضح شكل ٥، والذي يبين العلاقة بين الطاقة الحرارية التي يستهلكها المحرك ونسبة الطاقة الحرارية لوقود الديزل إلى الطاقة الكلية، فان انخفاض كمية الوقود غير المحترق وارتفاع الطاقة الحرارية التي يستهلكها المحرك تسبب زيادة كفاءة الاحتراق في النسب العالية لوقود الديزل. أما انخفاض نسبة وقود الديزل فتؤدي إلى عدم احتراق الوقود بصورة تامة، مما يستدعي زيادة كمية الوقود التي يحتاجها المحرك للحفاظ على السرعة المطلوبة.

يبين شكل ٦، العلاقة بين قيم الضغط المسجلة لنسب مختلفـة مـن الطاقـة الحراريـة لوقـود الـديزل إلـى الطاقـة الكليـة الداخلـة للمحرك، ويلاحظ انخفاض القيمة القصوى للضغط عند الأحمـال الجزئية في حالة عمل المحرك بنسب منخفضة من وقود الديزل، إن قيمة الضغط الأقصى للأسطوانة منخفضة، وتزداد مـع زيـادة نسبة الوقود الديزل إلى أن تصل إلى أعلى قيمة لها.

وعند الأحمال المتوسطة فأن انخفاض كمية الوقود الغازي في الخليط تسبب زيادة كمية الهواء الداخل للأسطوانة، وأن ارتفاع نسبة وقود الديزل تؤدي إلى زيادة كمية الحرارة المتحررة منه والمنتقلة إلى الوقود الغازي مما يزيد من كفاءة الاحتراق.

أمـا عنـد حمـل قريـب مـن الحمـل الأقصـى فأن أعلى قيمة للضغط داخل الاسطوانة تحدث عند عمل المحرك بأقل نسبة من وقـود الديزل، وتبدأ القيمة بالانخفاض التدريجي مـع زيـادة نسـبة وقـود الديزل، نتيجـة نقصـان فتـرة تـأخير الاشتعـال، وعـدم تـوفر فتـرة زمنيـة كافيـة لتحضـير أكبـر كميـة مـن الوقـود الجـاهز للاشتعـال، وان طبيعـة الخلـط فـي النسـب العاليـة للوقـود الغـازي فـي محـرك وقـود ثنائي عند الأحمـال العاليـة افضـل بكثيـر مـن طبيعـة الخلـط فـي محـرك يعمـل بالـديزل فقـط، ممـا يـؤدي إلـى تقـدم وانتشـار اللهـب، وحصـول الاحتراق بصـورة سـريعة وكفـوءة، إذا انخفضـت القيمة القصوى للضغط عند عمل المحرك فقط بوقود الديزل.
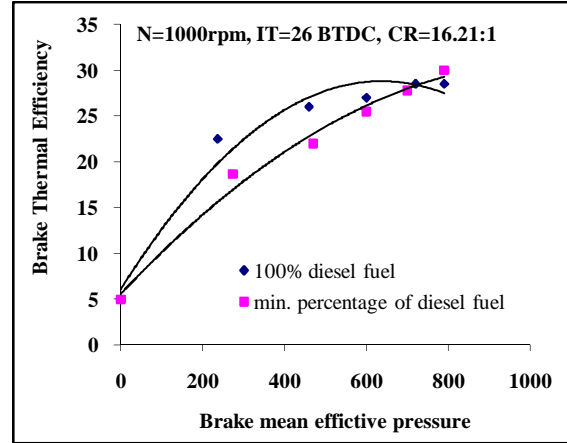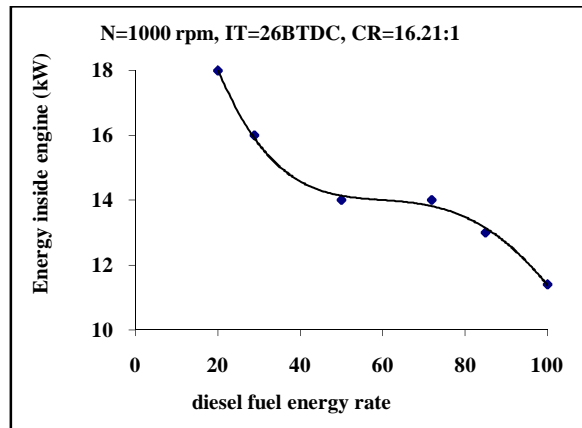

شكل ـ٦ـ قيم الضغط المسجلة لمجموعة التجارب لنسب مختلفة من الطاقة الحرارية لوقود الديزل إلى الطاقة الكلية الداخلة للمحرك.

إن فتـرة تـأخير الاشتعـال المقاسـة بدلالة درجات عمود المرفق من منحنى الضغط مع درجات عمود المرفق، تمثل الفتـرة المحصـورة من بداية حقن الوقود إلى الدرجة التي ينفصل فيها منحنى الضغط عند حصول الاحتراق عن منحنى الضغط للهواء في حالة تدوير المحرك بثبوت السرعة.

يوضح شكل ٧، العلاقة بين الدرجة التي يتم بها بدء الاشتعال بثبوت توقيت الحقن عند ٢٦ درجة قبل النقطة الميتة العليا، لنسب

مختلفة من الطاقة الحرارية لوقود الديزل إلى الطاقة الكلية الداخلة للمحرك وبأحمال مختلفة. إذ لوحظ زيادة فترة التأخير عند النسب العالية للوقود الغازي، ولا تلبث أن تنخفض مع نقصان هذة النسبة، وذلك لان زيادة نسبة الوقود الغازي في الخليط تؤدي إلى انخفاض كمية الهواء الداخل للمحرك نتيجة الحجم الذي يشغله بدلا من الهواء، كما تسبب زيادة طول فترة التأخير الكيميائية للخليط نتيجة عدم توفر الأكسجين بكميات كبيرة.

للخليط، وبما أن زيادة الحمل تسبب زيادة درجة حرارة مكونات الاسطوانة، لذا تقل هذة الفترة.

4. الاستنتاجات

1. تؤدي زيادة نسبة وقود الديزل في الأحمال المنخفضة إلى انخفاض الاستهلاك النوعي للوقود، إلى أن تصل اقل قيمة له عند نسب بحدود 40 لغاية 60% من وقود الديزل، بعد ذلك يعود للارتفاع مرة أخرى.

2. يحصل أعلى استهلاك نوعي للوقود في الأحمال المتوسطة عند اقل نسبة من وقود الديزل. وعند حمل قريب من الحمل الكلي يحدث اقل استهلاك نوعي للوقود عند اقل نسبة من وقود الديزل.

3. تسبب زيادة نسبة وقود الديزل في الأحمال المنخفضة إلى ارتفاع الكفاءة الحرارية المكبية تدريجيا، وبصورة أوضح مما هو عليه الحال عند عمل المحرك بأحمال متوسطة. إن الكفاءة الحرارية المكبية لمحرك وقود ثنائي في الأحمال العالية اكبر من قيمها عند العمل بالأحمال الجزئية.

4. عند عمل المحرك بحمل قريب من الحمل الكلي فأن الكفاءة الحرارية المكبية للمحرك الثنائي تكون مساوية تقريبا لقيمتها عند العمل بوقود ديزل فقط.

5. إن أعلى قيمة للضغط الأقصى للأسطوانة في الأحمال المنخفضة يحدث عند عمل المحرك بوقود ديزل فقط، فيما تكون أعلى قيمة له عند عمل المحرك بأحمال متوسطة عند نسب محصورة بين 40 الى 60% من وقود الديزل، أما عند حمل قريب من الحمل الكلي فان أعلى قيمة للضغط الأقصى داخل الاسطوانة يحدث عند اقل نسبة وقود ديزل.

شكل-7-العلاقة بين تأخر الأشعال ونسب الطاقة الحرارية لوقود الديزل إلى الطاقة الكلية الداخلة للمحرك لأحمال مختلفة.

تتأثر فترة تأخير الاشتعال بالضغط ودرجة حرارة الخليط أثناء شوط الانضغاط، إذ تقل هذة الفترة بزيادة درجة الحرارة والضغط

جدول 1،
مواصفات المحرك المستخدم في البحث.

Technical characteristics	
- Manufacture	PRODIT s.a.s.
-Cycle	OTTO or DIESEL, four strokes
-Number of cylinder	1 vertical
-Diameter	90 mm
-Stroke	85 mm
-Swept volume	541 cm^3
-Compression ratio	4÷17.5
-Max. power	4 kWat 2800 rpm
-Max torque	28Nm at 1600rpm
-water cooled	
-No load speed rang	500÷3600 rpm (Otto cycle)
-Load speed range	1200÷3600 rpm (Otto cycle)
-Intake start	54° before T.D.C.
-Intake end	22° after T.D.C.
-Exhaust start	22° before T.D.C.
-Exhaust end	54° after T.D.C.
-Fixed spark advance	10° (spark ignition)

Ambassador car engine, IE(I) Journal-MC, vol. 84, 2003.

[6] Mockus, S., Sapragonas, J., Stonys, A., Pukalskas, S., Analysis of exhaust gas composition of internal combustion engines using LPG, Journal of environmental engineering and landscape management, vol. 15, N0. 1, 2006

[7] Song, S and Hill, P.G., Duel fueling of a pre-chamber diesel engine with natural gas, SAE paper No.991115, 1999.

[8] Benea B C and Soica A O, Researches regarding using LPG on diesel engine, Fascicle of Management and Technological Engineering, vol. VI (XVI), 2007.

[9] Karim G A, An Examination of some measures for improving the performance of gas fuelled diesel engine at light load. SAE Transactions, 912366, 1991.

[10] Qi D H, Bian Y ZH, Ma ZH Y, Zhang CH H and Liu SH Q, Combustion and exhaust emission characteristics of a compression ignition engine using liquefied petroleum gas-Diesel blended fuel. Energy Conversion and Management, vol. 48, No.2, pp: 500 -509, 2007.

[11] Sethi V P and Salariya K S, Exhaust Analysis and Performance of a Single Cylinder Diesel Engine Run on Dual Fuels, IE (I) Journal.MC vol. 85, April, 2004.

قائمة الرموز المستخدمة

بعد النقطة الميتة العليا	ATDC
قبل النقطة الميتة العليا	BTDC
درجات من عمود المرفق	ᵒCA
نسبة الأنضغاط	CR
نسبة الوقود الى الهواء	FAR
توقيت الحقن الأمثل	OIT
متوسط الضغط المكبحي الفعال	bmep
القدرة المكبحية	bp
أستهلاك الوقود النوعي المكبحي	Bsfc

٦. المصادر

[1] Salariya, K S, Sethi, V, Exhaust analysis and performance of a single cylinder diesel engine run on dual fuels, IE (I) Journal, vol.85, 2004.

[2] Karim, G.A. and Klat, S.R. and Moore, N.P.W., Knock in dual fuel engine, Proc. Inst. of Mech. Eng., vol. 181, Pt.1, 1996.

[3] Karim, G.A., A review of combustion processes in the duel fuel engines, the gas-diesel engine, Prog. Energy Combustion Sci. J., vol. 1, 1989.

[4] Annand, W.J.D., Heat transfer in the cylinder s of reciprocating internal combustion engine, Ph.D. thesis, University of Manchester, England, 1992.

[5] Yamin, A. A., Servastava, R. M., Performance compression of LPG and gasoline as fuels of

Study of Effect of Diesel Fuel Energy Rate in Duel Fuel on Performance of Compression Ignition Engine

Maan Janan Basheer

Department of Machines and Equipment Engineering /University of Technology

Abstract

The aim of this work is to study the effect of diesel fuel percentage on the combustion processes in compression ignition engine using dual – fuel (diesel and LPG).

The brake thermal efficiency increased with the increase of diesel fuel rate at low loads, and decreased when load increased. To get sufficient operation in engine fueled with dual fuel, it required sufficient flow rate of diesel fuel, if the engine fueled with insufficient diesel fuel erratic operation with miss fire cycles presented.

Dual-fuel operation at part load showed higher specific fuel consumption than straight diesl operation. At full loads, brake specific fuel consumption of duel fuel engine approaches that for diesel fuel values.